A metal hydride air-conditioning system for fuel cell vehicles

A thesis accepted by the Faculty of Energy-, Process- and Bio-Engineering of the University of Stuttgart to fulfil the requirements for the degree of Doctor of Engineering Sciences (Dr.-Ing.)

by

Christoph Weckerle

born in Geislingen (Steige)

Main referee:	Prof. Dr. André Thess
Co referee:	Prof. Dr. Thomas Klassen
Date of oral exam:	15.07.2020

Institute for Building Energetics, Thermotechnology and Energy Storage
of the University of Stuttgart

2020

Eigenständigkeitserklärung

Hiermit versichere ich, dass ich die vorgelegte Dissertation selbständig und nur mit den angegebenen Hilfsmitteln verfasst habe. Alle Passagen, die ich wörtlich oder sinngemäß aus der Literatur oder anderen Quellen, wie z. B. Internetseiten übernommen habe, habe ich als Zitat mit der Angabe der Quelle kenntlich gemacht.

Zusammenfassung

Hochdrucktanks sind die etablierte Speichertechnologie für Wasserstoff in mobilen Systemen. Jedoch werden für die Kompression auf 700 bar etwa 15 % des unteren Heizwertes von Wasserstoff benötigt. Eine „offene“ Klimaanlage auf Basis von Metallhydriden (MH) stellt einen vielsprechenden Ansatz dar, um diese bisher ungenutzte und im Fahrzeug vorhandene potentielle Energie des komprimierten Wasserstoffs als Antriebsenergie zu verwenden. In der vorliegenden Dissertation wird ein solches System erstmalig systematisch untersucht und demonstriert, inwieweit diese Energie in nutzbare Kälte gewandelt werden kann.

Dafür wird ein Versuchsaufbau realisiert, der aus zwei neuartigen Plattenreaktoren besteht, die mit einer Polymerelektrolytmembran-Brennstoffzelle (BSZ) gekoppelt sind. Die Reaktoren mit optimierter Wärmeübertragungscharakteristik und einem mittleren Wärmetransportweg von 0,44 mm im MH-Bett sind mit ca. 1,5 kg Hydralloy® C2 ($Ti_{0.98}Zr_{0.02}Mn_{1.46}V_{0.41}Cr_{0.05}Fe_{0.08}$) befüllt, das im Temperaturbereich von 0 bis 50 °C thermodynamisch charakterisiert wird.

Der Funktionsnachweis bei einer elektrischen Leistung von 5 kW zeigt, dass die BSZ-Funktionalität durch die alternierenden Reaktoren mit einer Halbzyklusdauer von 145 s nicht beeinträchtigt wird. Wasserstoff wird bei 35 bar absorbiert und ein kontinuierlicher Massenstrom bei einem BSZ-Gegendruck von 4,1 bar zur Verfügung gestellt. Unter Referenzbedingungen mit einer Umgebungstemperatur von 30 °C und einer Kältetemperatur von 20 °C, können etwa 45 % der bisher ungenutzten potentiellen Energie des Wasserstoffs bei 700 bar in Kälte gewandelt werden. Darüber hinaus erhöht eine neuartige Betriebsoptimierung die Leistung um mehr als 50 % im Vergleich zu ohne deren Einsatz.

Auf Grundlage der Referenzbedingungen wird des Weiteren eine Leistungsuntersuchung für eine Variation der wesentlichen Einflussparameter durchgeführt: Die elektrische BSZ-Leistung und die Betriebstemperaturen. Die Variation der elektrischen BSZ-Leistung zwischen 1.8–7.9 kW resultiert in einer max. Kühlleistung von 807 W bei einer elektrischen Leistung von 7 kW, wobei eine spezifische Kälteleistung von 564 W kg_{MH}^{-1} bezogen auf einen Einzelreaktor erreicht wird. Die Leistungsfähigkeit nimmt mit steigenden Umgebungstemperaturen (variiert im Bereich von 24,3–42,3° C) und sinkenden Kältetemperaturen (variiert im Bereich von 13–25,4 °C) aufgrund erhöhter thermischer Verluste und reduzierter Halbzyklenzeiten ab.

Für eine weitere Erhöhung der Leistungsdichte wird der Plattenreaktor numerisch untersucht und Optimierungsmöglichkeiten aufgezeigt. Das validierte Modell zeigt, dass eine Steigerung der Kälteleistung durch Reduzierung des Wasserstofftransportweges, der Porosität des MH-Bettes sowie des BSZ-Gegendrucks erreicht werden kann. Bezogen auf die maximale Kälteleistung von 18,3 % der elektrischen BSZ-Leistung ist für dieses optimierte Design, selbst unter erschwerten Betriebsbedingungen, ein Kältewirkungsgrad von über 60 % realisierbar. Als innovativer „Wasserstoff-Druckminderer“ ist das System auf alle Anwendungen übertragbar, bei denen eine Wasserstoff-Druckdifferenz vorliegt.

Abstract

High-pressure tanks are the established hydrogen storage technology for automotive systems. However, around 15% of the lower heating value of hydrogen is required for compression up to a pressure of 700 bar. Since this energy is available onboard but has been wasted so far, an “open” cooling system based on metal hydrides (MHs) is a promising way to utilize the potential energy of compressed hydrogen. The thesis presents the systematic investigation of a first-of-its-kind system and a demonstration of the extent to which this energy can be transformed into useful cold.

For this purpose, an experimental setup is built that consists of two novel plate reactors coupled to a polymer electrolyte membrane fuel cell (FC). The reactors with an optimized heat transfer characteristic and an average heat transfer distance in the MH bed of 0.44 mm are filled with around 1.5 kg of Hydralloy® C2 ($Ti_{0.98}Zr_{0.02}Mn_{1.46}V_{0.41}Cr_{0.05}Fe_{0.08}$), which is thermodynamically characterized in the temperature range of 0–50 °C.

The functional demonstration at an electrical power of 5 kW shows that the FC operation is not affected by the alternately H_2-desorbing reactors with a half-cycle duration of 145 s. Hydrogen is absorbed at a pressure of 35 bar and a continuous flow rate is released at an FC backpressure of 4.1 bar. Under reference conditions for an ambient temperature of 30 °C and a cooling temperature of 20 °C, around 45% of the as-yet-unexploited potential energy of hydrogen at 700 bar can be utilized by generating a cooling effect. A novel operation optimization of time-shifted valve switching increases the performance by more than 50% compared to the case without its implementation.

Based on reference conditions, extensive performance investigations are performed while varying the key influencing parameters: the electrical FC power and the operating temperatures. The variation of the electrical FC power between 1.8 and 7.9 kW results in a maximum average cooling power of 807 W at an electrical power of 7 kW, reaching a specific cooling power of 564 W kg_{MH}^{-1} referred to the MH mass of a single reactor. The performance decreases with rising ambient temperatures (varied in the range of 24.3–42.3 °C) and decreasing cooling temperatures (varied in the range of 13–25.4 °C) due to increased thermal losses and reduced half-cycle times.

To further improve the performance, the plate reactor is numerically investigated and optimization recommendations are given. The validated model shows that an increase of the cooling power is obtained by reducing the distance of the hydrogen gas transport, the porosity of the MH bed and the FC backpressure. For this optimized system design, related to the maximum obtainable cooling power of 18.3% of the electrical FC power, cooling efficiencies above 60% are feasible even in harsher operating conditions. As an innovative “hydrogen pressure transducer”, the system can be transferred to all applications where a hydrogen pressure difference is available.

Publications

Parts of this thesis have been presented in the following publications:

Scientific Journals:

Weckerle C, Bürger I, Linder M, "Novel reactor design for metal hydride cooling systems", *Int J Hydrogen Energy*, vol. 42, pp. 8063–74, 2017.

Meier K, Kurtz C, Weckerle C, Hubner M, Bürger I, "Air-conditioning system for vehicles with on-board hydrogen", *Appl Therm Eng*, vol. 129, pp. 1150-9, 2018.

Weckerle C, Bürger I, Linder M, "Numerical optimization of a plate reactor for a metal hydride open cooling system", *Int J Hydrogen Energy*, vol. 44, pp. 16862–76, 2019.

Weckerle C, Nasri M, Hegner R, Linder M, Bürger I, "A metal hydride air-conditioning system for fuel cell vehicles – Performance investigations", *Appl Energy*, vol. 256, pp. 113957-71, 2019.

Weckerle C, Bürger I, Linder M, "Experimental demonstration of a metal hydride air-conditioning system for fuel cell vehicles - Functional demonstration", *Appl Energy*, vol. 259, pp. 114187-201, 2020.

Conferences:

Weckerle C, Bürger I, Linder M, "Reactor design for metal hydride based cooling systems", Presentation, in *WHEC 2016,* Zaragoza, Spain: 2016.

Weckerle C, Bürger I, Linder M, "Experimental analysis of a compact metal hydride based cooling system.", Poster presentation, in *Gordon Research Conference Hydrogen-Metal Systems,* Easton, USA: 2017.

Weckerle C, Dieterich M, Bürger I, Linder M, "Experimental analysis of a compact metal hydride based cooling system.", Poster presentation, in *WHTC - 7th World Hydrogen Technology Convention,* Prague, Czech Republic: 2017.

Weckerle C, Bürger I, Linder M, "An innovative hydrogen based air-conditioning system for fuel cell vehicles", Presentation, in *EHEC 2017,* Prague, Czech Republik: 2017.

Weckerle C, Bürger I, Linder M, "Eine Klimaanlage für Brennstoffzellenfahrzeuge auf Basis von Metallhydriden", Presentation, in *11. CTI-Jahrestagung Thermomangement im Gesamtfahrzeug,* München, Germany: 2018.

Patents:

Bürger I, Weckerle C, Postweiler P, Linder M, "Reaktor für ein Speichermaterial, welches unter Absorption bzw. Desorption eines Reaktionsgases Wärme aufnimmt bzw. abgibt…", DE102016110062B3, 2016.

Table of contents

Nomenclature, abbreviations and indices

Latin letters

Symbol	Description	Units
a	Corrugation amplitude	m
b	Width	m
c_p	Specific heat capacity	J kg^{-1} K^{-1}
d	Half channel thickness	m
E_a	Activation energy	J
f_g	Fanning friction factor	-
f_hys	Hysteresis factor	-
F	Hydrogen utilization factor	-
h	Specific enthalpy	J kg^{-1}
h_R	Reactor height	m
H_H2	Lower heating value of hydrogen	J kg^{-1}
ΔH	Heat of formation	J mol^{-1}
I	Current	A
k	Mass ratio	-
k_a	Absolute mass ratio	-
k_A	Rate coefficient (Arrhenius term)	s^{-1}
k_B	Boltzmann constant	J K^{-1}
K_0	Arrhenius coefficient	s^{-1}
K_i	Fitting parameters	-
l	Length	m
m	Mass	kg
$\dot{m}$	Mass flow rate	kg s^{-1}
m_pl	Plateau factor	wt. %$^{-1}$
M	Molar weight	kg mol^{-1}
$\dot{n}$	Molar mass flow rate	mol s^{-1}
$\vec{n}$	Normal vector	-
N	Number	-
p	Pressure	Pa
p_1	Initial pressure	Pa
p_2	Final pressure	
P_el	Electrical power	W
Pr	Prandtl number	-
$\dot{q}$	Specific cooling power	W kg$_\mathrm{MH}^{-1}$
$\dot{Q}$	Power	W
R	Universal gas constant	J mol^{-1} K^{-1}
Re	Reynolds number	-
ΔS	Entropy of reaction	J mol^{-1} K^{-1}
t	Time	s
T	Temperature	°C

u	Specific internal energy	$\mathrm{J\ kg^{-1}}$
$\vec{u}$	Gas velocity	$\mathrm{m\ s^{-1}}$
U	Voltage	V
v	Specific volume	$\mathrm{m^3\ kg^{-1}}$
$\dot{V}$	Volume flow rate	$\mathrm{m^3\ s^{-1}}$
w	Specific work	$\mathrm{J\ kg^{-1}}$
w_c	Specific work of compression	$\mathrm{J\ kg^{-1}}$
x	Transformed fraction	-
Z	Compressibility factor	-

Greek letters

α	Heat transfer coefficient	$\mathrm{W\ m^{-2}\ K^{-1}}$
β	Corrugation inclination angle	rad
γ	Kinematic viscosity	$\mathrm{m^2 s^{-1}}$
δ	Systematic uncertainty	-
Δ	Difference	-
ε	Porosity	-
η	Efficiency	-
κ	Permeability	$\mathrm{m^2}$
λ	Thermal conductivity	$\mathrm{W\ m^{-1} K^{-1}}$
λ_a	Corrugation wavelength	m
μ	Dynamic viscosity	$\mathrm{Pa\ s}$
μ_{JT}	Joule-Thomson coefficient	$\mathrm{K\ Pa^{-1}}$
ρ	Density	$\mathrm{kg\ m^{-3}}$
σ	Standard deviation	-
τ	Time constant	s
φ	surface enlargement factor	-
ψ	Ratio of specific heats	-
ω	Hydrogen capacity	$\mathrm{wt.\%}$

Subscripts

0	Standard
$\overline{\mathrm{ab}}$	Hydrogen outlet boundary
abs	Absorption
ac	Adiabatic compression
amb	Ambient
avg	Average
c	Cooling
cd	Compressed
cor	Corrected
cr	Critical
CHC	Cooling half-cycle
des	Desorption

eff	Effective
el	Electrical
ep	End plate
eq	Equilibrium
et	Equivalent
ex	Exergy
exp	Experiment
free	Free volume
g	Gaseous
h	Heating
hd	Hydraulic
H2	Hydrogen
i	Coefficient number
ic	Isothermal compression
in	Inlet
IG	Ideal gas
m	Modified
max	Maximum
mid	Middle
min	Minimum
out	Outlet
reg	Regeneration
re	Remaining
R1	Reactor 1
R2	Reactor 2
ref	Reference
RG	Real gas behaviour
RHC	Regeneration half-cycle
s	Solid
sim	Simulation
sl	Sensible heat losses
stat	Statistical
sw	Switching
sys	Systematic
SP	Separating steel plate
t	Total
tb	Tube
ts	Time shifted
tsd	Two-sided

Abbreviations

AC	Air-conditioning
AM	Ammeter
APU	Auxiliary power unit

C	Connection
Cool	Cooling
COP	Coefficient of performance
CP	Cooling phase
DOE	United States Department of Energy
DSD	Differential pressure sensor
ENG	Expanded natural graphite
FC	Fuel cell
FM	Flowmeter
FS	Full scale
GWP	Global warming potential
HC	Half-cycle
HIP	Heat input phase
HTF	Heat transfer fluid
HV	Hand valve
H&MT	Heat and mass transfer
LHV	Lower heating value
Me	Metal
MFC	Mass flow controller
MFM	Mass flowmeter
MH	Metal hydride
MHCS	Metal hydride cooling system
OPV	Overpressure valve
PCI	Pressure-concentration isotherm
PEM	Polymer electrolyte membrane
PRV	Pressure reducing valve
PS	Pressure sensor
PT	Pressure tank
PTC	Positive temperature coefficient
R	Reactor
Rd	Reading
Reg	Regeneration
RC	Reactor concept
RS	Reactor section
RV	Reference volume
SA	Sieverts area
SCP	Specific cooling power
SV	Sieverts volume
TB	Thermostatic bath
Temp.-dep.	Temperature-dependent
V	Valve
VP	Vacuum pump
VPS	Vacuum pressure sensor
VM	Voltmeter

1. Introduction

In the present thesis, a first systematic investigation and experimentally demonstration of an open MH cooling system (MHCS) for an automotive application is conducted. This system is driven by the as-yet-unexploited potential energy of compressed hydrogen in high-pressure tanks and, therefore, provides the possibility to increase the efficiency of fuel cell vehicles and the green mobile hydrogen cycle. In this chapter, initially, it is introduced why this is a relevant area of research. Then, the fundamentals of metal hydrides are illustrated and the detailed working principle of the present system is described. Concluding the chapter, a literature review including the state of the art in MHCSs is presented and the aim of the thesis is derived.

1.1 Motivation

The world in which we live would not be possible without transportation. However, the transport sector, being highly reliant on fossil fuels, contributes around 30% of global carbon dioxide gas emissions and is highly responsible for the deterioration of the urban air quality [1,2]. In order to diminish these emissions and to reduce the dependency on fossil fuels, vehicle electrification and a shift towards a low-emission and more efficient mobility are seen as the main decarbonization pathway [3,4].

Owing to their different chemical and physical properties, it is expected that this vehicle electrification will include both battery electric vehicles and fuel cell (FC) vehicles [5,6]. In an FC vehicle, hydrogen reacts with oxygen electrochemically in an FC to produce heat as well as electricity, which is used for propulsion [7]. As hydrogen has the highest energy densities by mass, FC vehicles offer long driving ranges of above 500 km and compressed hydrogen storage enables a fast refuelling within 3–5 minutes [3]. Therefore, these vehicles are particularly attractive for high-utilization transportation and long-range electrical vehicles. When hydrogen as the energy carrier is produced from renewable energy resources, a low-carbon means of transportation is facilitated [8].

There are, however, still some technical barriers that have to be overcome in order to increase the deployment of FC vehicles. A great barrier is the current lack of hydrogen infrastructure and the low efficiency of the green mobile hydrogen cycle [3,9]. This hydrogen cycle includes electrolysis of water, distribution and compression of hydrogen and the reconversion to electrical power in an FC vehicle as shown in Figure 1-1. Due to the low volumetric calorific value of 0.01 MJ dm^{-3} at standard conditions [10], hydrogen compression is required in order to reach the demanded energy densities. For the state-of-the-art 700 bar storage tanks used for automotive applications, around 15% of the gravimetric calorific value of hydrogen H_{H2}

(also referred to as the lower heating value) is consumed for the compression [11]. However, since a polymer electrolyte membrane (PEM) FC requires a backpressure of only around 3–10 bar, at present, hydrogen from the storage tank is throttled down and the work of compression w_c, which is available as potential energy of compressed hydrogen in the storage tank is lost.

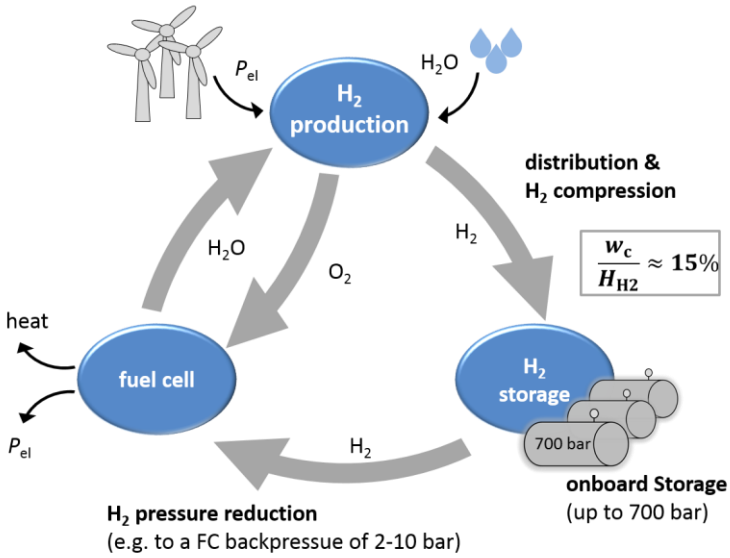

Figure 1-1: Illustration of the green mobile hydrogen cycle based on [3,9]. The compression to 700 bar requires around 15% of the lower heating value of hydrogen [11].

Furthermore, in terms of energy density, the onboard available chemical energy in the hydrogen storage tank is a very precious resource. Currently, electrically operated systems based on the vapour compression cycle are used for cooling, while a positive temperature coefficient (PTC) heater provides heat in the absence of waste heat from the combustion engine [12]. However, as the required electrical power is provided by the chemical energy of hydrogen, these auxiliary systems substantially decrease the driving range of electrical vehicles [13,14]. For instance, Pino et al. [15] demonstrated an increase of hydrogen consumption of up to 12.1% when an electrical compressor-driven air-conditioning (AC) system is in operation. Additionally, these systems require the use of refrigerants, which are currently flammable or show a high global warming potential (GWP) [16]. To encourage the development of novel working fluids, the European Union has passed a regulation to prohibit the use of chemical refrigerants with a GWP higher than 150 [17].

Due to the increased (hydrogen) fuel consumption and the climate-damaging effect of current refrigerants, research and development has been focused on innovative solutions for mobile AC systems. The objective is to reduce the energy consumption onboard while guaranteeing the passenger comfort. A very promising technology to improve FC vehicle thermal management without the consumption of electrical energy is an open metal hydride (MH) heating and cooling system. This system uses the as-yet-unexploited potential energy of compressed hydrogen as a driving force for providing heat and cold. Thus, it enables a

reduction of the onboard energy consumption and an increase in the efficiency of the green mobile hydrogen cycle. The operation principle is based on the exothermic or endothermic reversible gas–solid reaction of a metal with hydrogen and the dependency of the MH equilibrium temperature on the hydrogen pressure. The system utilizes the hydrogen available onboard as a working fluid (no additional refrigerant is required) and since MH enables very short reaction times and has a high heat of formation, mobile systems with high power densities are feasible [18]. In this work, a systematic investigation of such an open MHCS is conducted. Thereby, the focus is on the cooling operation. This includes a first functional demonstration of this novel system and a qualitative analysis of the extent to which the potential energy of hydrogen can be transformed into a cooling effect. Compared to other sorption systems which have been investigated in several literature studies [19,20], higher power densities are feasible with this system as no additional driving force (e.g. a heat source) is required and the number of system components is reduced. In the following the MH fundamentals are presented, which are crucial for the open MHCS.

1.2 Metal Hydride Fundamentals

MHs are generally a class of hydrogen compounds that are formed by absorbing hydrogen in the interstitial lattice sites of the metal. In this section, a brief introduction to MHs is given and the main characteristics that will be important for this thesis are presented. Then, the requirements for the reactor design which have to be considered in order to obtain a high performance of the present MHCS are illustrated.

The reversible gas–solid reaction of gaseous hydrogen (H_2) and a metal (Me) to form a metal hydride (MH_x) can be written as

$$\mathrm{Me} + \frac{x}{2}\mathrm{H_2} \rightleftharpoons \mathrm{MH}_x + \Delta H. \tag{1-1}$$

Here, x denotes the non-stoichiometric coefficient and ΔH is the reaction enthalpy. Corresponding to the principle of Le Chatelier-Braun, a rise of temperature shifts the equilibrium to the left side in equation (1-1), while an increase of pressure moves it to the right [21]. Thus, the release of hydrogen is enabled by either reducing the hydrogen pressure or increasing the MH temperature. The exothermic or endothermic character of the reaction can be used to generate a heating or cooling effect, respectively.

The majority of the metals from the Periodic Table of the Elements are able to build MHs [22]. However, most of the pure low electro-negative metals or A-metals (such as magnesium, calcium, zirconium and titanium) are active hydride elements forming very stable hydrides that require low hydrogen pressures or high temperatures to release hydrogen. Compared to this, more electro-negative metals or B-metals (such as nickel, cobalt, iron, manganese and

chromium) are very unstable and, therefore, need very high pressures to bond hydrogen at moderate temperatures. In order to obtain alloys with practicable and intermediate characteristics, these active hydride-forming elements A and non-hydride-forming metals B are combined to form intermetallic compounds [23]. The intermetallic compounds are usually classified in accordance with their stoichiometry as follows: AB (e.g. TiFe, LaNi), AB_2 (e.g. $TiMn_2$, $ZrMn_2$), AB_5 (e.g. $LaNi_5$, $CaNi_5$) and A_2B (e.g. Zr_2Cu, Ti_2Pd) [24]. A further option is the classification into low-temperature, medium-temperature and high-temperature MHs according to their equilibrium temperature at a hydrogen equilibrium pressure of 1 bar [25].

Through the partial substitution of alloy elements, the thermodynamic equilibrium characteristics and reaction kinetics can be varied and adapted to the desired specifications [26–28]. For instance, for the $Ti_{1.1}CrMn$ system [29], a part of the titanium atoms are replaced by zirconium. It was found that the equilibrium plateau pressures decrease and the material also shows faster absorption kinetics with an increase of the zirconium content. In the present thesis, the low-temperature metal hydride Hydralloy® C2 ($Ti_{0.98}Zr_{0.02}Mn_{1.46}V_{0.41}Cr_{0.05}Fe_{0.08}$) based on the alloy $TiMn_2$ is applied, whose characteristics and selection criteria are described in Chapter 2.1.

1.2.1 Thermodynamics

A main characteristic of MHs is their thermodynamic equilibrium, which defines the temperature and pressure conditions under which hydrogen is absorbed or desorbed by the material. Thus, in order to select a suitable MH for a certain application, it is very important to know this information.

The thermodynamic equilibrium characteristics of MHs are commonly determined by pressure–concentration isotherms (PCIs). The left part of Figure 1-2 shows schematic PCIs, in which the equilibrium pressure in logarithmic scale is shown versus the hydrogen capacity. The hydrogen capacity ω is defined as the ratio of absorbed hydrogen mass m_{H2} to the MH mass m_{MH}:

$$\omega = \frac{m_{H2}}{m_{MH}} \tag{1-2}$$

The shape of a single PCI shows three characteristic regions that can be described as follows: In the α-region, hydrogen starts to dissolve into the metal lattice. The hydrogen atoms are randomly distributed in the metal and the increase of pressure follows Sieverts´ law, where the hydrogen capacity is proportional to the square of the hydrogen equilibrium pressure ($\omega \sim \sqrt{p_{eq}}$). When the saturation limit of the solution is reached (see point 1 on the isotherm T_1), the material starts to actually form a hydride by occupying interstitial lattice sites. The α-phase is transformed into the β-phase and the characteristic plateau region ($\alpha + \beta$-region) is reached. Under idealized equilibrium conditions, in the plateau region

the hydrogen pressure remains constant with increasing hydrogen capacity following Gibbs´ Phase Rule. At point 2 and the end of the plateau, the α-phase is completely converted into the β-phase. For a growing hydrogen capacity in the β-phase, a pressure increase is required, which follows Sieverts´ law again. In this phase, the hydrogen atoms lie in an organized structure inside the MH. The plateau ends at the critical point T_{cr}, p_{cr} above which the conversion from α-phase to β-phase occurs continuously. [7,30]

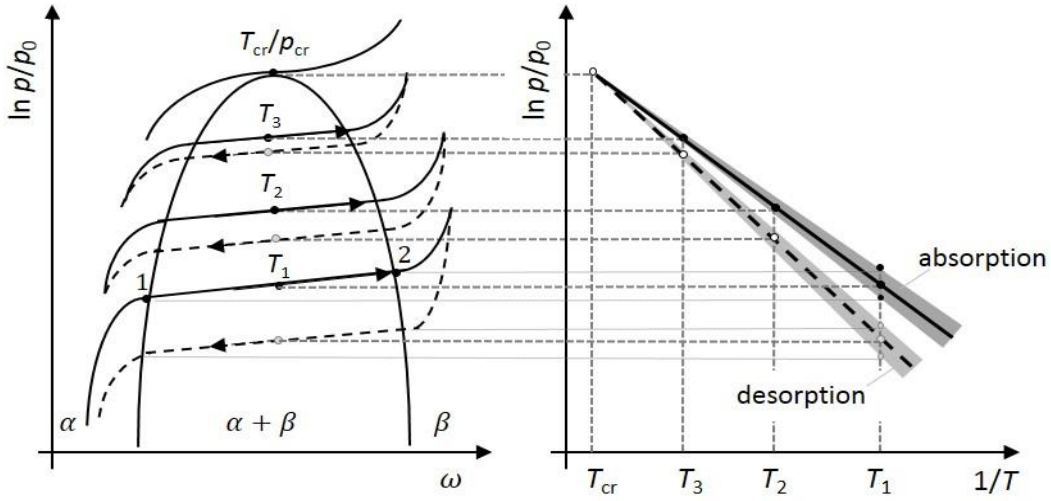

Figure 1-2: Schematic pressure-concentration isotherms (left) and van´t Hoff plot (right) of a real MH.

The following characteristics and parameters, which are important for the practical application of MHs, for example in the present open MHCS, are directly obtained from the PCIs.

Plateau slope

The plateau region is of particular importance since in this area the applied MH reversibly absorbs or desorbs a large quantity of hydrogen. Thereby, the length of the plateau characterizes the hydrogen capacity of the material. However, according to Figure 1-2, real MHs show a slope in the plateau region, which means that the equilibrium pressure in the $\alpha + \beta$ -region depends on the hydrogen capacity ω. This plateau slope is caused by inhomogeneities on the surface, impurities and stresses [30]. Commonly, one plateau factor m_{pl} for the absorption and the desorption, derived at the middle of the plateau ω_{mid}, is applied to describe the plateau characteristics (p_0 corresponds to the standard pressure) [31]:

$$m_{\mathrm{pl}} = \left.\frac{d\left(ln\frac{p_{\mathrm{eq}}}{p_0}\right)}{d\omega}\right|_{\omega_{\mathrm{mid}}} \tag{1-3}$$

Hysteresis

Corresponding to Figure 1-2, for a real MH the equilibrium pressure of absorption (solid line) is higher than the equilibrium pressure of desorption (dashed line). In the literature, this hysteresis effect is explained by the induced stresses and the lattice expansion during the formation of the hydride phase, therefore requiring a higher hydrogen pressure for the absorption [30]. The hysteresis factor f_{hys} is expressed quantitatively by a difference in free energy and can be determined as follows [32]:

$$f_{\mathrm{hys}} = \ln\left(\frac{p_{\mathrm{abs}}}{p_{\mathrm{des}}}\right)\Big|_{\omega_{\mathrm{mid}}} \tag{1-4}$$

Here, p_{abs} and p_{des} are the equilibrium pressures for absorption and desorption, which are determined in the middle of the plateau at the same temperature. For the present open MHCS, a small hysteresis and a low plateau slope are desired as both effects reduce the useful hydrogen capacity and the efficiency of the system.

Van´t Hoff plot

From the PCIs at different temperatures, the plateau pressure and temperature in the middle of the plateau can be transferred to obtain the characteristic van´t Hoff plot. The right part of Figure 1-2 illustrates such a van´t Hoff plot for a real MH, in which the plateau pressure is plotted against the inverse equilibrium temperature T_{eq}. Due to the hysteresis, the plot consists of two lines for the absorption and desorption, and the shaded areas illustrate the effect of the plateau slope.

The corresponding relation between the equilibrium pressure and temperature in the plateau region is given by the van´t Hoff equation [33]:

$$\ln\left(\frac{p_{\mathrm{eq}}}{p_0}\right) = \frac{-\Delta H}{R} \cdot \frac{1}{T_{\mathrm{eq}}} + \frac{\Delta S}{R} \tag{1-5}$$

From equation (1-5), two important material properties can be obtained. The slope of the van´t Hoff equation can be linked to the reaction enthalpy ΔH, whereas the intersection with the ordinate is equal to the entropy of reaction ΔS divided by the universal gas constant (separate equations for absorption and desorption).

Even though the values of reaction enthalpy and entropy are not independent from temperature, using a constant value for ΔH and ΔS in low operating temperature ranges is reasonable [34]. The van´t Hoff plot makes it possible to quickly identify a suitable MH for a certain application, which is specified by the desired operating temperature and hydrogen pressure conditions. The thermodynamic equilibrium characteristics of Hydralloy® C2 will be given in Chapter 2.1.

1.2.2 Reaction kinetics

The reaction kinetics are an another important property of MHs. While the thermodynamics describe states of equilibrium, the reaction kinetics characterize how fast the chemical reaction can take place.

In general, the MH material absorbs hydrogen through the occupation of interstitial lattice sites in the metal. Due to the small size of the hydrogen atoms and the resulting high diffusivity of hydrogen in the metal lattice, the hydration is a very fast process. The study by Martin et al. [35] describes the MH reaction pathway in detail and divides the hydrogen absorption reaction in a metal into five consecutive steps (see Figure 1-3): (i) physisorption of hydrogen molecules on the surface of the metal, (ii) dissociation and chemisorption of hydrogen molecules, (iii) diffusion of hydride atoms from the surface into the bulk through a surface layer, (iv) diffusion of hydrogen atoms through the hydride and (v) hydride formation at the MH interface. The corresponding desorption reaction takes place in reverse order. For each of these consecutive reaction steps, based on physical assumptions, complex mathematical functions with a large number of parameters exist to describe the intrinsic reaction kinetics, as has been done, for example in [35]. These assumptions include a uniform particle distribution and a perfect geometry of the particles, all of which can cause inaccuracies in the model for the intrinsic reaction kinetics [36].

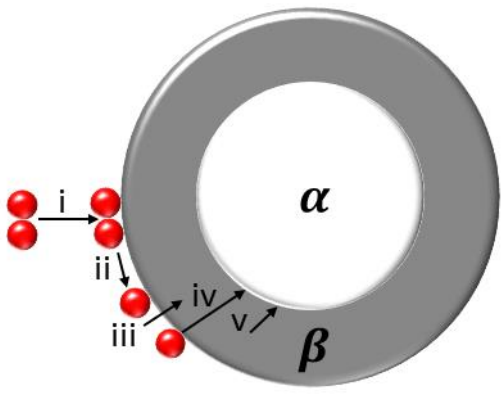

Figure 1-3: Illustration of the steps involved in the MH reaction based on [7,35].

For the titanium manganese alloy applied in this thesis, intrinsic kinetic measurements have proven that very high reaction rates and a full transformed fraction can be reached within seconds. For instance, for the desorption into vacuum with a hydride temperature of 20 °C, a full transformed fraction was obtained in 10 s [37]. Due to the very fast kinetics of most MH materials, it has been pointed out that the overall behaviour in the reaction bed is mainly dominated by heat and mass transfer limitations (referred to as reactor bed dynamics), and not by the intrinsic reaction kinetics [38–40].

For the purposes of reactor design, therefore, a simplified empirical expression to describe the effective reaction rate $\frac{\partial x}{\partial t}$ of the gas–solid reaction is usually applied according to [41]:

$$\frac{\partial x}{\partial t} = k_{\mathrm{A}}(T) \cdot f\left(p, p_{\mathrm{eq}}\right) \cdot f(x) \tag{1-6}$$

In this equation, the transformed fraction $x(t)$ is defined as the ratio of the hydrogen capacity $\omega(t)$ to the maximum reversible hydrogen capacity $\omega_{\max}$:

$$x(t) = \frac{\omega(t)}{\omega_{\max}} \tag{1-7}$$

Equation (1-6) focuses on only one rate-limiting step of the reaction and considers the evolution of transformed fraction [42]. The Arrhenius term $k_{\mathrm{A}}(T)$ describes the temperature dependency of the reaction, whereas the functions $f\left(p, p_{\mathrm{eq}}\right)$ and $f(x)$ describe the dependency of the effective reaction rate on the thermodynamic equilibrium and the reaction mechanism, respectively. The terms of these functions for the material used in this thesis will be given in Chapter 5.

1.2.3 Requirements for the reactors design

In the MH reactor, a coupling process of heat and mass transfer, and the chemical reaction occurs, which includes the reaction kinetics and thermodynamics of the applied MH. Due to these challenging characteristics, the reactor is the crucial component for all types of MH applications (see the schematic illustration in Figure 1-4). Limitations by the intrinsic kinetics of the MH can be excluded when an appropriate MH is selected. Commonly, indirect reactor concepts are applied, where the corresponding heat of formation is transferred from or to an external heat transfer fluid (HTF). The performance-limiting criteria and requirements that have to be considered in the reactor design for a high-performance system (including the present MHCS) can be divided into four main aspects, which are discussed in the following.

- Heat transfer characteristics
- Hydrogen mass transfer characteristics
- Sensible mass of the reactor
- Mechanical stability

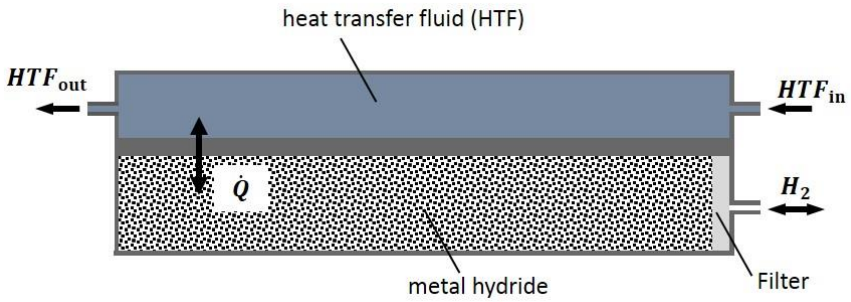

Figure 1-4: Schematic illustration of an MH reactor.

Heat transfer characteristics

The heat transfer in the MH reactor can be generally divided into the internal heat transfer in the MH bed, the heat transfer by conduction in the wall separating the MH from the HTF and the external heat transfer in the HTF by convection [43].

The MH is mostly packed as a fine powder with a small average particle size of around 10 µm in the void reactor volume [44,45]. The internal heat transfer in the porous MH bed occurs through a combination of conduction in the solid MH particles and in the hydrogen filler gas, as well as through radiation between the particle surfaces and partially through convection [36,46]. The resulting total heat transport is expressed by the effective heat conductivity λ_{eff}. Since MHs have a low effective heat conductivity in the range of 1 W $m^{-1}K^{-1}$ [47–49], previously published studies pointed out that the reactor performance for high-performance systems is mainly limited by the internal heat transfer [50,51]: when the heat flow supplied (desorption) or dissipated (absorption) is lower than the respective heat flux due to the chemical reaction, the material reaches equilibrium and the hydride formation or decomposition stops. According to Fourier´s law, the internal heat transfer can be improved by either increasing the thermal conductivity of the MH bed or reducing the heat transfer distance. To increase the thermal conductivity, several measures are proposed in the literature such as inserting heat transfer enhancement matrices [52–55] or mixing of the powder with expanded natural graphite (ENG) and compression into MH compacts [56–59]. However, these measures reduce the available MH capacity and increase the reactor mass [60]. The second option, namely reducing the heat transfer distance from the MH bed to the HTF, is applied in the reactor design of this thesis.

In contrast, the external heat transfer in the HTF is considered as less limiting, especially when the HTF is a liquid and is in the state of turbulent flow. References [61,62] illustrated that an increase of the external convective heat transfer coefficient beyond 1000 W $m^{-2}K^{-1}$ has less effect on the performance of the reactor. However, if the HTF is a gas and has a low flow velocity, the thermal resistance can be in the range of the MH bed and improving the external heat transfer, for example by using fins to increase the heat transfer area, is reasonable. Due

to the high thermal conductivity of the reactor materials (for instance aluminium or stainless steel), the thermal resistance of the separating wall is generally negligible [40].

Hydrogen mass transfer characteristics

The chemical reaction of MHs only takes place when an efficient supply or removal of the hydrogen gas is enabled. However, due to the hydrogen flow in the porous MH powder bed, a pressure drop occurs. According to Darcy´s law, the pressure gradient ∇p is related to the gas velocity $\vec{u}$:

$$\vec{u} = -\frac{\kappa}{\mu}\nabla p \tag{1-8}$$

Here, κ is the permeability of the MH bed and μ is the dynamic viscosity of hydrogen. The pressure drop depends correspondingly on the physical properties of the MH and can be minimized by reducing the mass transfer distance. Thus, a common applied method is the implementation of a gas artery that enables a uniform distribution of hydrogen in the reaction bed. A filter tube with fine pores for MH powder beds [63,64] or a drilled hole in the centre of MH compacts [65,66] are usually implemented. By the integration of such a filter into the gas supply, the MH powder extraction caused by particle entrainment is additionally avoided.

Sensible mass of the reactor

The sensible (parasitic) reactor mass is a crucial characteristic as thermal energy is consumed to heat or cool the reactor and the MH mass, when absorption and desorption occurs at two different temperature levels. The resulting sensible heat losses are particularly of interest in continuously operating MH systems, as the temperature change significantly decreases the system performance (e.g. in MH heat pumps or cooling systems [67,68]). Its effect is an intrinsic system property and the mass ratio k of passive reactor mass m_{R} to active MH mass m_{MH}, as given in equation (1-9), can be introduced for a comparison of different reactor designs:

$$k = \frac{m_{\mathrm{R}}}{m_{\mathrm{MH}}} \tag{1-9}$$

The value of k should be generally kept as small as possible. However, the mass ratio commonly increases if measures to improve the heat transfer characteristic are applied. Thus, there is a conflict of objectives between avoiding heat transfer limitations on the one hand and reducing the sensible heat losses on the other hand, and this is an important aspect of the present thesis.

Mechanical stability

A further challenge in the reactor design is the mechanical stability of the reactor, which is partially in conflict with the aforementioned performance-limiting criteria. Mechanical strains

caused by the expansion of the MH lead to mechanical stresses on the reactor wall, beside the hydrogen pressure and the thermomechanical strains (Heubner et al. [69] demonstrated axial mechanical stresses of up to 85 bar). These mechanical stresses depend on a variety of aspects, for example porosity, cycle number and hydrogen supply, and are a result of different mechanisms in the reaction bed [70,71]. Through the phase change during absorption and desorption, a cyclic swelling and shrinking of the material, called the breathing of the material, occurs [72]. For AB_2 materials this swelling can be larger than 20% [73]. In addition, during the activation procedure in the first hydrogenation cycles the material fragments into fine powder. This decrepitation is associated with a densification and a segregation effect with higher local stresses at the bottom of the reactor caused by the larger number of small grains in this section [74,75]. Thus, a decreasing variation of the hydride bed volume during hydration and dehydration occurs with an increased number of cycles. For a Ti-Cr-V + Zr-Ni alloy as an example, the variation of the bed volume reaches a constant level after around 30 cycles [76]. To reduce the mechanical strains caused by the expansion, it is generally recommended that a critical initial packing fraction (generally larger than 0.4 [40]) should not be exceeded. Furthermore, a reduction in the vertical height of the reactor is reasonable and pre-processing of the MH powder (e.g. pre-cycling in highly pressure-resistant containers or MH powder encapsulation) makes it possible to limit to effect of pulverization.

1.3 Open MH cooling system

Based on the presented fundamentals of the MH, in the following the detailed working principle of the open MHCS for FC vehicles is presented. As the cooling power output is the crucial characteristic of this system, furthermore, this section analyses which parameters particularly affect the performance and which aspects have to be considered especially in order to reduce sensible heat losses.

1.3.1 Working principle

The general operation principle of the open MHCS is based on the endothermic desorption of hydrogen according to equation (1-1) and the dependency of the MH equilibrium temperature on the hydrogen gas pressure.

Figure 1-5 shows a schematic illustration of its working principle through a van´t Hoff plot. In this system, an MH reactor is integrated between the pressure tank and the FC in the hydrogen pathway of an FC vehicle. Thereby, the system operates in two successive states of operation at two different pressure levels – the absorption pressure p_{abs} supplied by the hydrogen storage tank and the FC backpressure p_{FC}. In the regeneration half-cycle (HC), the MH reactor is initially charged with hydrogen from the pressure tank. The heat of formation of the exothermic reaction has to be released to the ambient environment during the cooling

operation (cf. conventional heat pumps), or, in case of low ambient temperatures, it can be used for (pre-)heating. When the reactor is completely charged with hydrogen, it is connected to the FC. The desired cooling effect considered in this thesis results from the subsequent desorption of hydrogen at a reduced FC backpressure p_{FC} by taking up heat at low temperature T_{c} in the endothermic cooling HC.

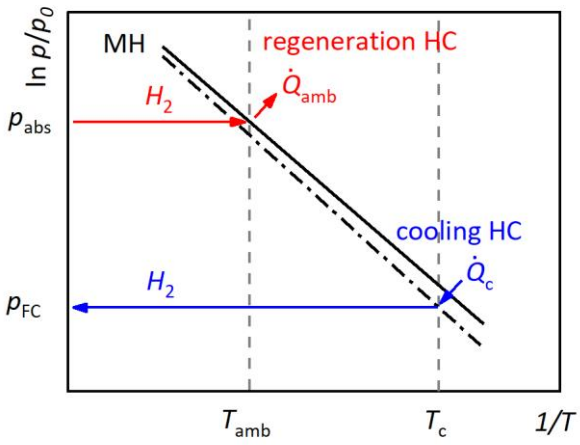

Figure 1-5: Schematic illustration of the working principle of the open MHCS in the van´t Hoff plot.

In order to guarantee a continuous supply of hydrogen to the FC and to obtain a continuous cooling effect, at least two identical MH reactors that alternately pass through the regeneration HC and cooling HC are required. Figure 1-6 illustrates a detailed integration concept of the open MHCS with the reactors R1 and R2. According to this, while reactor R2 absorbs hydrogen from the pressure tank, reactor R1 supplies hydrogen to the FC in the 1st HC (top) and vice versa in the 2nd HC (bottom).

The corresponding absorption pressure is adjusted by the pressure reducing valve PRV1 and the pressure reducing valve PRV2 protects the FC from exceedingly high pressure. A pressure ratio of around 6 to 10 between absorption and desorption is commonly sufficient to generate satisfactory cooling effect. In order to provide the required heat for the endothermic desorption and to take up the heat of formation in the regeneration HC, two independent HTF loops (cooling HTF loop and ambient HTF loop) flow alternately through the reactors. Their corresponding flows are changed by means of three-way HTF valves at each reactor inlet and outlet. The HCs are switched when the reactor outlet pressure, which decreases during the desorption of hydrogen, is close to the required FC backpressure. The system is called “open”, since hydrogen continuously passes the open MHCS from the pressure tank to the FC (no hydrogen is consumed). A bypass allows hydrogen mass flow directly from the pressure tank to the FC in case of low hydrogen pressures in the storage tank or when very high hydrogen mass flow rates are required for the propulsion in case of peak demands of the electrical FC power.

As the system is purely driven by the onboard available potential energy in the hydrogen storage tank (no electrical energy is required except for HTF pumps and valves), it is a promising way for improving the efficiency of FC vehicles and the green mobile hydrogen cycle by providing heat or cold. Additionally, environmentally friendly hydrogen is used as a working fluid and there is no need for additional refrigerant, options for which are currently flammable or show a high GWP.

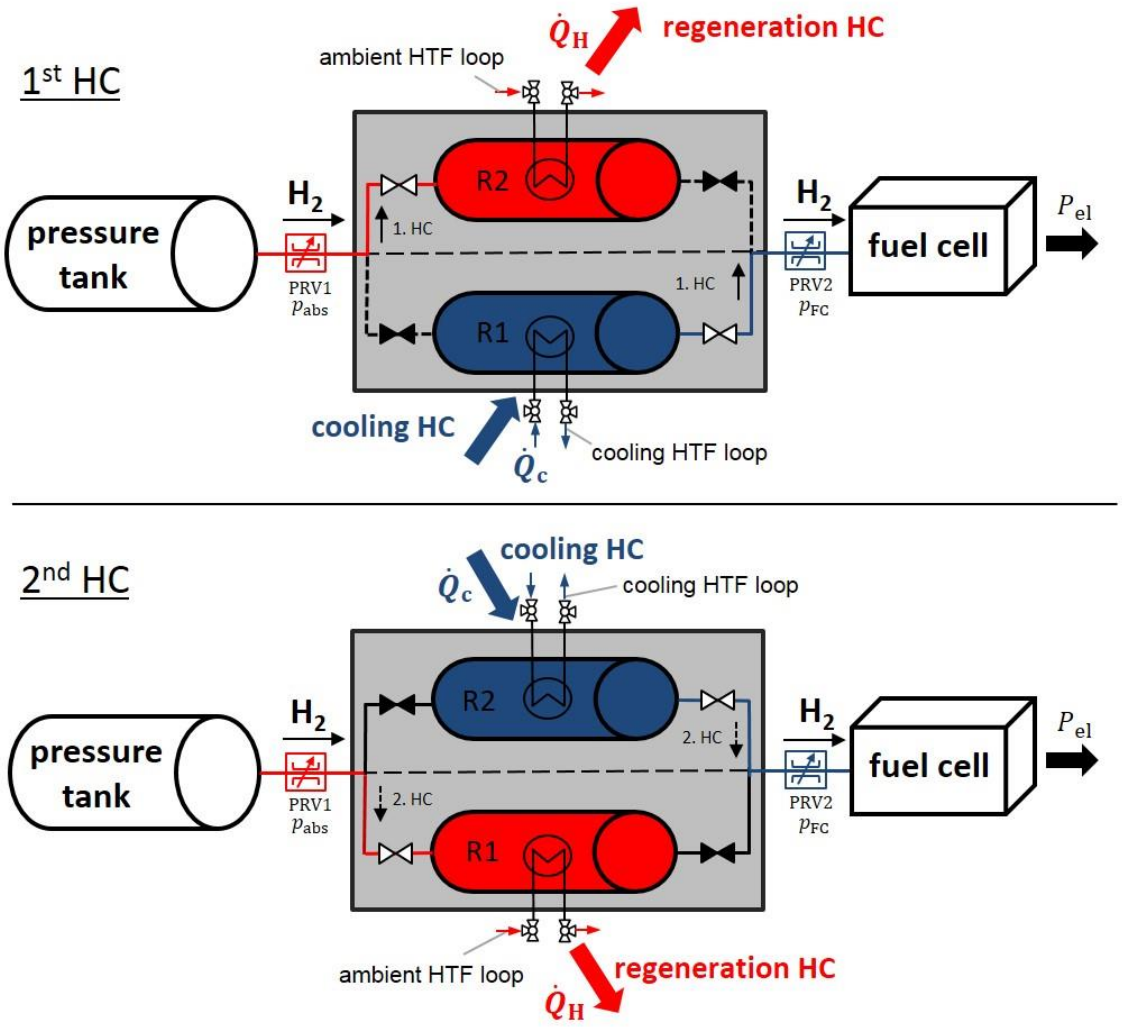

Figure 1-6: Integration concept of the open MHCS in the hydrogen pathway of an FC vehicle. Top: Illustration of the 1st HC. Bottom: Illustration of the 2nd HC.

1.3.2 Cooling power

The cooling power output is the crucial performance characteristic of the open MHCS. In this section, it is analytically described, which parameters affect the performance in particular. This real characteristic is experimentally investigated and demonstrated in the main part of the thesis.

The cooling power of the open MHCS results from the absorbed heat at low temperature T_c during the endothermic desorption of hydrogen in the cooling HC. The maximum obtainable cooling power (also referred to as reaction power)

$$\dot{Q}_{\mathrm{max,des}} = \dot{n}_{\mathrm{H2}}\, \Delta H_{\mathrm{des}}, \tag{1-10}$$

depends directly on the desorption reaction enthalpy ΔH_{des} of the MH and the desorbed molar mass flow rate $\dot{n}_{\mathrm{H2}}$. Since this molar mass flow rate is converted to electrical energy in the FC according to

$$P_{\mathrm{el}} = \eta_{\mathrm{FC}} H_{\mathrm{H2}} M_{\mathrm{H2}} \dot{n}_{\mathrm{H2}}, \tag{1-11}$$

there is an intrinsic dependency of $\dot{Q}_{\mathrm{max,des}}$ on the electrical FC power P_{el}. In equation (1-11), η_{FC} is the FC efficiency, ΔH_{H2} depicts the lower heating value of hydrogen and M_{H2} is the molar mass of hydrogen. For instance, for an electric power of $P_{\mathrm{el}} = 5\ \mathrm{kW}$ and an FC efficiency of $\eta_{\mathrm{FC}} = 0.5$ (corresponding to a hydrogen mass flow rate $\dot{m}_{\mathrm{H2}} = M_{\mathrm{H2}} \dot{n}_{\mathrm{H2}}$ of $5\ \mathrm{g\ min^{-1}}$), the theoretical maximum cooling power is $\dot{Q}_{\mathrm{max,des}} = 915\ \mathrm{W}$. Thus, there is a maximum ratio of cooling power to electrical FC power (depending on the FC efficiency) of

$$\frac{\dot{Q}_{\mathrm{max,des}}}{P_{\mathrm{el}}} = 18.3\%. \tag{1-12}$$

These values are calculated using the reaction enthalpy of the applied MH Hydralloy® C2 ($\Delta H_{\mathrm{des}} = 21.9\ \mathrm{kJ\ mol^{-1}}$), whose thermodynamic equilibrium characteristics and material properties are determined in Chapter 2.1. Due to the continuous operation at the two temperature levels T_{amb} and T_c, sensible heat losses occur, as part of the reaction enthalpy is required to cool the MH and the sensible reactor mass while switching from the regeneration HC to the cooling HC according to:

$$\dot{Q}_{\mathrm{sl}} = \frac{(m_{\mathrm{MH}} c_{\mathrm{p,MH}} + m_{\mathrm{R}} c_{\mathrm{p,R}}) \Delta T}{t_{\mathrm{HC}}} \tag{1-13}$$

Here, m_{MH} and $c_{\mathrm{p,MH}}$ are the mass and specific heat capacity of the MH, m_{R} and $c_{\mathrm{p,R}}$ correspond to the mass and specific heat capacity of the reactor, and $\Delta T = T_{\mathrm{amb}} - T_c$ is the temperature difference between the operating temperature levels. The HC time t_{HC} is defined as duration of the cooling HC, in which one reactor supplies hydrogen to the FC before the FC backpressure is reached. The average cooling power $\dot{Q}_{\mathrm{avg}}$ of the system is defined as the difference between the maximum obtainable cooling power and the sensible heat losses:

$$\dot{Q}_{\mathrm{avg}} = \dot{n}_{\mathrm{H2}}\, \Delta H_{\mathrm{des}} - \frac{(m_{\mathrm{MH}} c_{\mathrm{p,MH}} + m_{\mathrm{R}} c_{\mathrm{p,R}}) \Delta T}{t_{\mathrm{HC}}} \tag{1-14}$$

When the average cooling power is divided by the necessary mass of alloy, the specific average cooling power $\dot{q}_{\mathrm{avg}}$ per kilogram of MH is derived:

$$\dot{q}_{\mathrm{avg}} = \underbrace{\frac{\dot{n}_{\mathrm{H2}}\,\Delta H_{\mathrm{des}}}{m_{\mathrm{MH}}}}_{\dot{q}_{\mathrm{max,des}}} - \underbrace{\frac{k_{\mathrm{a}}}{t_{\mathrm{HC}}}\,c_{\mathrm{p,avg}}\Delta T}_{\dot{q}_{\mathrm{sl}}} \tag{1-15}$$

In the above expression, the absolute mass ratio is given by $k_{\mathrm{a}} = (m_{\mathrm{MH}} + m_{\mathrm{R}})/m_{\mathrm{MH}}$ and $c_{\mathrm{p,avg}}$ depicts the average specific heat capacity of the MH and the reactor.

In order to illustrate the extent to which the reactor design affects the specific average cooling power, Figure 1-7 schematically compares two different reactor concepts. Reactor concept 1 (RC1) is characterized by ideal heat and hydrogen mass transfer (H&MT) characteristics, which is schematically shown on left part of Figure 1-7. Therefore, a limitation of the chemical reaction during the release of hydrogen is avoided. However, to achieve these characteristics, it is necessary to take several measures which tend to increase the absolute mass ratio (e.g. insertion of fins or heat transfer enhancement matrices). In contrast to this, reactor concept 2 (RC2) shows poor heat and mass transfer characteristics (e.g. a high heat transfer distance from the MH to the HTF), but a low value of k_{a} is reached.

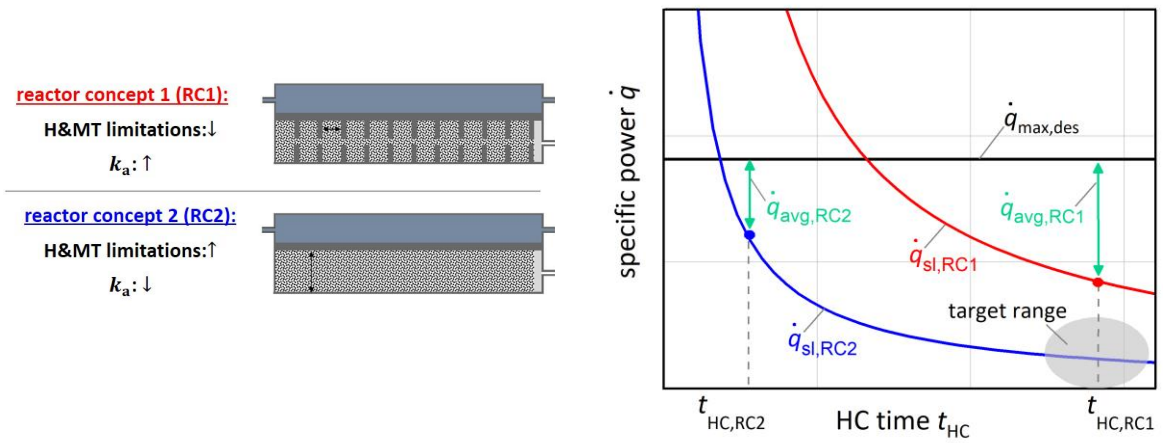

Figure 1-7: Schematic comparison of two different reactor concepts. Left: Illustration of the concepts RC1 and RC2. Right: Specific power as a function of the half-cycle time.

From equation (1-15), it is obvious that the specific reaction power $\dot{q}_{\mathrm{max,des}}$ is purely affected by the reaction enthalpy of the MH and the desorbed molar mass flow rate (increases with growing electrical FC power), but it is independent of the design of the reactor. Therefore, the profile of $\dot{q}_{\mathrm{max,des}}$ on the right part of Figure 1-7 is valid for both reactor concepts in the case of the same operating conditions and equal MH capacities. In contrast to this, the layout of the reactor significantly determines the sensible heat losses and, thus, the cooling power output of the system: due to the low value of k_{a}, RC2 (shown in blue) shows smaller specific sensible power losses $\dot{q}_{\mathrm{sl}}$ for equal HC times compared to RC1 (shown in red). However, the

resulting duration of the cooling HC is defined by the heat and mass transfer characteristics of the reaction bed. For instance, in the case of heat transfer limitations, the heat flow supplied is lower than the heat flux required for the desorption. Thus, the MH cools down and low equilibrium pressures are reached. As soon as the reactor pressure is equal to the minimum required FC backpressure, the HC is completed and no more hydrogen can be released even though no completely transformed fraction is obtained. For this reason, in this example, RC2 shows a reduced HC time ($t_{\mathrm{HC,RC2}}$) compared to RC1 ($t_{\mathrm{HC,RC1}}$) and less of the available MH capacity is utilized. As the difference between $\dot{q}_{\mathrm{max,des}}$ and the corresponding values of $\dot{q}_{\mathrm{sl}}$, the green arrows depict the values of specific average cooling power $\dot{q}_{\mathrm{avg}}$ of RC1 and RC2, respectively.

From this schematic comparison, two aspects are crucial for the reactor design in order to obtain the maximum system performance of the open MHCS: On the one hand, heat and mass transfer limitations in the MH bed have to be avoided to reach a high duration of the cooling HC and a high utilization of the available MH capacity (characteristic of RC 1). At the same time, the sensible reactor mass should be kept to the minimum required to obtain a low absolute mass ratio (characteristic of RC2). When these two characteristics are facilitated, sensible heat losses are reduced to a minimum (grey-shaded area as the target range) and the maximum average cooling power is obtained.

1.4 Literature review

As the open MHCS is driven by unused potential in hydrogen storage tanks, in this section, first a summary of hydrogen storage technologies for mobile applications is provided. Then, the compression work that is required to compress hydrogen to a final pressure of 700 bar and the maximum useful work that can be extracted from the high-pressure tank are illustrated. The section concludes with a brief overview of MH applications and the state of the art in MHCSs is presented with regard to the aim of the present thesis.

1.4.1 Hydrogen storage for mobile applications

Hydrogen has the highest lower heating value (gravimetric calorific value) of $H_{\mathrm{H2}} = 120\ \mathrm{MJ\ kg^{-1}}$ [10]. However, its low volumetric calorific value of 0.01 MJ dm^{-3} under standard conditions poses a technical challenge for the mobile storage of hydrogen [10]. This challenge includes storing the amount required for a vehicle range of around 500 km (5 –6 kg of hydrogen have to be stored onboard [77]) within the constraints of weight, volume, durability, efficiency and total cost. The ultimate targets of the United States Department of Energy (DOE) include a fast filling time within 2–3 min and gravimetric and volumetric storage capacities of 0.075 kg_{H2} per kg system and of 0.07 kg_{H2} per dm^3 system, respectively [78]. Figure 1-8 gives an overview of various hydrogen storage technologies, which can be categorized into

physical-based and material-based technologies [77,79]. The latter technologies include hydrogen storage in sorbents, MH and chemical hydrides. Physical-based storage includes compressed storage as well as storage in liquid and cryo-compressed form.

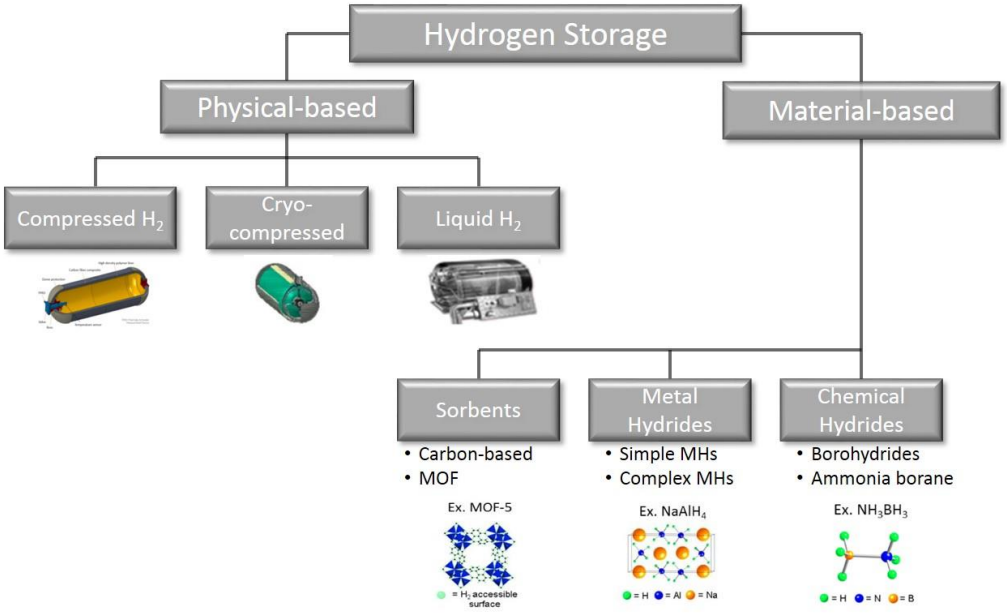

Figure 1-8: Overview and classification of hydrogen storage technologies based on [77,79].

Numerous reviews of hydrogen storage technologies have been published. For instance, Rivard et al. [80] provided a detailed overview of hydrogen storage systems for mobile applications, which includes the requirements for onboard storage along with the advantages and disadvantages of each technique. Weidenthaler and Felderhoff [25] published a review focusing on material-based hydrogen storage especially in solids. It is concluded that none of the existing material-based storage systems are suitable for automotive applications as either the current storage capacities are too low or the materials cannot be reversibly operated under acceptable physical conditions.

As a physical-based storage technique, liquid hydrogen enables an increase of the volumetric calorific value. However, a main problem is the heat input (e.g. from the surroundings) into the storage tanks, which leads to evaporation and loss of energy due to the boil-off of hydrogen. Additionally, about 30–35% of the lower heating value of hydrogen is required to liquefy it (boiling temperature of 20.3 K at standard pressure) [77]. Also, cryo-compressed storage is under consideration, where hydrogen is stored in a pressure tank at around 350 bar and up to cryogenic temperatures [25]. However, this technique requires a complex tank design and a separate infrastructure is needed.

Compressed storage of hydrogen in high-pressure tanks is the established method for mobile applications [25,80]. All commercially available FC vehicles, such as the latest Toyota Mirai [81], rely on pressure tanks with a maximum pressure of 700 bar. Furthermore, politics and industry

have decided to develop equipment standards and to establish a standardized hydrogen infrastructure (e.g. the H2Mobility initiative in Germany [82]), which is based on 700 bar refuelling stations and the compressed storage technique [6]. The state-of-the-art high-pressure tanks of types III and IV are made of a plastic or metallic liner wrapped with carbon fibres and embedded in a polymer matrix [83]. Except for the volumetric storage density, these pressure tanks fulfill the above mentioned requirements of the DOE for onboard hydrogen storage [25]. A remaining task is to further decrease its weight while guaranteeing pressure-resistance and safety in case of collision. However, it is inevitable that a considerable amount of energy is required for the compression.

1.4.2 Compression work and exergy of high-pressure tanks

The present open MHCS is driven by the onboard available but as-yet-unexploited potential energy of compressed hydrogen, which is available in state-of-the-art high-pressure tanks. In this section, the required work of compression (technical work for gas compression) and the maximum useful work (exergy) that can be extracted from these pressure tanks are presented.

Work of compression

Several studies describe the fundamentals and the work required to compress hydrogen [10,11,84,85]. The theoretical minimum work is the work of isothermal compression, where the gas temperature remains constant. With the simplification of hydrogen as an ideal gas and without considering friction, integration of the infinitesimal pressure-volume work $w = \int_1^2 v\, dp$ yields [11]:

$$w_{\mathrm{ic,IG}} = p_1 v_1 \ln\left(\frac{p_2}{p_1}\right) \tag{1-16}$$

In this equation, v_1 corresponds to the specific volume, and p_1 and p_2 are the initial pressure before hydrogen is compressed and the final gas pressure, respectively. However, in a real process, the compression is never entirely isothermal. When all the heat generated during compression is kept in the gas by ideal insulation, the theoretical maximum work by adiabatic compression for an ideal gas is described by [85]:

$$w_{\mathrm{ac,IG}} = \left(\frac{\psi}{\psi - 1}\right) p_1 v_1 \left[\left(\frac{p_2}{p_1}\right)^{\frac{\psi-1}{\psi}} - 1\right] \tag{1-17}$$

For hydrogen, the ratio of specific heats is given as $\psi = 1.41$. Figure 1-9 illustrates the work required to compress hydrogen from standard pressure to the final pressure p_2 . On the left ordinate, the ratio of compression work to the lower heating value of hydrogen (LHV) H_{H2} is shown, while the right ordinate depicts the work of compression per kg_{H2}. Thereby, the equations (1-16)–(1-18) are referred to the mass of hydrogen. According to this, the

compression to 700 bar requires a minimum of 6.8% of the LHV when the process is an ideal isothermal one and 20.2% of the LHV in the case of ideal adiabatic compression. For hydrogen pressures above 100 bar, the dimensionless compressibility factor Z is conveniently used to consider real gas behaviour. The corresponding equations for the isothermal compression of a real gas are given in the Appendix A. However, as can be seen in Figure 1-9, the deviation from ideal gas behaviour in the considered pressure range up to 1000 bar is comparably small (e.g. the deviation at 700 bar corresponds to 6.7%).

As different types of hydrogen compressors[1] and varying refuelling conditions are used (pre-cooling and overpressures are required due to compression heating), no common value for the work of compression is given in the literature. For instance, Bossel et al. [86] and Weindorf et al. [87] estimate the work of compression as 18% and 13% of the LHV, respectively, for a final hydrogen pressure of 800 bar. Literature values for the work required to compress hydrogen are included in Figure 1-9 as black dots and the grey area shows the range of expected practical values. Of these values, it can be concluded that approximately 15% of the LHV (corresponding to 18 MJ kg_{H2}^{-1}) is required to compress hydrogen from standard pressure to a final pressure of 700 bar. Since hydrogen is currently throttled down to the FC backpressure, this compression work, which is available as potential energy of compressed hydrogen in the storage tank, has been wasted until now. The maximum useful work that can be extracted from the hydrogen pressure tank can be determined using an exergy balance as described in the following.

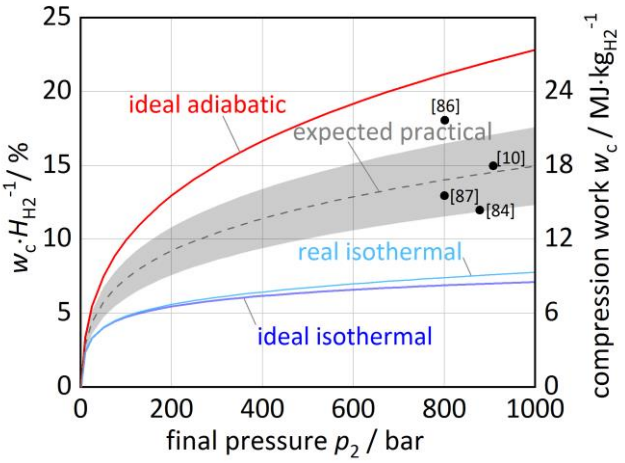

Figure 1-9: Work required to compress hydrogen from standard pressure to the final pressure p_2 based on [10,11,84,86,87]. Left ordinate: Ratio of compression work w_c to the lower heating value of hydrogen H_{H2}. Right ordinate: Work of compression per kg_{H2}.

[1] Currently, hydrogen compression is mainly conducted using multi-stage piston compressors and, related to isothermal compression, an energy efficiency of 50% is typically obtained [10,84]. In newer concepts, an MH or an electrochemical compressor is suggested [94,152].

Exergy of the pressure tank

By combining the energy and entropy balance for a closed system, the maximum useful work w_{ex} that can be extracted from the hydrogen pressure tank for a reversible change of states is given by [85]:

$$-w_{\mathrm{ex}} = u_{\mathrm{cd}} - u_{\mathrm{amb}} - T_{\mathrm{amb}}(s_{\mathrm{cd}} - s_{\mathrm{amb}}) + p_{\mathrm{amb}}(v_{\mathrm{cd}} - v_{\mathrm{amb}}) \qquad (1\text{-}18)$$

In this equation, kinetic and potential energies are neglected and $\Delta u = u_{\mathrm{cd}} - u_{\mathrm{amb}}$ corresponds to the change of internal energy. The indices “cd” and “amb” refer to the initial state of compressed hydrogen and the ambient environment, respectively. The transferred heat is given by $q = T_{\mathrm{amb}}\Delta s$ with $\Delta s = s_{\mathrm{cd}} - s_{\mathrm{amb}}$ as the change of entropy. The expression $p_{\mathrm{amb}}(v_{\mathrm{cd}} - v_{\mathrm{amb}})$ considers the work that is required to overcome the atmospheric pressure, which can be neglected in the case of a rigid wall and a constant specific volume. The maximum useful work w_{ex} is not specified, which means that the system can be brought into equilibrium by a mechanical, electrical, chemical, or thermal change of state. Equation (1-18) can be solved for real gas behaviour using a *T*–*s* diagram, which includes the lines of constant pressure p, density $\rho = 1/v$ and enthalpy $h = u + pv$.

A *T*–*s* diagram of hydrogen in the temperature range of 85–330 K is shown in Appendix B. As an example, the maximum useful work corresponds to $w_{\mathrm{ex}} \approx -4.5\ \mathrm{MJ\ kg_{H2}}^{-1}$ for an initial hydrogen pressure of $p_{\mathrm{cd}} = 700\ \mathrm{bar}$ and an FC backpressure of $p_{\mathrm{amb}} = 5\ \mathrm{bar}$ (isothermal expansion with $T_{\mathrm{amb}} = 25\ °\mathrm{C}$ and $p_{\mathrm{FC}} = p_{\mathrm{amb}}$). In this thesis, an MHCS that basically transforms the potential energy of compressed hydrogen into useful cold is investigated. As the system operates between an absorption pressure of 35 bar and an FC backpressure of around 5 bar, the maximum useful work for these conditions is given as $w_{\mathrm{ex}} \approx -1.22\ \mathrm{MJ\ kg_{H2}}^{-1}$. For the 5–6 kg of hydrogen that have to be stored onboard for a vehicle range of around 500 km, this is equal to a maximum useful work of –6.1 to –7.32 MJ. These values show that it is reasonable to implement a system which uses the as-yet-unexploited potential energy in the hydrogen pressure tank of an FC vehicle. Next to high-pressure tanks, the open MHCS can be applied in all applications, where hydrogen is available above pressures of 30-40 bar (e.g. cryo-compressed storage) and it has to be throttled to a hydrogen sink (e.g. an FC). Thereby, the system generally operates as an innovative “hydrogen pressure transducer” by locally providing thermal energy.

Besides the exergy of the pressure tank, with flowing gases, the compression and expansion are generally combined with a change of temperature. For an isenthalpic process, this change of temperature can be described using the Joule-Thomson coefficient $\mu_{JT} = (dT/dp)_h$ [10]. Since the Joule-Thomson coefficient of hydrogen is negative in the relevant range of pressures (the inversion temperature of hydrogen corresponds to 202 K), the isenthalpic expansion results in an increase of gas temperature. This effect can be seen as a rise in temperature in the *T*–*s* diagram that takes place during an isenthalpic pressure decrease. However, the effect

is relatively small, as the expansion from 700 bar to 5 bar at an initial temperature of 25 °C increases the gas temperature by only around 15–20 K. Equations (1-16) and (1-17) for calculating the work of compression are also valid for the expansion. They can be derived from equation (1-18) using ideal gas behaviour for the change of internal energy and entropy, and when the work that is required to overcome the atmospheric pressure is neglected.

1.4.3 MH applications

According to the previously presented fundamentals, MHs are able to reversibly bond with or release hydrogen gas. For this exothermic or endothermic reaction, heat is required or released and the equilibrium pressure of the gas–solid reaction is depending on the MH temperature. Due to these characteristics, there exist a variety of MH applications such as hydrogen storage and thermal applications that have been reported in various literature works and patents.

The hydrogen storage in MHs enables potential high storage capacities on a material level and the loss-free storage of hydrogen at moderate pressures [25,88]. For instance, complex hydrides such as light metal aluminium hydrides (alanates) and borohydrides are very promising storage materials owing to their high hydrogen capacities of 10.4 wt.% for $LiAlH_4$ and 18.5 wt.% for $LiBH_4$, respectively [25,89]. For alanates, however, thermodynamics properties and intrinsic kinetics are the limiting factor or the hydrogen release is not reversible. Borohydrides, on the other hand, are very stable as the desorption occurs at temperatures above 300 °C and they tend to form toxic boranes. Thermodynamic tailoring or the addition of catalysts is a promising approach to adapt the equilibrium characteristics and to improve the intrinsic kinetics. However, further research is required to develop successful materials that fulfil all the requirements for the onboard hydrogen storage [25].

Besides the hydrogen storage, MHs are used in various thermal applications. For instance, thermal energy storage based on MHs is a promising way to cope with the fluctuations and inconsistency of renewable energy sources [90–92]. Several materials are available that are found to be suitable for various operating temperature and pressures. Materials such as $NaBH_4$ and KBH_4 offer thermal energy densities of 4000 to 5600 kJ kg^{-3}, which exceed the heat storage capacity densities of sensible and latent heat storage materials [93]. The dependency of the equilibrium pressure on the MH temperature is utilized in thermally driven hydrogen compressors. These systems are characterized by safe and easy operation as no moving parts are required and multistage MH compressors allow discharge pressures up to the kilobar range. As it is possible to use waste heat instead of electricity, this technology is considered as a promising alternative to conventional methods of hydrogen compression [50,94]. Furthermore, the exothermic or endothermic character of the MH reaction is utilized for (pre-)heating, cooling and heat upgrade applications [20,95]. From these thermal applications, in particular continuous operating systems, potentially suitable MHs and the requirements for

the reactor design of the present system are derived. As an MHCS for FC vehicles is investigated in this work, the following section gives an overview of the current state of the art in this specific application.

1.4.4 MH cooling systems

According to the classification of the working material, MHCS belong to the solid sorption systems that use the heat of formation to generate a cooling effect [96]. In this thesis, they are principally divided into two basic operation modes – open and closed MHCSs. As shown in Chapter 1.3.1, an open MHCS absorbs hydrogen from a high pressure hydrogen source (e.g. a gaseous pressure tank) and releases it to a hydrogen sink (e.g. an FC) at a reduced pressure, thereby providing a cooling effect. If no hydrogen infrastructure is available, the required pressure difference has to be generated by another MH. This system is referred to as a “closed” MHCS as hydrogen does not cross the system boarder [97]. A closed system can be regarded as a common MHCS and a large variety of literature is available, including works on its demonstration and optimization. In contrast to this, the open MHCS was first presented in 2011 as a result of the increased deployment of FC vehicles and the growth of the hydrogen infrastructure. However, up to now only a single study on this system is available [98]. In the following, a brief description of the working principle of a closed MHCS is described and an overview of state of the art of MHCSs is given with regard to the aim of the thesis. From this overview, the reactor requirements for the present open system are derived (previously shown in Chapter 1.2.3), as very similar criteria have to be considered as for closed MHCSs.

Working principle of the closed MHCS

The basic configuration of the closed MHCS (thermally driven) consists of two MH materials with different thermodynamic equilibrium characteristics [20]: the low-temperature MH1 (cold generating) and the high-temperature MH2 (hydrogen–supplying material), which are able to exchange hydrogen. Similarly to the open system, the closed MHCS operates in two successive HCs (see Figure 1-10). In the cooling HC, initially, MH1 is completely charged, while MH2 is in a dehydrogenated state. When both materials are connected, hydrogen flows from MH1 to MH2 as the equilibrium pressure of MH1 is higher than that of MH2. Due to the endothermic desorption of hydrogen in MH1, the desired cooling effect at the temperature level T_{c} is generated until the maximum obtainable transformed fraction is reached. In the following regeneration HC, heat at the temperature level T_{h} is supplied to MH1 (e.g. exhaust gas from a combustion engine), causing it to desorb hydrogen when its equilibrium pressure is above MH2. The released hydrogen flows back to MH2 and the hydrogen cycle is closed. In both HCs, the heat of formation has to be released to the ambient environment at the temperature level T_{amb}. In order to gain a continuous cooling effect, two alternately working MH pairs have to be used (on the left part of Figure 1-10 only a single MH pair is illustrated).

In the literature, several variations of the closed MHCS are proposed. For instance, the required pressure difference can also be generated by a mechanical or electrochemical hydrogen compressor instead of using MH2 [67,99]. To increase the cooling effect and to enhance the performance, multi-stage arrangements have been investigated [20,100]. Furthermore, several options, such as internal heat recovery and mass recovery, are suggested to reduce the impact of sensible heat losses [101–104]. However, for these approaches, an increased number of MH reactors are required (multi-stage systems) or the system operation has to be extended and further valves have to be integrated (heat and mass recovery). Since in a closed MHCS the release of hydrogen is not coupled to the FC operation, there is an increase in the maximum obtainable cooling power along with a reduction in the time to exchange the maximum amount of hydrogen. Therefore, short HC times are generally desired for a high power density of the closed MHCS [31].

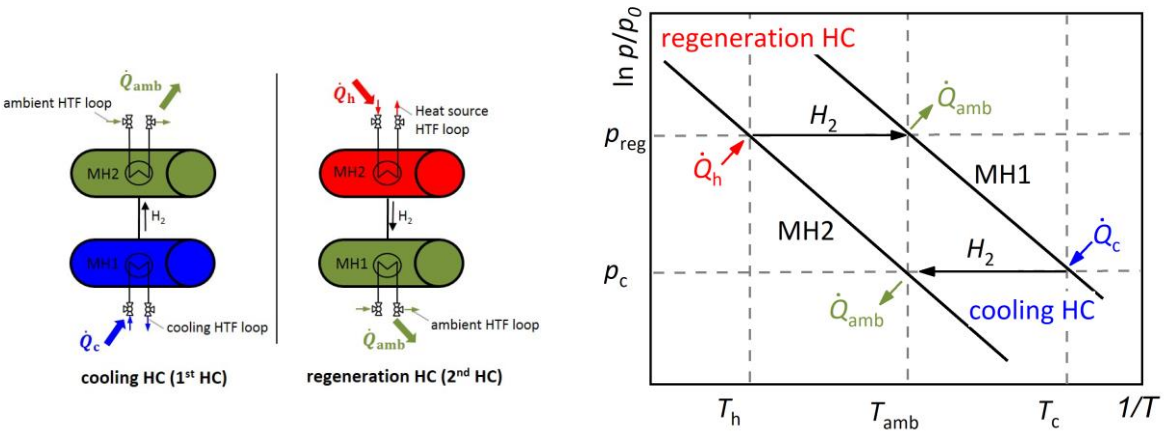

Figure 1-10: Schematic illustration (left) and van´t Hoff plot (right) of thermally driven closed MHCS.

Existing MH cooling systems

Table 1-2 gives an overview of MHCSs that have been experimentally investigated within the least 20 years, which also includes the earlier study by Ron [66]. According to their corresponding operation principles, these systems are divided into closed (thermally driven and compressor-driven) and open MHCSs. The table gives a brief description of the operating temperature levels, the applied MHs and the reactor design. To compare the performance, the specific cooling power is given per kilogram of low-temperature MH of a single reactor, as in some studies only one MH pair or a single reactor is investigated. Where not mentioned in the reference, these values have been calculated from the literature data to the best of the author´s knowledge. Nonetheless, in some cases, it is difficult to compare the performances due to the different operating conditions.

The feasibility of the thermally driven closed MHCS was first proposed by Gruen et al. in 1978 [105]. Since then, a variety of thermally driven systems have been demonstrated. Of

these, the two most promising approaches are the following: In 1984, Ron [66] developed a system that could be driven by the exhaust gas of a bus. Upon cycling operation, a specific cooling power of 200–250 W kg_{MH}^{-1} for the material pair $LaNi_{4.7}Al_{0.3}$ and $MmNi_{4.15}Fe_{0.85}$ was obtained. As the MH reactor, tubular reactors with an outside diameter of 14 mm were applied and aluminum fins in the cross-flow direction were integrated to improve the heat transfer characteristics. Using the MH pair $LmNi_{4.91}Sn_{0.15}$ and $Ti_{0.99}Zr_{0.01}V_{0.43}Fe_{0.09}Cr_{0.05}Mn_{1.5}$, Linder [31] demonstrated a specific cooling power of 640 W kg_{MH}^{-1} under operating conditions of 130 °C / 28 °C / 15 °C in 2010. The applied capillary tube bundle reactors consisted of 372 stainless steel tubes with an inner diameter of 1.4 mm, in which the shell sides were filled with the MH.

The first compressor-driven closed MHCS was experimentally investigated by Park et al. [99] in 2002. Under operating conditions of $T_{\mathrm{amb}} = 27\ °\mathrm{C}$ and $T_{\mathrm{c}} = 10\ °\mathrm{C}$, the specific cooling power was 410 W kg_{MH}^{-1}. As an MH reactor, two fin-tube reactors (outside diameter of 15 mm) filled with $Zr_{0.9}Ti_{0.1}Cr_{0.55}Fe_{1.45}$ were used and a heat-conducting matrix was included to improve the heat transfer characteristics. Magnetto et al. [106] demonstrated a cooling power of 1449 W under operating conditions of $T_{\mathrm{amb}} = 35\ °\mathrm{C}$ and $T_{\mathrm{c}} = 20\ °\mathrm{C}$ (MH mass is not given in the reference). Two ring manifold reactors with a small outer diameter of 3.175 mm were applied, with fins were added to each tube to increase the surface area.

Similarly to systems based on the vapour-compression cycle [107–109] or other sorption systems (e.g. based on silica-gel, zeolites or activated carbon [101,102,110]), all MHCSs have in common that the performance strongly depends on the operating conditions. As key influencing parameters, the operating temperature levels as well as the duration of the HC were identified. For the presented MHCS, Table 1-2 includes the range of parameters varied when a sensitivity analysis was conducted. For instance, Paya et al. [51] demonstrated that the average cooling power was decreased by more than 20% when the cooling temperature of the thermally driven MHCS was reduced from 18 to 8 °C. For a compressor-driven MHCS, Muthukumar et al. [67] showed that the average cooling power was reduced by 46 and 59% when the HC time was increased from 4 to 16 min and the cooling temperature was decreased from 20 to 10 °C, respectively. These values demonstrate that for the integration and application of an MHCS, it is very important to know the performance under varied operating conditions.

The presented specific cooling powers of these closed MHCSs are promising, however, for compact and lightweight systems in automotive applications, the performance needs to be further improved. Indeed, with regard to the intrinsic material properties of MHs, much larger values of the specific cooling power should be possible due to the high reaction rates and enthalpies of MHs [18]. The observed gap between theoretically intrinsic feasible thermal powers and experimentally proven thermal powers is mainly due to (heat transfer) limitations in the reaction bed. The reactor design for MHCS so far has been mainly restricted to tubular reactors and tube bundle reactors (cf. Table 1-2). However, there is no general rule due to the

large variety of applications and operating conditions (e.g. temperature and pressure levels, heat carrier or type of MH). At system level, furthermore, thermally driven MHCSs are currently disadvantageous with regard to the efficiency, as the coefficient of performance (COP) is below 0.5 [20]. On the other hand, compressor-driven MHCSs require progress in the development of low-capacity hydrogen compressors. Further characteristics of closed MHCSs are included in the review articles by Muthukumar and Groll [20], and Bhuiya et al. [111].

The underlying operation principle of the present open MHCS for FC vehicles was first conceptually proposed by Linder and Kulenovic [98] in 2011. The corresponding experimental setup consisted of two capillary tube bundle reactors (the same as described in [51,64]), which were each filled with 0.8 kg of the intermetallic compound $Ti_{0.99}Zr_{0.01}V_{0.43}Fe_{0.09}Cr_{0.05}Mn_{1.5}$. The regeneration HC was conducted with an absorption pressure of up to 54 bar, while at the end of the desorption the pressure was reduced to around 6 bar. However, this study focused on the MH system only since no FC was implemented in the experimental setup. Consequently, the presented values of the cooling power did not consider the dependency on the electrical power of the FC and potential limitations that might occur during the coupled operation. In contrast to the thermally or compressor-driven closed MHCS, no external heat source or electrical energy is consumed as the open MHCS is driven by the potential energy of compressed hydrogen in the pressure tank. Furthermore, it is directly implemented in the existing hydrogen infrastructure of an FC vehicle and, therefore, in terms of system complexity the open MHCS is superior compared to closed MHCSs or other sorption systems (a reduced number of components and reactors are required). To summarize these characteristics, Table **1-1** presents a comparison of the open and closed thermally driven MHCSs.

Table 1-1: Comparison of the open and closed thermally driven MHCS.

Characteristic	Open MHCS	Thermally driven closed MHCS
Driving force	Potential energy of hydrogen	Thermally driven
Temperature levels	2 (T_c and T_{amb}), 2 HTF circuits	3 (T_c, T_{amb} and T_h), 3 HTF circuits
Number of reactors	Two reactors with same MH	Four reactors with two MHs
H_2 infrastructure	H_2 pressure difference required	Independent from H_2 infrastructure
Level of development	**No system demonstration**	First prototypes in the 1970s

Conclusions of the literature review

The standardized hydrogen infrastructure for mobile applications is based on the compressed storage of hydrogen in high-pressure tanks. However, a major drawback of this storage technology is that approximately 15% of the LHV of hydrogen (corresponding to 18 MJ kg_{H2}^{-1}) is consumed for the increase of pressure up to 700 bar. At the same time, the application of electrically driven cooling systems, for instance systems based on the vapour compression cycle, result in a substantial decrease of the driving range. Open MHCSs are promising for the

utilization of the so-far unexploited potential energy of compressed hydrogen in a storage tank by generating cold and thus improving the efficiency of FC vehicles. The maximum useful work for a system that operates between an absorption pressure of 35 bar and an FC backpressure of around 5 bar corresponds to $w_{\mathrm{ex}} \approx -1.22\ \mathrm{MJ\ kg_{H2}}^{-1}$. As pointed out in the literature review of existing MHCSs, a closed system can be regarded as a common MHCS from which the requirements for the present reactor can be derived. However, at the outset of the preparation of this thesis, no detailed investigation and experimental system demonstration of an open MHCS has been conducted so far.

Table 1-2: Overview of MH cooling systems.

Author and Ref.	Year	System	Metal hydride	Reactor design	Temperature levels T_h / T_{amb} / T_c	Spec. cooling power	Varied parameters
Ron [66]	1984	Thermally driven closed MHCS	$LaNi_{4.7}Al_{0.3}$ +18 wt.% Al / $MmNi_{4.15}Fe_{0.85}$ +18 wt.% Al (Pellets)	Tubular reactor with fins	380-400 °C / 19 °C / 19 °C	250 W kg_{MH}^{-1}	-
Chernikov et al. [112]	2002	Thermally driven closed MHCS	$LaNi_{4.6}Al_{0.4}$ (1.5 kg) / $MmNi_{4.15}Fe_{0.85}$ (1.5 kg)	Tubular reactor with Al foil	200 °C / 21 °C / 10 °C	103 W kg_{MH}^{-1}	-
Park et al. [99]	2002	Compressor-driven closed MHCS	$Zr_{0.9}Ti_{0.1}Cr_{0.55}Fe_{1.45}$ (3.5 kg)	Tubular reactor with Al matrices	27 °C / 12 °C	410 W kg_{MH}^{-1}	t_{HC}: 2 – 16 min
Magnetto et al. [106]	2006	Compressor-driven closed MHCS	Rare-earth intermetallic compound (not described in detail)	Ring manifold reactor	35 °C / 20 °C	1449 W (No MH mass given)	T_{amb}: 21 – 35 °C t_{HC}: 90 – 210 s
Ni and Liu [113]/ Qin et al. [114]	2007	Thermally driven closed MHCS	$LaNi_{4.61}Mn_{0.26}Al_{0.13}$ (2.75 kg) / $La_{0.6}Y_{0.4}Ni_{4.8}Mn_{0.2}$ (2.75 kg)	Tubular reactor with fins	150 °C / 30-32 °C / 20 °C	89 W kg_{MH}^{-1}	-
Satheesh and Muthukumar [104]	2010	Thermally driven closed MHCS (double-stage)	$LaNi_{4.1}Al_{0.52}Mn_{0.38}$ (1.96 kg) / $LmNi_{4.91}Sn_{0.15}$ (1.85 kg) / $Ti_{0.99}Zr_{0.01}V_{0.43}Fe_{0.09}Cr_{0.05}Mn_{1.5}$ (1.8 kg)	Tubular reactor with Al foam	305 °C /100 °C / 25 °C / 10 °C	150 W kg_{MH}^{-1}	T_h: 285 – 325 °C T_c: 0 – 20 °C t_{HC}: 10 – 20 min
Linder [31]/ Payá et al. [51]	2010/ 2011	Thermally driven closed MHCS	$LmNi_{4.91}Sn_{0.15}$ (0.948 kg) / $Ti_{0.99}Zr_{0.01}V_{0.43}Fe_{0.09}Cr_{0.05}Mn_{1.5}$ (0.8 kg)	Tube bundle reactor	130 °C / 28 °C / 15 °C	640 W kg_{MH}^{-1}	T_h: 110 – 160 °C T_c: 3 – 18 °C t_{HC}: 50 – 400 s
Linder et al. [98]	2011	Open MHCS	$Ti_{0.99}Zr_{0.01}V_{0.43}Fe_{0.09}Cr_{0.05}Mn_{1.5}$ (0.8 kg)	Tube bundle reactor	30 °C / 13 °C	No system demonstration	T_{amb}: 30 – 35 °C
Yasuda et al. [115]	2013	Thermally driven closed MHCS	$TiFe_{0.9}Ni_{0.1}$ (0.075 kg) / $La_{0.6}Y_{0.4}Ni_{4.9}$ (0.05 kg)	Tubular reactor without HTF	125 °C / 15 °C / 15 °C	195 W kg_{MH}^{-1}	-
Fang et al. [116]	2015	Thermally driven closed MHCS	$TiMn_2$ catalyzed MgH_2 + 5 wt.% ENG (0.05 kg) / $TiV_{0.62}Mn_{1.5}$ (0.19 kg)	Tubular reactor without HTF	Not given	~125 W peak	-
Muthukumar et al. [67]	2016	Compressor-driven closed MHCS	$Lm_{4.91}Sn_{0.15}$ (2.75 kg)	Tube bundle reactor	25 °C / 20 °C	53.5 W kg_{sys}^{-1} (both reactors and total MH mass)	T_{amb}: 24 – 35 °C T_c: 10 – 20 °C t_{HC}: 4 – 16 min

1.5 Aim of Thesis

The aim of the present thesis is to perform the first systematic investigation and experimental demonstration of an open MHCS for an automotive application driven by the as-yet-unexploited potential energy of hydrogen in a high-pressure tank. For this purpose, the thesis is divided into four parts, which can be described as follows:

In the first part, the experimental details have to be defined, which includes the selection and thermodynamic characterization of a suitable MH, and the realization of an appropriate reactor concept with regard to the defined reactor requirements. For the system demonstration, an experiment setup has to be build that contains two alternately operating reactors supplied by pressurized hydrogen and directly coupled with an FC.

In the second part, with this setup, a first functional demonstration of the open MHCS has to be executed. The focus is on the investigation of whether the alternately operating reactors are able to supply the required hydrogen mass flow rate for a continuous operation of the FC without disturbing its functionality. If this is the case, what cooling power can be obtained under reference conditions and to what extent the potential energy of hydrogen can be transformed into a useful cooling effect.

As it is expected that the cooling power is strongly affected by the operating conditions, in the third part, a detailed performance investigation of the effects of varying the key influencing parameters (operating temperature levels and electrical FC power) has to be conducted. In particular, what cooling power can be realized under varied automotive conditions and to what extent the alternating operation reduces the efficiency of the system has to be demonstrated. By means of this systematic variation, it is possible to determine the operational limits of the present first-of-its-kind system.

Finally, since the achievable power of the open MHCS depends mainly on the reaction bed, the realized reactor concept has to be numerically investigated with a view to identifying performance-limiting characteristics and showing the possibilities for optimization. For this purpose, the developed model has to be validated with the experimental results and the expected performance of the improved design has to be presented in order to demonstrate the automotive applicability of the open MHCS.

2. Experimental details

For the systematic investigation of the open MHCS conducted in this thesis, the applied MH material and the realized reactor design are crucial as they define the operating temperature levels as well as the resulting cooling power of the system. Therefore, in the following section, initially, the selected MH including its thermodynamic characterization and the realized reactors are presented. Then, the experimental setup, which is applied for the first experimental demonstration of the open MHCS is described in detail. Concluding the chapter, the working principle of a novel operation optimization is introduced, which aims to reduce the thermal losses that occur in the continuous system operation. The contents of this section have been published in [117,118].

2.1 Description of the applied MH

As MH in the present study, the AB_2-alloy Hydralloy® C2 ($Ti_{0.98}Zr_{0.02}$ $Mn_{1.46}V_{0.41}Cr_{0.05}Fe_{0.08}$) was selected since it meets the requirements of the open MHCS with regard to thermodynamic equilibrium characteristics, intrinsic material kinetics and cycling stability. The material was provided by GfE (Gesellschaft für Elektrometallurgie mbH), Germany and the corresponding alloy composition is given in Table 2-1.

Table 2-1: Alloy composition of Hydralloy® C2.

	Titanium (Ti)	Zirconium (Zr)	Manganese (Mn)	Vanadium (V)	Chromium (Cr)	Iron (Fe)
Share in wt.%	29.9	1.16	51.1	13.3	1.65	2.85

A high cycling stability of the applied MH is requested since the duration of a half-cycle in the present system is in the range of 2–3 min. Wanner et al. [119] have proven the cycling stability of Hydralloy® C2 as the capacity losses are below 10% for about 10^5 absorption/desorption cycles. This value corresponds to more than 3300 hours of system operation. With respect to the short half-cycle times, additionally, the intrinsic kinetics of the applied MH have to be very fast. Skripnyuk and Ron [37] investigated the reaction constant of Hydralloy® C2, which is, for instance, 0.67 s^{-1} at 20 °C. For the desorption into vacuum, a complete transformed fraction can be obtained after around 10 s, when heat and mass transfer limitations are avoided. Furthermore, the thermodynamic equilibrium characteristics are very important to know as the relation between the equilibrium pressure p_{eq}, the hydrogen capacity ω and the MH temperature T_{eq} determines the operating conditions and the theoretically usable hydrogen capacity $\Delta\omega_{\mathrm{max}}$. In view of an automotive application, the equilibrium temperature of the applied MH at the FC backpressure p_{FC} has to be clearly below the ambient temperature. The required cooling temperature is generally determined by the space to be cooled and the final

application of the system. For instance, according to Musat and Helerea [120], the comfort level of the cabin is achieved by ensuring a temperature within the range of 20 to 22 °C. Furthermore, since the ambient environment is used as heat sink in the regeneration HC, the equilibrium temperature at the absorption pressure p_{abs} has to be above the ambient temperature. As a 700 bar hydrogen pressure tank is considered empty at around 30-40 bar, the required absorption pressure has to be in this range in order to guarantee that the open MHCS can be operated as long as the pressure in the hydrogen storage tank is above p_{abs}.

However, for Hydralloy® C2 very limited literature data about the equilibrium characteristics are available (at 5 °C, 20 °C and 30 °C). Additionally, the reported values of the reaction enthalpy differ by around 15% [37,121]. Therefore, based on a description of the measurement principle, in the following the experimental results for the thermodynamic characterization of Hydralloy® C2 are presented and a mathematical expression to describe the PCIs is presented.

2.1.1 Experimental setup for the thermodynamic characterization

The thermodynamic characterization of Hydralloy® C2 was conducted in a dynamic measurement setup. Its operating principle is based on a constant supply of hydrogen from a reference volume to an MH sample (kept at constant temperature), which increases its hydrogen uptake and pressure during the absorption. Thus, a specific PCI curve at isothermal conditions is obtained. The reverse direction is used for the corresponding PCIs of desorption.

Figure 2-1 shows the schematic flow diagram of the test bench that was used for this purpose. In principle, the test bench can be roughly divided into a Sieverts area (left) and a reactor section (right). The Sieverts area consists of three different Sieverts volumes SV1-SV3, which can be combined depending on the mass of the MH sample. To enable a constant hydrogen gas temperature, these volumes are placed in a water reservoir. The desired initial pressure for the absorption is adjusted by the hydrogen inlet and remaining gas before the desorption can be released to the ambient environment via the hydrogen outlet or the vacuum pump. An overpressure valve OVP is included to release hydrogen in case of exceedingly high pressure.

In the reactor section, a controlled supply or release of hydrogen to or from the MH reactor is enabled by the mass flow controller MFC. The corresponding hydrogen mass flow $\dot{m}_{\mathrm{H2,MFC}}$ is adjusted in such a way that a quasi-isothermal MH temperature is guaranteed during the measurement. Since the flow direction of the MFC is only one way, additional piping is required to reverse the flow for the desorption. The flow directions and the combination of the Sieverts volumes are enabled by several pneumatic valves $V_{1\text{-}15}$. As an MH reactor (see Figure 2-2, right), a stainless steel tubular reactor with an outer diameter of 9 mm and a length of 120 mm was applied. Owing to the small mass flow rates, this reactor geometry enables a quasi-isothermal MH temperature. Additionally, in the free reactor volume enough space for packing the sample is provided. The temperature in the MH was controlled by a thermocouple type K, which was located at the center and around 10 mm above the bottom end of the reactor. In

order to avoid MH powder extraction, a filter with a pore size of 3 µm was included at the hydrogen inlet of the reactor. The void reactor volume was filled with an MH mass of $m_{C2} = 16.18\,\mathrm{g}$, which was previously cycled 20 times. A picture of Hydralloy® C2 in the as-received condition and after 20 cycles is shown on the left part of Figure 2-2. To protect the MH from oxygen atmosphere after the filling procedure, a hand valve HV was included at the top of the reactor. A thermostatic bath is used to adjust and control the desired MH temperature during the PCI measurements.

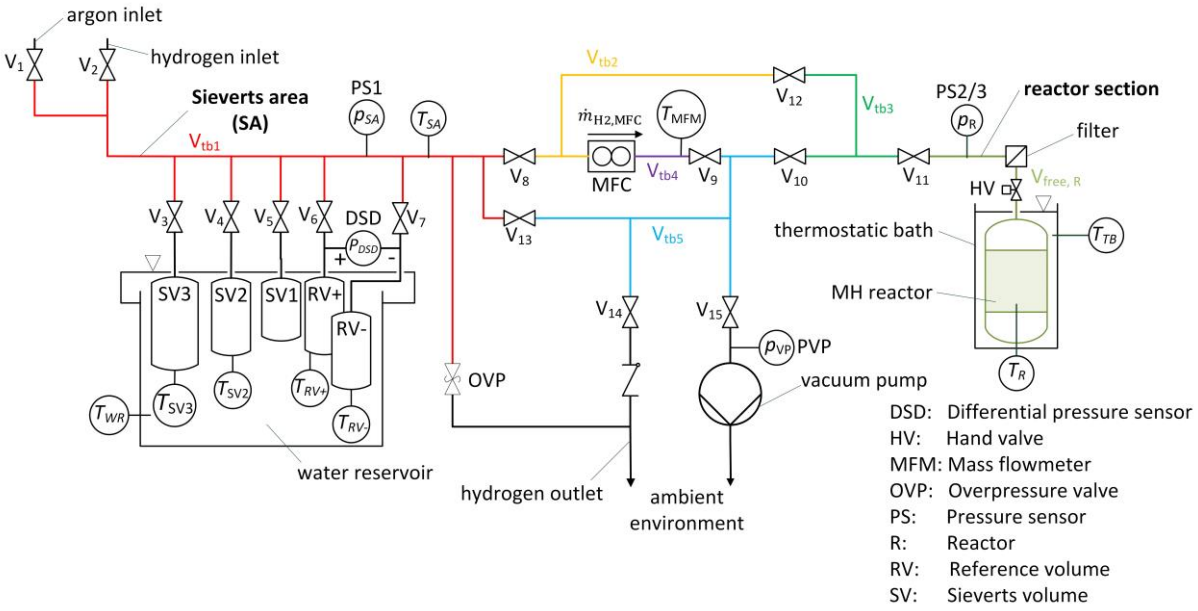

Figure 2-1: Schematic flow diagram of the experimental setup for the thermodynamic characterization of Hydralloy® C2.

In order to monitor the test bench, the following measurement equipment is additionally integrated. The pressure sensor PS1 controls the hydrogen pressure in the Sieverts area, which was leak tested up to a maximum pressure of 75 bar. Using the corresponding reference volume RV^+ or RV^-, the differential pressure sensor DSD measures the pressure change during the hydrogen absorption and desorption. The hydrogen equilibrium pressure of the MH sample is detected by the pressure sensors PS2 and PS3 depending on the pressure value in the reactor section. Furthermore, several thermocouples of type K are installed in the Sieverts volumes, the water reservoir and the connecting tubes to monitor the hydrogen gas temperature. The applied sensors including the measurement range and accuracy are summarized in Table D-2 in the Appendix.

The measurement procedure to determine the PCIs can be described as follows. Before the start of the absorption, the sample is evacuated by means of the vacuum pump and the desired MH temperature is adjusted via the thermostatic bath until constant temperature conditions are reached. The test bench is designed to operate automatically and a Siemens SIMATIC STEP 7 system is applied as a data logger. As input parameter, the hydrogen mass flow

rate, the starting and end pressure level as well as the measurement duration are adjusted. During the absorption, a constant hydrogen mass flow rate is supplied to the MH sample, which is kept on a constant temperature. Both, the hydrogen pressure and capacity slowly increase until the end of the reaction time or the end pressure level is reached. According to equation (1-2), the hydrogen capacity ω as a function of p_{eq} is given by the ratio of absorbed hydrogen mass m_{H2} to the MH mass m_{MH} (in this case, the sum of m_{MH} and m_{H2} is used). Thereby, the value of m_{H2} is derived from the pressure change in the Sieverts volume over time, which is determined by means of the differential pressure sensor DSD. The integral value of the mass flow controller MFC enables to validate the absorbed hydrogen mass. However, due to the lower accuracy of the MFC, the pressure change in the Sieverts volume is applied for the calculation of m_{H2}.

For the desorption, the Sieverts area is initially evacuated (valve V_{11} is closed) and hydrogen is released from the MH sample at the adjusted flow rate until the end of the desorption is reached. The remaining mass of hydrogen in the MH sample is given by the initial hydrogen mass at the end of the absorption reduced by the released amount of hydrogen. The change of hydrogen mass in the free volume of the reactor section is taken into account as difference between initial hydrogen mass at the end of the absorption and the remaining hydrogen mass in the free volume. In order to obtain accurate measurement values, all free volumes of the test bench are precisely determined. For this purpose, an argon supply is included at the inlet of the Sieverts area. Further details for the thermodynamic characterization including the calculation of the hydrogen mass are given in the Appendix D and the references [97,122].

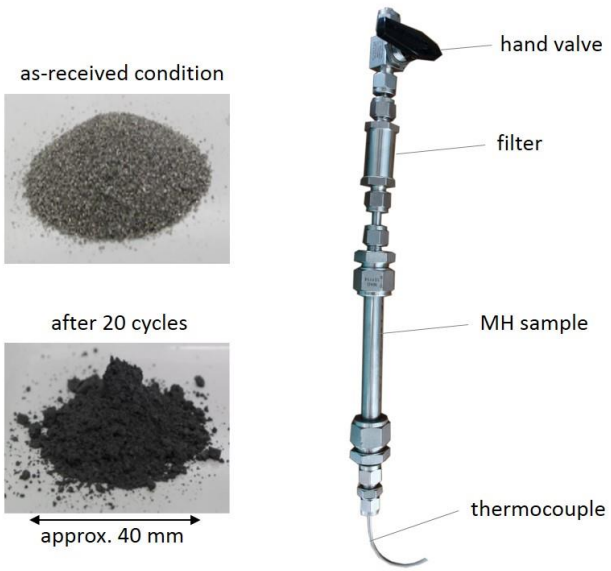

Figure 2-2: Picture of Hydralloy® C2 in the as-received condition and after 20 cycles (left), and design of the reactor for the thermodynamic characterization (right).

2.1.2 Results of the thermodynamic characterization

Figure 2-3 presents the PCIs of Hydralloy® C2 for the absorption (left) and desorption (right) in the relevant temperature range from 0–50 °C. The measurements for a single PCI were performed with a hydrogen mass flow rate of $\dot{m}_{\mathrm{H2}} = 6.75 \cdot 10^{-4}\ \mathrm{g\ min^{-1}}$ and in the Sieverts area with a volume of 1.8 dm^3 (volumes S2 and S3 were used) a pressure change of around 3 bar for an experimental duration of around 11 h was observed. During these measurements, the maximal temperature change of the MH sample was 2 K. From the experimental PCIs (dashed lines with symbols), it can be seen that the material shows a plateau for around $0.6\ \mathrm{wt.\,\%} < \omega < 1.6\ \mathrm{wt.\,\%}$ and a maximum hydrogen capacity of $\omega_{\max} = 1.75\ \mathrm{wt.\,\%}$. In the plateau region, a slope and a hysteresis can be observed. For instance, at 20 °C the difference between absorption and desorption pressure is around 2.5 bar, which results in a hysteresis factor of $f_{\mathrm{hys}} = 0.19$ (see equation (1-4)). The corresponding plateau factors at 20 °C are $m_{\mathrm{pl,abs}} = 5.7\ \mathrm{wt.\,\%^{-1}}$ and $m_{\mathrm{pl,des}} = 4.1\ \mathrm{wt.\,\%^{-1}}$ for $\Delta\omega = 0.1\ \mathrm{wt.\,\%}$ at the middle of the plateau (see equation (1-3)).

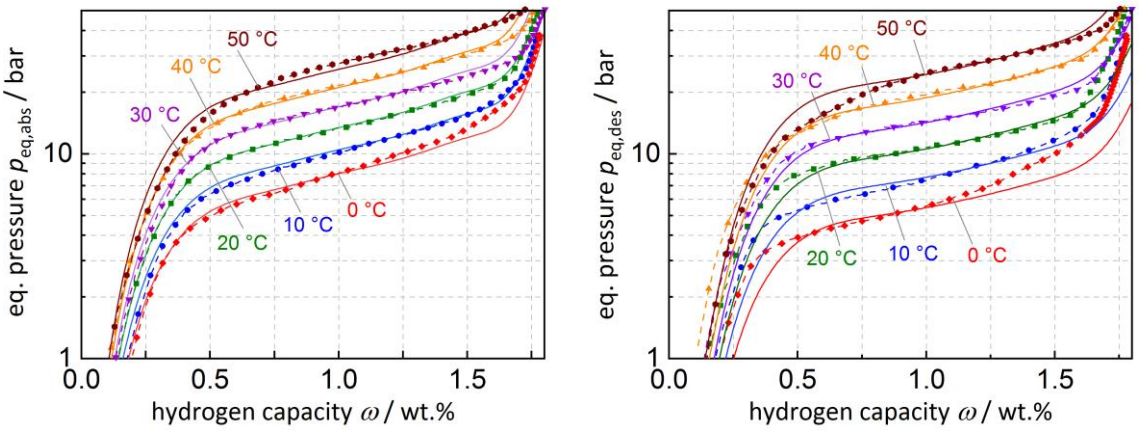

Figure 2-3: PCI of Hydralloy® C2 for the absorption (left) and desorption (right): Experiments (dashed lines with symbols) and polynomial fit according to equation (2-4) (solid lines).

In Figure 2-4 the van 't Hoff plot of Hydralloy® C2 is shown, which is derived from the experimentally determined PCIs (measurement points are given as symbols). The solid red lines describe the equilibrium of the absorption of hydrogen, while the dashed blue lines correspond to the desorption. According to this data, it is clear why this material has been chosen for this work: During the desorption of hydrogen a cooling effect can be generated, since for an FC backpressure of around 5 bar, the equilibrium temperature at a hydrogen capacity of $0.5\omega_{\max}$ is equal to 0 °C. This temperature fits to the comfort level of the cabin, since for the heat transfer from the cabin to the MH a temperature gradient is required. In the regeneration HC, a hydrogen pressure of around 30–35 bar is needed to charge the MH at an ambient temperature above 40 °C. Thus, with regard to these temperature and pressure conditions, the material is suitable for an automotive application.

From the van´t Hoff law according to equation (1-5) and the corresponding equilibrium pressure p_{eq}, the reaction enthalpy and entropy can be determined. In the table on the right part of Figure 2-4, the derived values for the absorption and desorption are given, which are mean values in the presented temperature range from 0–50 °C for $0.5\omega_{\mathrm{max}}$. These material properties are important as the maximum obtainable cooling power $\dot{Q}_{\mathrm{max,des}}$ depends directly on the desorption reaction enthalpy ΔH_{des} of the applied material (see Chapter 1.3.2).

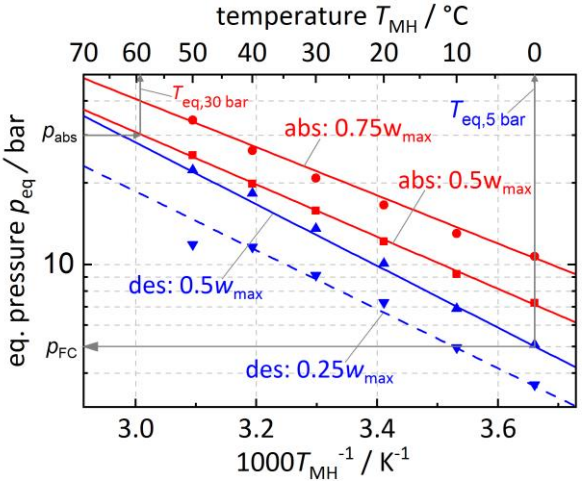

Material properties of Hydralloy® C2.	
Parameter	**Value**
ΔH_{abs}	17.8 kJ mol^{-1}
ΔH_{des}	21.9 kJ mol^{-1}
ΔS_{abs}	83.9 J mol^{-1} K^{-1}
ΔS_{des}	91.8 J mol^{-1} K^{-1}
ω_{max}	1.75 wt. %

Figure 2-4: Van´t Hoff plot for various hydrogen capacities ω (left) and material properties of Hydralloy® C2 (right).

Furthermore, from the PCIs and the van´t Hoff plot the theoretically usable hydrogen capacity $\Delta\omega_{\mathrm{max}}$ can be obtained, which defines the amount of hydrogen that can be released by the MH reactors to the FC in one half-cycle. For instance, for a regeneration temperature of 30 °C at an absorption pressure of 35 bar and a cooling temperature of 20 °C at an FC backpressure of 5 bar, the maximum usable hydrogen capacity corresponds to $\Delta\omega_{\mathrm{max}} = \omega_{\mathrm{abs}} - \omega_{\mathrm{des}} = 1.32$ wt. % (this value is determined based on a polynomial fit of the PCIs presented in the following). However, as can be seen from the deviations between the lines for 25% and 75% transformed fraction in Figure 2-4, this value can vary significantly with the operating temperature and pressure levels. For instance, when the value of the FC backpressure is increased to 10 bar, and the absorption pressure and the temperature levels remain constant, the maximum usable hydrogen capacity is reduced to $\Delta\omega_{\mathrm{max}} = 0.82$ wt. %. In order to characterize to what extent the theoretically usable hydrogen capacity $\Delta\omega_{\mathrm{max}}$ is exploited in the operation of the open MHCS, the hydrogen utilization factor F can be used [123,124]. It depends on the reactor design and is defined as the ratio of actually used hydrogen capacity $\Delta\omega$ to the theoretically usable hydrogen capacity $\Delta\omega_{\mathrm{max}}$:

$$F = \frac{\Delta\omega}{\Delta\omega_{\mathrm{max}}} \tag{2-1}$$

Polynomial fit of the PCIs for Hydralloy® C2

A mathematical expression that precisely describes the PCIs is very important for the design of the open MHCS and the numerical analysis of the present reactor design, which is conducted in Chapter 5 to identify performance-limiting characteristics. Different methods have been presented in the literature for this purpose, e.g. the Zou or the Lacher–Lototsky model [125–127]. Of these methods, the polynomial fitting method [128,129] is in best accordance with the present experimental results. In this approach, the PCI of a single experimental reference isotherm (here $T_{\mathrm{ref}} = 273.15\ \mathrm{K}$) with the equilibrium pressure p_{ref} is approximated by the polynomial

$$\frac{p_{\mathrm{ref}}}{p_0} = \sum_{i=0}^{n_{\mathrm{abs/des}}} K_{\mathrm{i}} \omega^{\mathrm{i}}, \tag{2-2}$$

where k_i are the polynomial fitting coefficients and p_0 is the standard pressure. Then, for the equilibrium pressure p_{eq}, the van´t Hoff law corresponding to equation (1-5) is formulated for the desired equilibrium temperature T_{eq} and the reference isotherme T_{ref}, resulting in the following equation:

$$\frac{p_{\mathrm{eq}}}{p_{\mathrm{ref}}} = \exp\left\{\frac{\Delta H_{\mathrm{abs/des}}}{R} \cdot \left(\frac{1}{T_{\mathrm{ref}}} - \frac{1}{T}\right)\right\} \tag{2-3}$$

Consequently, the equilibrium pressure for absorption $p_{\mathrm{eq,abs}}$ or desorption $p_{\mathrm{eq,des}}$ at a given equilibrium temperature T_{eq} is

$$\frac{p_{\mathrm{eq,abs/des}}}{p_0} = \exp\left\{\frac{\Delta H_{\mathrm{abs/des}}}{R} \cdot \left(\frac{1}{T_{\mathrm{ref}}} - \frac{1}{T}\right)\right\} \sum_{i=0}^{N_{\mathrm{abs/des}}} K_i \omega^i \tag{2-4}$$

The fitting parameters K_i for the equations of absorption ($N_{\mathrm{abs}} = 11$) and desorption ($N_{\mathrm{des}} = 9$) are summarized in Table 2-2 and in equation (2-4) the hydrogen capacity ω is expressed in percent. Corresponding to Figure 2-3, the polynomial fits (solid line) are in good agreement with the previously presented measurements. Hence, they are appropriate for describing the PCIs of Hydralloy® C2. In the plateau region between $0.6\ \mathrm{wt.\,\%} < \omega < 1.6\ \mathrm{wt.\,\%}$, the mean value deviation for the absorption is below 5% and for the desorption is below 7%. For a desorption temperature of 0 °C and 50 °C, this deviation slightly increases in the α-phase ($\omega \leq 0.6\ \mathrm{wt.\,\%}$) and β-phase ($\omega \geq 1.6\ \mathrm{wt.\,\%}$).

Table 2-2: Parameters of the polynomial fit for Hydralloy® C2.

Parameter	Absorption	Desorption
N	11	9
K_0	-0.03	-0.227
K_1	2.52	10.12
K_2	-26.48	-132.84
K_3	430.82	879.24
K_4	-1322.4	-2495.4
K_5	1578.3	3833.4
K_6	-364.55	-3466.8
K_7	-910.82	1856
K_8	875.41	-546.39
K_9	-255.61	68.37
K_{10}	-12.27	-
K_{11}	13.14	-
T_{ref}	273.15 K	273.15 K

2.2 Description of the reactor design

The MH reactor is the most important component of the present system and several considerations have to be taken into account as mentioned in the introduction. Due to the low thermal conductivity of the MH, firstly, short heat transfer distances in the MH bed to/from the HTF have to be achieved to avoid heat transfer limitations. Secondly, in order to reduce thermal losses that occur in continuous system operation at two temperature levels, the reactor should have a low mass ratio of the passive reactor mass to the active MH mass. Furthermore, mechanical strains due to periodic swelling of the material as well as the hydrogen pressure have to be considered (see Chapter 1.2.2 and 1.3.2).

Based on these design criteria, the novel plate reactor concept is applied in the present study that was first proposed in [130]. In single measurements with a small-scale reactor (filled with 0.353 kg of Hydralloy® C5), very short reaction times of $t \sim 60$ s were demonstrated, which makes it suitable for the application in the open MHCS. An extract from this single reactor characterization is shown in the Appendix C.

In this thesis, an up-scaled version of this reactor concept is used for the two identical reactors (cf. Figure 2-5). It is based on a brazed plate heat exchanger from Kelvion Holding GmbH of type GWH 220H-36 with a single-pass system. In the primary and secondary sides of the reactor, the MH (number of channels: $N_{\mathrm{MH}} = 18$) and the HTF ($N_{\mathrm{HTF}} = 17$) are arranged alternately in very small channels with an average thickness of 1.76 mm. This results in a very short average heat transfer distance in the MH bed of 0.44 mm, which is a quarter of the average channel thickness. The MH and HTF channels are separated by 36 plates made of stainless steel 1.4401. On the HTF side, stamped plates (see cross-sectional view at the bottom

right in Figure 2-5) enable a high heat transfer coefficient α from the reactor wall to the fluid. For instance, for an HTF inlet temperature of $T_{\mathrm{HTF,in}} = 35\ °\mathrm{C}$ and an HTF flow rate of $\dot{V}_{\mathrm{HTF}} = 7\ \mathrm{l\ min^{-1}}$, α corresponds to around 1200 W m^{-2} K^{-1}. This value is given by the manufacturer for a mixture of water/glycol as an HTF. Therefore, external heat transfer limitations in the HTF are avoided.

For the uptake and release of hydrogen, the connection C3 is utilized. In this connection, a filter candle with a filtration ratio of 3 µm is integrated to exclude MH extraction and to realize a uniform distribution of hydrogen in the MH channels. The connection C4 is used for the MH filling procedure and remains closed during the operation of the system. On the HTF side, the connections C1 and C2 are used as HTF inlet and outlet.

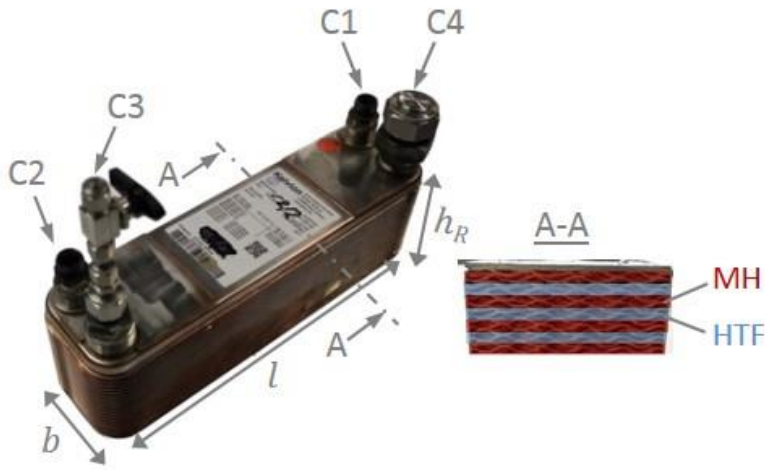

Figure 2-5: Design of the plate reactor. Right: Cross-sectional view.

The reactor is pressure resistant up to a pressure of 55 bar and the dimensions are 328 mm × 90 mm × 92 mm (length l × width b × height h_{R}), which results in a reactor volume of 2.7 dm^3. The free volume on the MH side is filled with a total MH mass of $m_{\mathrm{MH,R1}} = 1.43\ \mathrm{kg}$ and $m_{\mathrm{MH,R2}} = 1.49\ \mathrm{kg}$, and an equal distribution in each MH player was realized. To guarantee the mechanical stability of the reactor and taking into account the influence of the MH expansion, this value corresponds to a high average porosity of $\epsilon_{\mathrm{R1}} = 68\%$ and $\epsilon_{\mathrm{R2}} = 67\%$ in the MH beds. The empty reactor mass is 4.7 kg without the sealing cap at the connection C4 and the piping at C3, which is equal to a low mass ratio according to equation (1-9) of $k_{\mathrm{R1}} = 3.28$ and $k_{\mathrm{R2}} = 3.16$. Apart from the small acquisition cost and the good volume to surface ratio of the plate reactor, a major advantage of the concept is its scalability. As long as the dimensions of the plates are constant, heat and mass transfer remain unchanged, and the concept can be adapted to the desired application (e.g. electrical FC power of the present open MHCS) by increasing the number of plates and the HTF flow. In Table 2-3, all relevant characteristics of the plate reactor is summarized.

Before filling the reactors, the MH was activated and then pre-cycled 20 times in a Swagelok sample cylinder (type: 304L-HDF4-1000, pressure resistant up to 124 bar), which was temperature controlled by means of a thermostatic bath. The absorption HCs were conducted with an absorption pressure of 45 bar and a temperature of 5 °C, while the desorption HCs were executed at a temperature of 110 °C into vacuum. Due to the pre-cycling, the high mechanical stresses that occur in the first cycles are reduced, and the MH fragments in small particles with an average particle size in the range of 6 µm [131], which can be filled in the reactor. During the operation the reactor is positioned vertically and hydrogen is supplied from the bottom. Thereby, densification and segregation at the bottom of the reactor are counteracted.

Table 2-3: Characteristics of the plate reactor.

Description	Value
Average channel thickness	1.76 mm
Empty reactor mass	4.7 kg (without connections)
Free MH volume	0.712 dm^3
Heat exchange area	0.88 m^2
Mass ratio of reactor R1 and R2	$k_{\mathrm{R1}} = 3.28$ and $k_{\mathrm{R2}} = 3.16$
Max. permitted pressure	55 bar
Max. permitted temperature	200 °C
MH mass of reactor R1 and R2	$m_{\mathrm{MH,R1}} = 1.43$ kg and $m_{\mathrm{MH,R2}} = 1.49$ kg
Number of HTF channels	$N_{\mathrm{HTF}} = 17$
Number of MH channels	$N_{\mathrm{MH}} = 18$
Number of separating steel plates	$N_{\mathrm{SP}} = 36$
Reactor dimensions	328 mm × 90 mm × 92 mm ($l \times b \times h_{\mathrm{R}}$)
Reactor volume	2.7 dm^3
Porosity of reactor R1 and R2	$\epsilon_{\mathrm{R1}} = 68\%$ and $\epsilon_{\mathrm{R2}} = 67\%$
Thickness of the separating plates	0.4 mm

2.3 Description of the experimental setup

After presenting the applied MH and the realized reactor design, the experimental setup that is used for the first demonstration of the open MHCS is described in the following. According to the schematic flow diagram, which is shown in Figure 2-6, the setup can be divided into a hydrogen section (left) and an HTF infrastructure section (right).

Description of the hydrogen section

The hydrogen section on the left side consists of a hydrogen inlet section (shown in yellow) and a hydrogen outlet section (shown in blue), which connects the two plate reactors with the FC. At the inlet, hydrogen from the pressure tank (PT) is throttled down to the absorption pressure p_{abs} by means of the mechanical pressure reducing valve PRV1. Depending on the operation of the reactors, the electromagnetic three-way valves $V_{H2,1}$ and $V_{H2,2}$ distribute

hydrogen to (absorption) or from (desorption) the plate reactors. While reactor R1 supplies hydrogen to the FC in the 1st HC, reactor R2 absorbs hydrogen from the pressure tank and vice versa in the 2nd HC. Thus, according to the system´s working principle (cf. Figure 1-6), two repetitive states of operation are realized, which enable a continuous supply of hydrogen to the FC at the hydrogen outlet.

Since the maximum FC supply pressure is limited to 6.25 bar, the mechanical pressure reducing valve PRV2 reduces the outlet pressure of the reactors. Next to this, the following safety valves are additionally implemented in the setup: In order to protect the FC and the reactors from exceedingly high pressure (e.g. in case of failure of PRV1 or PRV2), the mechanical overpressure valves OPV1 and OPV2, that release hydrogen to the ambient for pressures above 40 bar and 6.25 bar, respectively, are integrated. In case of leakage, the electromagnetic hydrogen valves $V_{H2,3\text{-}5}$ enable to stop the hydrogen flow from the pressure tank to the FC. The hand valves HV1 and HV2, which are directly at the inlet of the reactor, protect the MH from oxygen atmosphere after the filling procedure or in case of leakage in the hydrogen piping.

In order to monitor the hydrogen section, the following measurement equipment is integrated. The hydrogen mass flow rates at the inlet and outlet of the system are measured by the Coriolis mass flow meter MFM1 and the mass flow meter MFM2. The two pressure sensors PS1 and PS2 measure the hydrogen pressure of reactor R1 and R2 during the absorption and desorption. Furthermore, the pressure at the FC inlet is controlled by the pressure sensor PS3, which is also utilized for the switching of the HCs. Since the reactor outlet pressure decreases during the desorption of hydrogen and the FC requires a minimum operating backpressure of 4.1 bar, the HCs are switched when the pressure at the FC inlet is below the switching pressure of $p_{\mathrm{sw}} \leq 4.3$ bar.

The FC is a HyPM™ HD8 manufactured by Hydrogenics Corporation. The low-temperature PEM FC consists of a stack with 80 cells and a total surface area of 0.02 m². The dimensions of the FC are 365 mm × 250 mm × 224 mm (length × width × height), which results in a total volume of around 20 dm³ (coolant pump and delivery excluded), and the total mass corresponds to 26 kg. The maximum electrical power that can be achieved is 8.5 kW. The corresponding voltage varies between 40 to 80 V and the maximal current is 200 A.

The required oxygen is supplied to the FC cathode by an air supply system, which consists of a fan and air ducts. The produced water vapor of the electrochemical reaction is released to the surroundings of the laboratory. To avoid overheating of the FC, a separate FC cooling circuit is installed (HTF: Glysantin FC G20-00/50). It includes a fluid-to-air heat exchanger (vehicle cooler of a Smart ForTwo ED) and a liquid-to-liquid heat exchanger in order to release the waste heat to the ambient or the cooling infrastructure of the laboratory. Several resistance thermometers and differential pressure sensors, are installed in this circuit to control the FC

operation. A picture of the FC cooling circuit and the entire experimental setup can be seen in Figure 2-7.

In order to consume and adjust the electrical power, the FC is electrically coupled to a DC electronic load. The corresponding electrical current and the voltage are measured by the ammeter AM and the voltmeter VM. The electrical FC power of the FC is calculated according to:

$$P_{\mathrm{el}} = U_{\mathrm{el}} I_{\mathrm{el}} \tag{2-5}$$

Thus, with the LHV of hydrogen H_{H2}, the FC efficiency η_{FC} can be determined according to:

$$\eta_{\mathrm{FC}} = \frac{P_{\mathrm{el}}}{H_{\mathrm{H2}} \dot{m}_{\mathrm{H2,out}}} \tag{2-6}$$

In the experiments presented in the following, the FC operates with a constant electrical power. This assumption is reasonable, since in the FC vehicle operation the peak demands for propulsion are usually covered by the electrical battery, which allows a mainly constant FC operation.

Description of HTF infrastructure section

To simulate the temperature levels T_{amb} and T_{c} corresponding to the working principle of the system, the HTF infrastructure section on the right part of Figure 2-6 consists of an ambient HTF loop (shown in red) as well as a cooling HTF loop (shown in green). Depending on the system operation, the electromagnetic valves $V_{\mathrm{HTF,1\text{-}4}}$ at the inlet and outlet of R1 and R2 connect these two HTF loops with the alternately working MH reactors.

During the 1st HC, the cooling HTF loop is connected to R1, and heat is supplied for the endothermic desorption of hydrogen. At the same time, during the absorption of hydrogen in reactor R2, the ambient HTF flows through the reactor, and the exothermic heat of formation is released. In the following 2nd HC, the positions of the HTF valves are changed, and the reactors R1 and R2 are connected to the ambient HTF and cooling HTF, respectively. To avoid that the reactors do not affect each other during the alternating operation, they are properly insulated. In order to reduce the number of HTF valves and the required system volume, in the experimental setup two 6/2-way HTF valves are used to replace the HTF valves $V_{\mathrm{HTF,1\text{-}4}}$. The thermostatic baths TB_{amb} and TB_{c} are applied as a heat sink and heat source to obtain constant inlet temperatures. The corresponding HTF flow rates can be adjusted by means of the pumps P_{amb} (directly integrated in TB_{amb}) and P_{c}. As HTF, a mixture of water and antifreeze Glysantin® G48 (ratio of 1:1) is used, which has a specific heat capacity of $c_{\mathrm{p,HTF}} = 3245\ \mathrm{J\ kg^{-1}\ K^{-1}}$ and a density of $\rho_{\mathrm{HTF}} = 1073\ \mathrm{kg\ m^{-3}}$ at 20 °C. The specific heat capacity $c_{\mathrm{p,HTF}}$ was measured with differential scanning calorimetry in the temperature range from 0–60 °C and its density ρ_{HTF} was determined using a hydrometer.

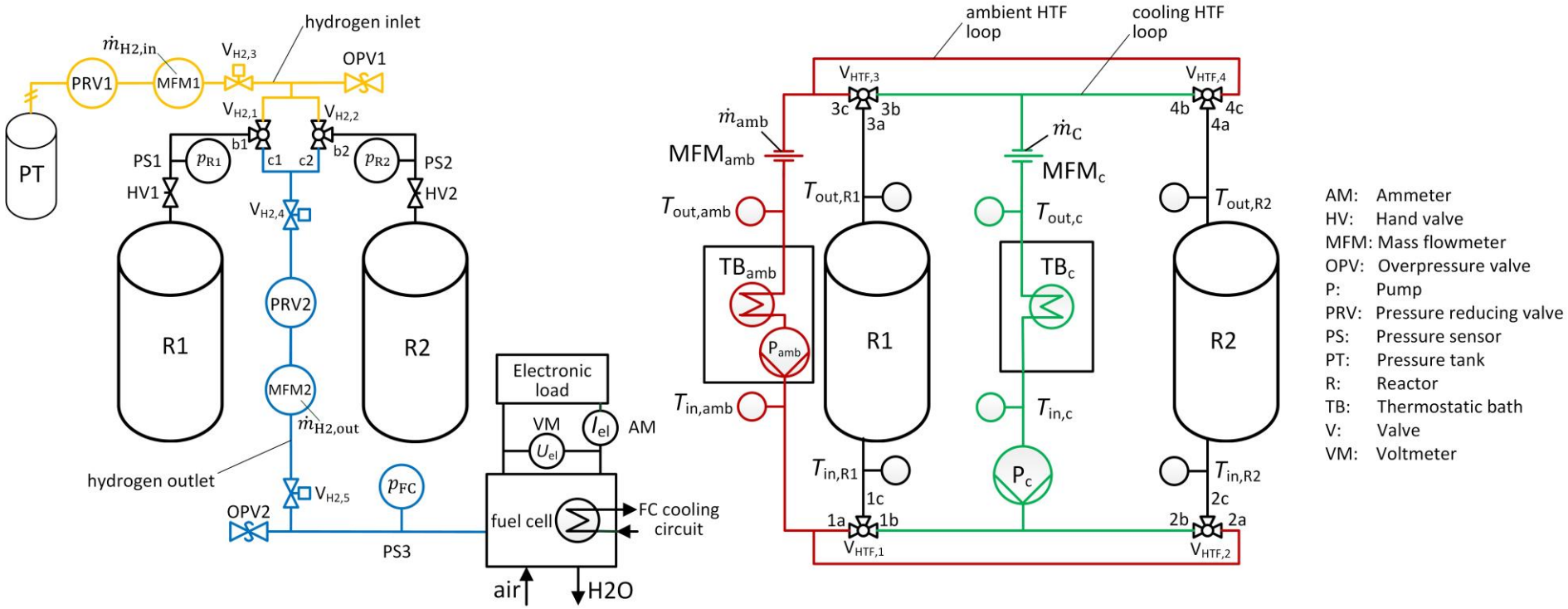

Figure 2-6: Schematic flow diagram of the experimental setup for the demonstration of the open MHCS: Hydrogen section (left) and HTF infrastructure section (right).

In order to survey the HTF temperatures and to determine the transferred thermal power, eight resistance thermometers and two impeller HTF flow meters MFM_{amb} and MFM_c are installed in the HTF infrastructure section. Two Pt 100 sensors are each integrated at the reactor inlet and outlet as well as in the ambient and cooling HTF loop. The resulting transferred cooling power in the cooling HTF loop is calculated according to:

$$\dot{Q}_{\mathrm{HTF}} = \dot{V}_{\mathrm{c}} \rho_{\mathrm{HTF}} c_{\mathrm{p,HTF}} \left(T_{\mathrm{in,c}} - T_{\mathrm{out,c}}\right) \tag{2-7}$$

According to this, positive values of the HTF power correspond to a cooling effect, while negative values show a heat input in the HTF cooling loop.

Since thermal losses occur in the continuous operation at the two temperature levels, the resulting average cooling power in the HTF $\dot{Q}_{\mathrm{HTF,avg}}$ is reduced. The cooling efficiency η_{c} with the maximum obtainable cooling power $\dot{Q}_{\mathrm{max,des}}$ according to equation (1-10) can be evaluated to characterize the efficiency of the present system:

$$\eta_{\mathrm{c}} = \frac{\dot{Q}_{\mathrm{HTF,avg}}}{\dot{Q}_{\mathrm{max,des}}} \tag{2-8}$$

The implemented measurement sensors are summarized in Table 2-4 and the equipment of the experimental setup is shown in the Appendix E. The heat input in the two 6/2-way HTF valves (from the ambient HTF loop to the cooling HTF loop) and the temperature dependency of the HTF values was considered in the evaluation of the experiments. The embedded CompactRIO® controller by National Instruments is applied as a data logger and control unit of the test bench. The FC and its cooling circuit is monitored by the onboard control and diagnostic software HyPM view, which is supplied by the manufacturer.

Table 2-4: Measurement sensors of the experimental setup for the open MHCS.

Sensor	Measurement range	Accuracy	Max. deviation
H_2-Mass flow meter MFM1	0–333 sL min^{-1}	±0.1% v.Rd	0.33 sL min^{-1}
H_2-Mass flow meter MFM2	0–200 sL min^{-1}	±0.5% Rd plus ±0.1% FS	1.2 sL min^{-1}
Absolute pressure sensors PS1-2	0–50 bar	±0.1% FS	0.05 bar
Absolute pressure sensor PS3	0–30 bar	±0.1% FS	0.03 bar
Ammeter AM	0–600 A	±0.0002% at 25 °C	0.012 A
Voltmeter VM	0-60 V	< ±0.08% v.Rd	0.048 V
Resistance thermometers	-100 °C to +450 °C	±(0.15 °C+0.002*T*)	0.23 K (<40 °C)
HTF flow meter MFM_C and MFM_R	0–16.67 L min^{-1}	±2% v.Rd	0.33 L min^{-1}

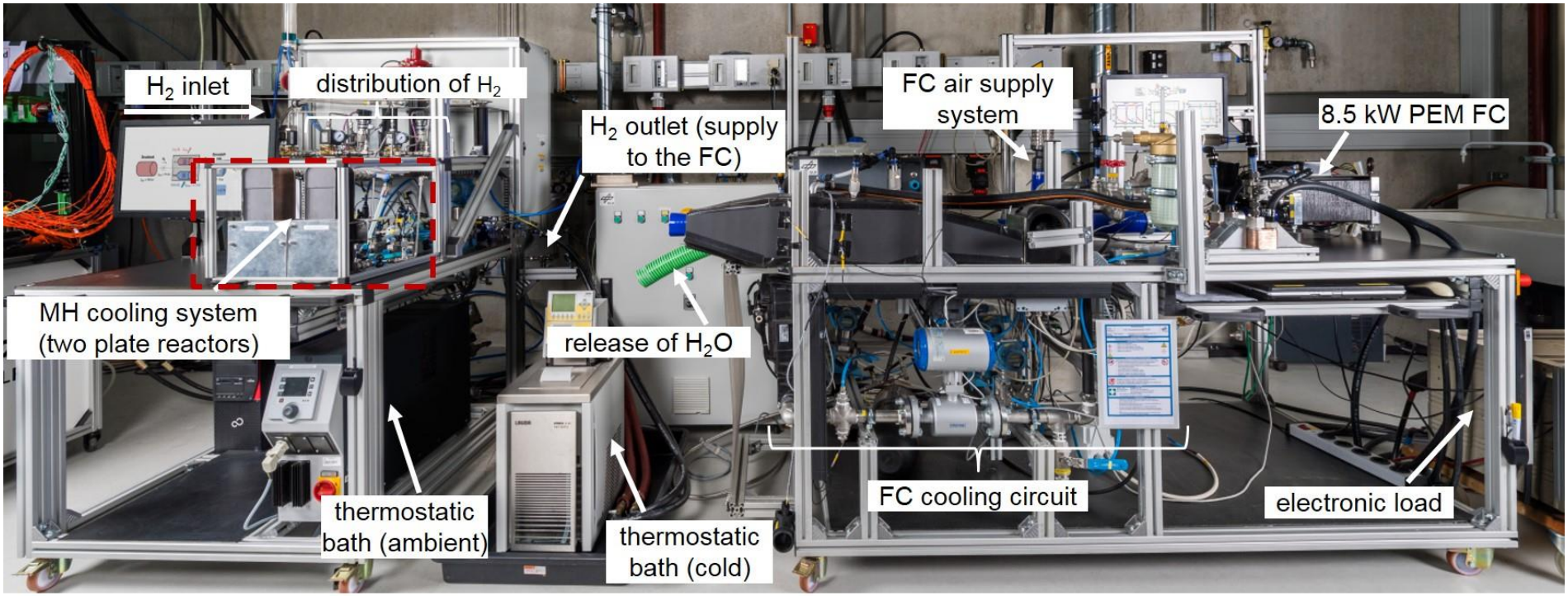

Figure 2-7: Picture of the experimental setup for the demonstration of the open MHCS.

2.4 Description of the operation optimization

The alternating operation of the reactors at two temperature levels decreases the performance of the open MHCS. In order to reduce this effect, a novel operation optimization is introduced in present thesis that can be described as follows. During the continuous system operation and the switching of the HCs, the HTF valves at the inlet and outlet of the reactor are not switched at the same time as it would have been expected for the following reason: At the beginning of each cooling HC, ambient HTF from the previous HC is present in the HTF volume of the currently desorbing reactor (volume between HTF inlet valves $V_{HTF,1\text{-}2}$ and HTF outlet valves $V_{HTF,3\text{-}4}$). When the HTF inlet valves and the HTF outlet valves would be switched at the same time, this ambient HTF flows into the cooling HTF loop. Consequently, there would be a heat input, which can significantly reduce the cooling efficiency. This effect is referred to as fluid exchange losses.

To reduce these fluid exchange losses and to increase the cooling efficiency, a novel operation optimization is implemented in the system operation that can be explained as follows. At the beginning of each HC (cf. Figure 2-8), initially, only the position of the HTF valves at the reactor inlet $V_{HTF,1\text{-}2}$ are changed. At the same time, the position of the HTF outlet valves $V_{HTF,3\text{-}4}$ remain in the position of the previous HC for the duration t_{ts}. Thus, there is a time-shifted switching of the HTF outlet valves at the beginning of each HC. The outlet of the previously absorbing reactor is initially still connected to the hot ambient loop, and therefore remaining hot HTF from the previous regeneration flows into the intended ambient HTF loop. At the same time, the remaining cold HTF from the previously desorbing reactor can flow into the cooling HTF loop.

Table 2-5: States of operation and the HTF/H_2 valve positions.

Number of HC	**1st HC**		**2nd HC**	
Operating mode	R1: Cool-HC	R2: Reg-HC	R1: Reg-HC	R2: Cool-HC
Time-shifted valve switching (beginning of each new HC)	$V_{HTF,3}$: 3a-3c	$V_{HTF,4}$: 4a-4b $V_{H2,3}$: closed	$V_{HTF,3}$: 3a-3b $V_{H2,3}$: closed	V_{HTF4}: 4a-4c
HTF-valve position	$V_{HTF,1}$: 1b-1c $V_{HTF,3}$: 3a-3b	$V_{HTF,2}$: 2a-2c $V_{HTF,4}$: 4a-4c	$V_{HTF,1}$: 1a-1c $V_{HTF,3}$: 3a-3c	$V_{HTF,2}$: 2b-2c $V_{HTF,4}$: 4a-4b
H_2-valve position	$V_{H2,1}$: b1-c1	$V_{H2,2}$: a2-b2	$V_{H2,1}$: a1-b1	$V_{H2,2}$: b2-c2

When no more hot ambient HTF is in the reactor volume (HTF from the cooling loop enters the reactor at the inlet and no mixture of ambient HTF loop and cooling HTF loop is assumed), the HTF outlet valves are switched. To avoid that the heat of formation of the absorption gets into the cooling loop, during the time-shifted valve switching the hydrogen mass flow rate at the inlet is stopped by additionally closing the hydrogen valve $V_{H2,3}$. The duration t_{ts} of the time-shifted valve switching depends on the HTF volume and the HTF flow rate, and can be

optimized. For the functional demonstration in the following, a duration of $t_{ts} = 10\,s$ is assumed to be reasonable with an HTF volume of around 0.8 dm³ between the HTF valves. A detailed evaluation of the operation optimization for various durations t_{ts} is evaluated in Chapter 3.3. The corresponding position of the HTF valves and the hydrogen valves for the repetitive states of operation (1st HC/2nd HC and the time-shifted valve switching at the beginning of each new HC) are summarized in Table 2-5. In contrast to an internal heat recovery or mass recovery generally proposed for thermally driven sorption systems [101–104], this operation optimization is based on an intelligent control only. Consequently, no additional valves or piping have to be implemented in the system. It should be noted that the fluid exchange losses are not included in the analytical equations for the cooling power presented in Chapter 1.3.2.

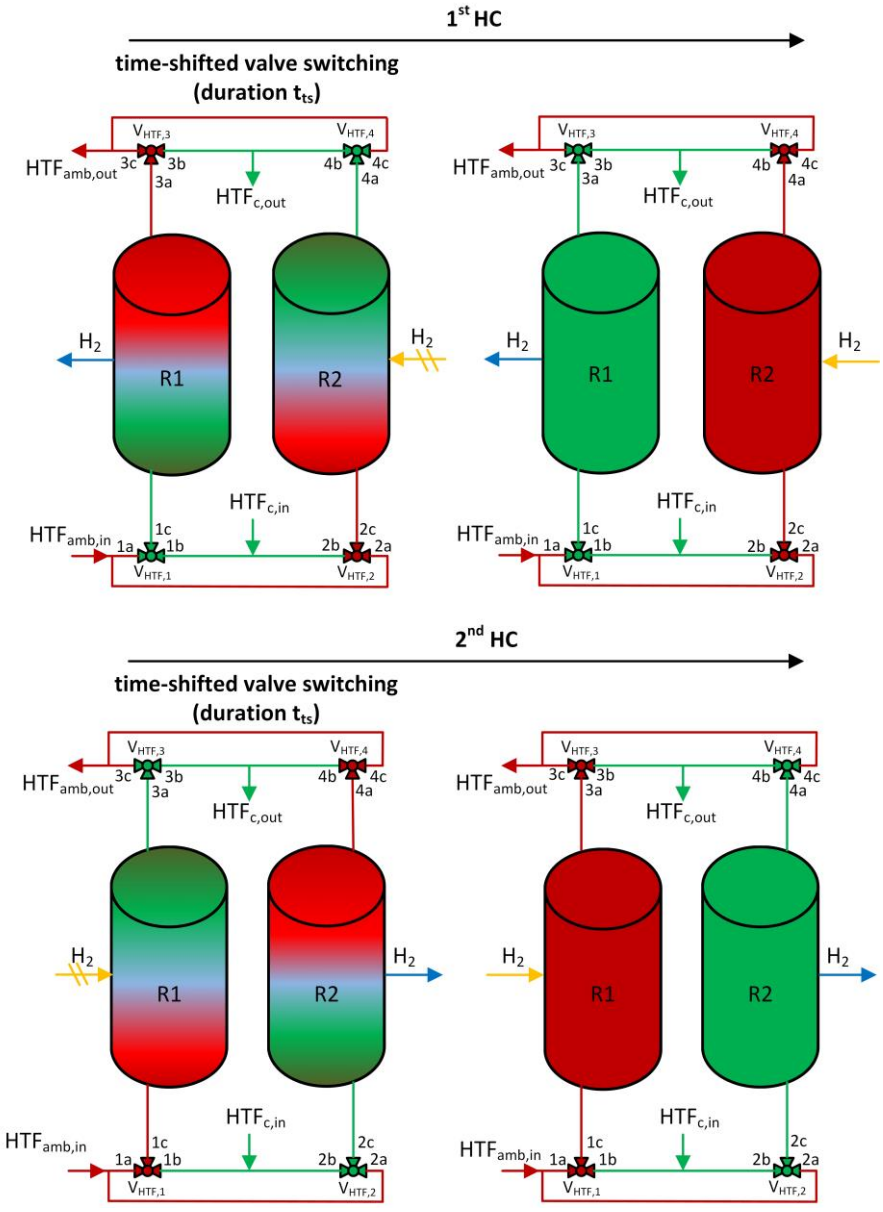

Figure 2-8: Illustration of the states of operation of the open MHCS. Top: HTF flow and hydrogen flow in the 1st HC, bottom: HTF flow and hydrogen flow in the 2nd HC.

Conclusions of the experimental details

In this section the experimental details were presented, which are required for the systematic investigation of the open MHCS. For this purpose, Hydralloy C2 was identified as suitable MH with regard to the automotive pressure and temperature conditions. The material was thermodynamically characterized in the range from 0 to 50°C and the applied polynomial fitting method is suitable to describe the PCIs, as the mean value deviation in the plateau region is below 7%. As an MH reactor, two plate reactors filled with around 2×1.5 kg of Hydralloy C2 were realized, which fulfil the presented requirements for the reactor design. For the demonstration of the first-of-its-kind system, an experimental setup was built that consists of a hydrogen section and a HTF infrastructure section. Furthermore, a novel operation optimization was introduced in order to increase the system performance during the continuous operation. By means of these experimental details and the realized setup, in the following parts of the thesis, a first functional demonstration and detailed performance investigation of the open MHCS can be conducted.

3. Functional demonstration

Based on the previously presented experimental details, in this section the first functional demonstration of the open MHCS is presented. It is investigated whether the alternately operating MH reactors are able to continuously supply the hydrogen mass flow rate required for the FC operation without disturbing its functionality. If so, what cooling power can be obtained in the HTF cycle when the system is directly coupled to an FC and to what extent the potential energy of hydrogen can be transformed into useful cold. In the following, initially, the reference operating conditions are given before the experimental results of the functional demonstration are presented in detail. Then, the novel operation optimization that aims to reduce the thermal losses is evaluated and an error analysis of the presented experimental results is conducted. The contents of this section have already been published in [118].

Experimental procedure and definition of the reference conditions

For the functional demonstration, the following reference conditions are applied: The absorption pressure at PRV1 is set to 35 bar, while at PRV2 the reactor outlet pressure is reduced to a maximum of $p_{\mathrm{PRV2}} = 5.4$ bar to protect the FC from exceedingly high pressure. The HCs are switched when the reactor outlet pressure is below the switching pressure of $p_{\mathrm{sw}} = 4.3\,\mathrm{bar}$, and, at the beginning of each HC, the duration of the time-shifted valve switching is set to $t_{\mathrm{ts}} = 10$ s. The average inlet temperatures of the ambient and cooling HTF cycle are $T_{\mathrm{in,amb}} = 30.1$ °C and $T_{\mathrm{in,c}} = 20.2$ °C, respectively, and the corresponding HTF flow rates are adjusted to $\dot{V}_{\mathrm{HTF,amb}} = 5.77\,\mathrm{l\,min^{-1}}$ and $\dot{V}_{\mathrm{HTF,c}} = 7.98\,\mathrm{l\,min^{-1}}$. The FC operates constantly with an average electrical power of $P_{\mathrm{el}} = 4.98$ kW. Table 3-1 gives an overview of these reference conditions.

Table 3-1: Overview of reference conditions.

Parameter	Symbol	Value
Electrical FC power	P_{el}	~5 kW
Inlet temperature of the ambient HTF loop	$T_{\mathrm{in,amb}}$	30.1 °C
Inlet temperature of the cooling HTF loop	$T_{\mathrm{in,c}}$	20.2 °C
Absorption pressure	p_{abs}	35 bar
Switching pressure	p_{sw}	4.3 bar
Duration of the time-shifted switching	t_{ts}	10 s

After an initial run-in period of four half-cycles and when constant operating conditions are obtained, the experiment is run for 15 minutes, of which 500 s are shown in the following. For the hydrogen section, the values of the HC time t_{HC}, the total released hydrogen mass $m_{\mathrm{H2,out}}$ as well as the thermal losses each refer to reactor R1 and the first presented HC. The theoretically usable hydrogen capacity $\Delta\omega_{\mathrm{max}}$ for the calculation of the hydrogen utilization factor F according to equation (2-1) is determined based on the polynomial fit of the PCIs of

Hydralloy® C2. For the HTF infrastructure section, the presented values of the average cooling power and the cooling efficiency are calculated for the entire duration of the experiment t_{exp} and the average hydrogen mass flow rate. For determining the ratio of $\dot{Q}_{\mathrm{HTF,avg}} \cdot {P_{\mathrm{el,et}}}^{-1}$ independent from the FC operation, an equivalent electrical FC power $P_{\mathrm{el,et}}$ for an FC efficiency of 50% is determined based on equation (1-11) and the measured average hydrogen mass flow rate.

According to the description of the experimental setup, in the following, first the hydrogen section is evaluated in detail, before the temporal course of the HTF temperature and the resulting cooling power in the HTF infrastructure section are shown. The inlet temperature of the ambient HTF loop and the inlet temperature of the cooling HTF loop are partially referred to as the ambient temperature and cooling temperature.

3.1 Results of the hydrogen section

At the top of Figure 3-1, the temporal course of the pressure of reactor R1 (p_{R1}) and reactor R2 (p_{R2}) are illustrated under these reference conditions. Next to this, the hydrogen mass flow rates $\dot{m}_{\mathrm{H2,in}}$ (absorbed by the reactors) and $\dot{m}_{\mathrm{H2,out}}$ (desorbed by the reactors) as well as the electrical FC power P_{el} are shown at the bottom. From the pressure profiles, the alternating operation of the reactors between a maximum pressure of around 35 bar and minimum pressure of 6 bar can be observed. During the duration of 500 s, three complete HCs (two times 1st HC and one time 2nd HC) are passed. According to the states of operation in Table 2-5, in the 1st HC reactor R1 desorbs hydrogen to the FC, and a reduction of p_{R1} can be seen. In the subsequent 2nd HC, the pressure of R1 increases again due to the absorption, while reactor R2 alternately passes the same pressure levels.

The detailed temporal course of the pressure during a single desorption can be explained as follows: At the start of each cooling HC, a sharp pressure drop of around $\Delta p = 15\ \mathrm{bar}$ can be observed, since when the hydrogen valves $V_{H2,1\text{-}2}$ at the reactor outlet are opened, a free volume expansion occurs (volume between $V_{H2,1\text{-}2}$ and the FC inlet). Subsequently, the pressure continuously decreases as a constant hydrogen mass flow rate is supplied to the FC and the system pressure is below the equilibrium pressure of Hydralloy® C2. With ongoing transformed fraction, the characteristic plateau region of Hydralloy® C2 is reached, and a reduction of the pressure decline can be observed (see PCIs in Figure 2-3). The corresponding cooling HC is completed when the switching criterion $p_{\mathrm{sw}} < 4.3\ \mathrm{bar}$ is reached. Then, the previously absorbing reactor subsequently starts feeding the FC.

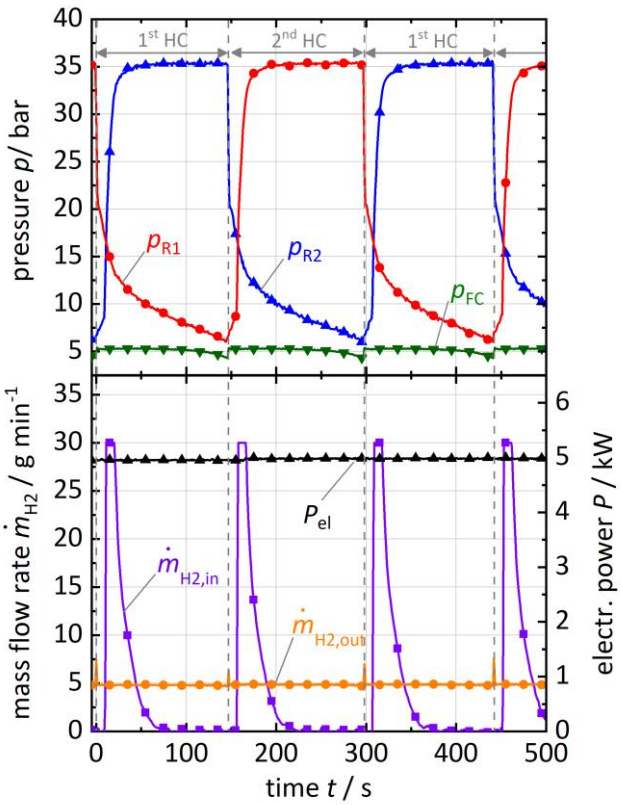

Figure 3-1: Top: Temporal course of the reactor pressures and the FC inlet pressure. Bottom: Temporal course of the hydrogen mass flow rates (inlet and outlet) and the electrical FC power.

From the profile of the outlet mass flow rate $\dot{m}_{\mathrm{H2,out}}$, it can be seen that the alternately desorbing reactors are able to continuously provide the required hydrogen mass flow rate to the FC and its operation is unaffected from the two alternately desorbing reactors. Thus, the functionality of system is ensured. The value of $\dot{m}_{\mathrm{H2,out}}$ is constant (average hydrogen mass flow rate of 4.86 g min^{-1}) since it is directly affected by the hydrogen consumption of the FC. According to equation (2-6), the FC efficiency corresponds to $\eta_{\mathrm{FC}} = 51\%$. During the 1st HC ($0\ \mathrm{s} \leq t \leq 145\ \mathrm{s}$), reactor R1 releases a total hydrogen mass of $m_{\mathrm{H2,out}} = \int_{0\ \mathrm{s}}^{145\ \mathrm{s}} \dot{m}_{\mathrm{H2,out}}(t)dt = 11.80\ \mathrm{g}$ to the FC. Thus, the actually used hydrogen capacity is $\Delta\omega = 0.83\ \mathrm{wt.\%}$ with $m_{\mathrm{MH,R1}} = 1.43\ \mathrm{kg}$, which is in good accordance with the desorption of reactor R2 in the 2nd HC. Related to the theoretically usable hydrogen capacity of $\Delta\omega_{\mathrm{max}} = 1.32\ \mathrm{wt.\%}$, the hydrogen utilization factor under reference conditions corresponds to $F = 0.63$ (see equation (2-1)).

In contrast to the desorption, the mass flow rate of the regeneration HC $\dot{m}_{\mathrm{H2,in}}$ is not influenced by the hydrogen consumption of the FC. At the beginning of each absorption, the inlet pressure is increased to $p_{\mathrm{PRV1}} = 35$ bar. Since this pressure is above the equilibrium pressure, the reactor starts absorbing, and a sharp increase of $\dot{m}_{\mathrm{H2,in}}$ can be observed. For a period of $\Delta t = 9\ \mathrm{s}$, a value of $\dot{m}_{\mathrm{H2,in}} = 30\ \mathrm{g\ min^{-1}}$ is reached, which corresponds to the maximum measuring range of 333 sL min^{-1} of the applied mass flow meter MFM1. According

to the measured values of the MFM1, the total absorbed hydrogen mass of reactor R1 ($m_{\mathrm{H2,in}} = 10.71$ g) in the 2nd HC is less when compared to the released hydrogen mass in the 1st HC. Thus, at the first seconds of each absorption, the actual absorbed mass flow rate might be even higher.

Subsequently, $\dot{m}_{\mathrm{H2,in}}$ decreases due to the characteristics of the MH reaction. Firstly, the effective reaction rate (proportional to the hydrogen mass flow rate) decelerates with increased amount of absorbed hydrogen and ongoing transformed fraction [18]. Additionally, the effective reaction rate strongly depends on the distance of the system pressure p from the equilibrium pressure p_{eq} (increases during the reaction), which for Hydralloy® C2 is expressed by the normalized pressure dependence method [132]. As a system response to the increase of pressure at the start of each absorption, a first order reaction can be assumed, which is characterized by the time constant τ [31]. This time constant is the required time to reach 63.2% of the total absorbed hydrogen mass $m_{\mathrm{H2,in}}$. The absorption is assumed to be completed after a time interval of 5τ and a transformed fraction of 99.3% . Thus, for reactor R1 the absorption in the 2nd HC is completed after a duration of $\Delta t = 74$ s (in good accordance with reactor R2 in the 1st HC). This value shows that under reference conditions the duration of the desorption determines the HC time of the system, which allows a fast preparation of the absorbing reactor for the subsequent coupling to the FC.

To demonstrate the automatic system operation and the switching of the HCs, in Figure 3-2 the FC inlet pressure of the 2nd HC is illustrated in detail. It shows that the FC operates between two pressure levels $p_{\mathrm{PRV2}} = 5.4$ bar and $p_{\mathrm{FC,min}} = 4.3$ bar. These pressure levels are defined by the PRV2 and the defined switching criterion of the system. At the start of the 2nd HC ($t = 146$ s), an increase of FC inlet pressure can be observed, which is caused by the switching from the desorbing reactor R1 to the previously absorbing reactor R2. Subsequently, the FC inlet pressure decreases due to the desorption of hydrogen and increasing transformed fraction. At $t = 296$ s, the switching criterion is fulfilled, which corresponds to a HC duration of $\Delta t_{\mathrm{HC}} = 150$ s. This value is in good accordance with the duration of the 1st HC. When the pressures of p_{FC} and p_{R1} are compared at the point of switching, a pressure difference of around $\Delta p = 1.8$ bar can be observed, which is probably caused by a pressure drop in the mechanical pressure reducing valve PRV2.

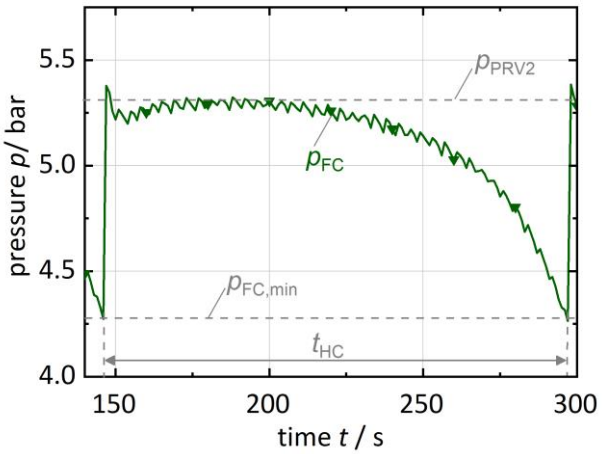

Figure 3-2: Temporal course of the FC inlet pressure for the 2nd HC.

3.2 Results of the HTF infrastructure section

To determine the resulting cooling power, the HTF temperature profiles of the reactors and the cooling HTF loop are of interest. In Figure 3-3, the HTF inlet temperatures and outlet temperature of reactor R1 (top) and reactor R2 (bottom) are presented. The temperature profiles of $T_{\mathrm{in,R1}}$ and $T_{\mathrm{in,R2}}$ show the two operating temperature levels of the cooling HC ($T_{\mathrm{in,c}} \approx 20$ °C) and the regeneration HC ($T_{\mathrm{in,amb}} \approx 30$ °C). Thus, at each point of switching, a sharp increase (regeneration HC) or decrease (cooling HC) of the inlet temperature can be observed. The oscillation around the set values results from the regulation of the thermostatic baths TB_{amb} and TB_C.

In the following, the detailed temporal course of the outlet temperature $T_{\mathrm{out,R1}}$ of reactor R1 is described. To generate a continuous cooling effect, reactor R2 alternately passes the same operation and its behaviour is analogue. At $t = 0$ s, the cooling HC of R1 is initiated and the cooling HTF flows through the previously absorbing reactor with an initial temperature of 30 °C. For the duration of $\Delta t = 20$ s, the outlet temperature is above the inlet temperature. Therefore, a negative cooling power is generated, which is a result of thermal losses that occur in the continuous system operation. At the beginning of each desorption HC, the total reactor mass including the passive reactor mass and the active MH mass has to be cooled from the ambient temperature level T_{amb} to the cooling temperature level T_{c}. Consequently, a part of the reaction enthalpy is used internally to cool down the reactor and the MH mass instead of cooling down the HTF. This effect is referred to as sensible heat losses (see Chapter 1.3.2). Due to the endothermic desorption of hydrogen and when no more ambient HTF is in the reactor, for $t \geq 20$ s the outlet temperature is below the inlet temperature and a cooling effect is generated. Since the desorbed mass flow rate is controlled by the hydrogen consumption of the FC, an almost homogeneous profile of $T_{\mathrm{out,R1}}$ is obtained.

At $t = 145$ s, the pressure-controlled switching criterion is reached, and the regeneration HC of R1 is initiated by increasing the inlet temperature. Initially, the total reactor mass is on cooling temperature level, and there is cold HTF in the reactor volume ($T_{\mathrm{out,R1}} = 17.9\,°\mathrm{C}$) while ambient HTF enters at the inlet. As a result, at the beginning of the regeneration HC the outlet temperature is below the inlet temperature. When the absorption of hydrogen is initiated at $t = 156$ s by opening the hydrogen valve $V_{H2,2}$, the heat of formation of the exothermic reaction is transferred to the HTF, and an increase of the HTF outlet temperature can be observed. The temperature profile of $T_{\mathrm{out,R1}}$ in the regeneration HC is less homogeneous in contrast to the cooling HC, since the hydrogen mass flow rate is not affected by the hydrogen consumption of the FC. Therefore, for the very high hydrogen mass flow rates $\dot{m}_{\mathrm{H2,out}}$ at the beginning of the absorption, a maximum temperature increase of $\Delta T = T_{\mathrm{out,R1}} - T_{\mathrm{in,R1}} = 11.2$ K can be seen. With reduced hydrogen mass flow rate $\dot{m}_{\mathrm{H2,out}}$, there is a decline of the outlet temperature $T_{\mathrm{out,R1}}$. When a transformed fraction of 99.3% of the total absorbed hydrogen mass $m_{\mathrm{H2,in}}$ is reached at $t = 230$ s, the absorption is assumed to be completed [31], and the temperature difference between reactor inlet and outlet is below 0.4 K (remaining sensible heat). Finally, at $t = 296$ s the switching criterion of the 2nd HC is fulfilled by the desorption of hydrogen in reactor R2, and the 1st HC is started again.

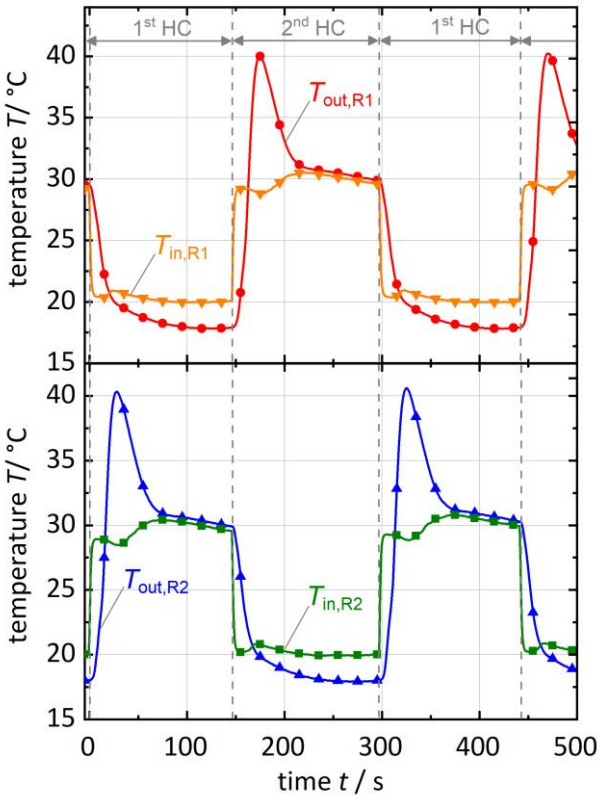

Figure 3-3: Temporal course of the inlet and outlet temperatures of reactors R1 (top) and R2 (bottom).

To evaluate the resulting cooling power and to demonstrate the influence of the thermal losses, the top of Figure 3-4 shows the temporal course of the inlet temperature $T_{\mathrm{in,c}}$ and the outlet temperature $T_{\mathrm{out,c}}$ of the cooling HTF loop. The decline of the outlet temperature $T_{\mathrm{c,out}}$ in the cooling HTF loop is generated by the alternating operation of reactors R1 and R2 according to the system operation and the reactor temperature profiles of Figure 3-3. Thus, a quasi-continuous cooling effect is obtained, which can be seen in the resulting power of the cooling HTF loop at the bottom of Figure 3-4. According to equation (2-7), positive values of the HTF power correspond to a cooling effect while negative values indicate a heat input.

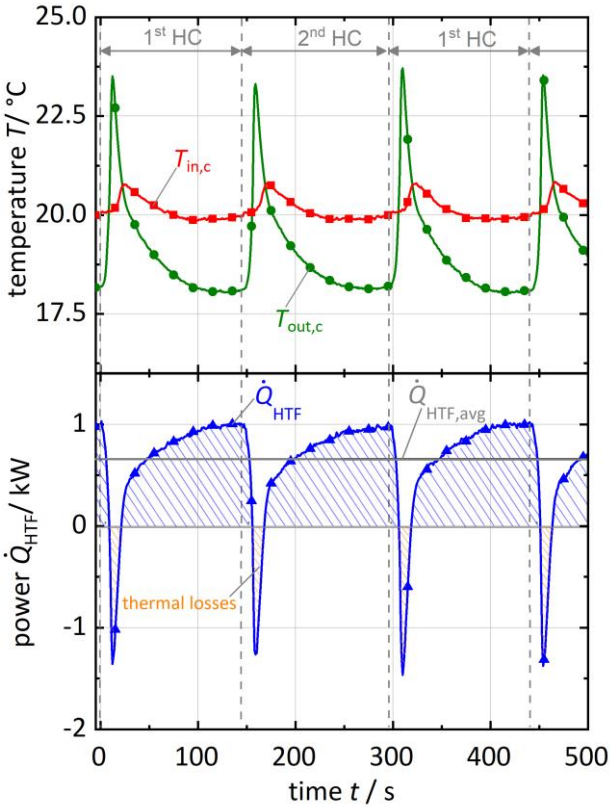

Figure 3-4: Temporal course of the inlet and outlet temperatures of the cooling HTF loop (top) and the resulting cooling power (bottom).

At the beginning of each HC, a heat input phase (HIP) and a negative peak of the cooling power of around -1.3 kW can be observed before an actual cooling effect is generated. This heat input is caused by thermal losses (sum of sensible heat losses and fluid exchange losses) and the reactor operation at the two temperature levels. The maximum temperature difference of up to 2.2 K between the cooling HTF inlet and outlet in the actual cooling phase (CP) results in a maximum cooling power $\dot{Q}_{\mathrm{HTF,max}}$ of around 1 kW. For the entire experimental duration of $t_{\mathrm{exp}} = 15\ \mathrm{min}$, an average cooling power of $\dot{Q}_{\mathrm{HTF,avg}} = {t_{\mathrm{exp}}}^{-1} \int_0^{t_{\mathrm{exp}}} \dot{Q}_{\mathrm{HTF}}(t)dt = 662\ \mathrm{W}$ is reached. This value is equal to a ratio of $\dot{Q}_{\mathrm{HTF,avg}} \cdot {P_{\mathrm{el,et}}}^{-1} = 13.6\%$, and corresponding to equation (2-8) a cooling efficiency of $\eta_{\mathrm{c}} = 75\%$ is obtained. Thus, for the present system and the defined reference experimental conditions, thermal losses reduce the cooling efficiency

by around 25% compared to the maximum obtainable cooling power. Referred to the MH mass of reactor R1 with $m_{\mathrm{MH,R1}} = 1.43\,\mathrm{kg}$, the specific cooling power (SCP) is equal to 463 W kg_{MH}^{-1}. As shown in the literature review, this value is commonly applied to compare the performance of different sorption systems. For the SCP of the total system, the mass of auxiliary components, such as valves and piping, has to be taken into account next to the mass of the reactors. Since these auxiliary components are not optimized in the present first-of-its-kind system, the SCP of the total system is not applied in this thesis.

From these values, it can be derived to what extent the potential energy of compressed hydrogen can be reutilized by generating a cooling effect in the HTF cooling loop: Under reference conditions with an average hydrogen mass flow rate of $4.86\,\mathrm{g\,min^{-1}}$ and an absorption pressure of 35 bar, the present system can be operated for $t = 205\,\mathrm{min}$ per kg of hydrogen. With an average cooling power of 662 W, this is equal to a total transformed cold of 8.16 MJ kg_{H2}^{-1}. Referred to the compression work of 18 MJ kg_{H2}^{-1} that is required for the pressure increase to 700 bar according to Chapter 1.4.2, therefore, around 45% of the potential energy of hydrogen can be transformed into useful cold under these reference conditions. This value even increases for a reduced initial hydrogen pressure in the storage tank, e.g. for 350 bar tanks. In relation to the maximum useful work of -1.22 MJ kg_{H2}^{-1}, which can be can be extracted between an absorption pressure of 35 bar and an FC backpressure of around 5 bar, the ratio of total transformed cold to the maximum useful work corresponds to 6.7. As shown before, except of the electrical energy that is required for the auxiliary components (HTF pumps and valves), the system is purely driven by the onboard available and so far not exploited potential energy of compressed hydrogen in the storage tank. Since this electrical power is not measured in the setup, it is difficult to specify the COP for the present open MHCS. As a rough estimation, for an electrical power of the auxiliary components of around 100–125 W and an average cooling power of 662 W, the COP under reference conditions is equal to 5.3–6.6 (without considering the compression work).

After presenting the results in the HTF infrastructure section, in the following section, it is evaluated to what extent the performance and cooling efficiency is increased by the implementation of the operation optimization, and the optimum duration of the time-shifted valve switching is determined.

3.3 Evaluation of the operation optimization

In the previously presented results of the functional demonstration, the effect of the operation optimization (time-shifted valve switching according to Chapter 2.4) that aims at reducing the fluid exchange losses and increasing the cooling efficiency can be seen in Figure 3-3 and Figure 3-4 as follows: At the beginning of each HC and for the duration of $t_{\mathrm{ts}} = 10\,\mathrm{s}$, the

cooling HTF loop remains connected to the reactor that was previously desorbing by means of the HTF outlet valves $V_{HTF,3\text{-}4}$. Thus, for instance, during the time-shifted valve switching at the beginning of the 1st HC and the desorption of hydrogen in reactor R1, remaining cold HTF from the outlet of reactor R2 with an initial outlet temperature of $T_{\mathrm{out,R2}} = 18\ °\mathrm{C}$ flows into the cooling HTF loop. Consequently, a cooling effect is generated in the cooling HTF loop, although the operating temperature levels are changed. Accordingly, the temporal course of $\dot{m}_{\mathrm{H2,in}}$ (bottom of Figure 3-1) also shows the delayed hydrogen supply to the absorbing reactor, since the heat of formation of absorption would increase the temperature in the cooling HTF loop. Furthermore, it is avoided that remaining hot ambient HTF from the previously absorbing reactor R1 with an initial outlet temperature of $T_{\mathrm{out,R1}} = 29.5\ °\mathrm{C}$ (see Figure 3-3) gets into the cooling HTF loop.

To demonstrate the operation optimization, the top of Figure 3-5 shows a comparison of the cooling power of the cooling HTF loop in the case of $t_{\mathrm{ts}} = 10\ \mathrm{s}$ (result of the functional demonstration) and $t_{\mathrm{ts}} = 0\ s$ (simultaneous switching of the HTF inlet valves and the HTF outlet valves). It can be seen that the profiles show different characteristics of the HIP while the maximum cooling power is unaffected by varying t_{ts}. For the simultaneous switching of the HTF valves, at the beginning of each HC, remaining ambient HTF flows into the cooling HTF loop. Thus, the thermal losses are increased up to a negative peak value of −3.5 kW. The total heat input in the 1st HC corresponds to −31.1 kJ compared to a value of −9.1 kJ for the functional demonstration. As a result, the average cooling power for $t_{\mathrm{ts}} = 0\ \mathrm{s}$ ($\dot{Q}_{\mathrm{HTF,avg}} = 489\ \mathrm{W}$) is 26% less compared to $t_{\mathrm{ts}} = 10\ \mathrm{s}$. The effect of the operation optimization can be observed as well when the cooling power in the cooling HTF loop and the reactor cooling power are compared, which is shown in the Appendix F.

In order to determine the optimum duration of the time-shifted valve switching for a maximum cooling efficiency η_{c}, t_{ts} is varied in the range of 0–26 s. Except for t_{ts}, the same experimental reference conditions are applied as in the functional demonstration of the system, and each experiment was run for 15 min. The resulting cooling efficiencies for varying t_{ts} are presented at the bottom of Figure 3-5. It can be seen that the maximum cooling efficiency of $\eta_{\mathrm{c}} = 81\%$ is reached for $t_{\mathrm{ts}} = 12\ \mathrm{s}$. For this duration, the average cooling power is $\dot{Q}_{\mathrm{HTF,avg}} = 766\ \mathrm{W}$, and a ratio of $\dot{Q}_{\mathrm{HTF,avg}}\ {P_{\mathrm{el,et}}}^{-1} = 14.7\%$ was reached. Compared to the experiment without the implementation of the operation optimization and the simultaneous switching of the HTF valves ($t_{\mathrm{ts}} = 0\ \mathrm{s}$), the average cooling power can be increased by around 57%. For $t_{\mathrm{ts}} > 15\ \mathrm{s}$, a decrease of cooling efficiency can be observed since when the duration t_{ts} is too long, ambient HTF from the inlet of the absorbing reactor flows into the cooling HTF loop.

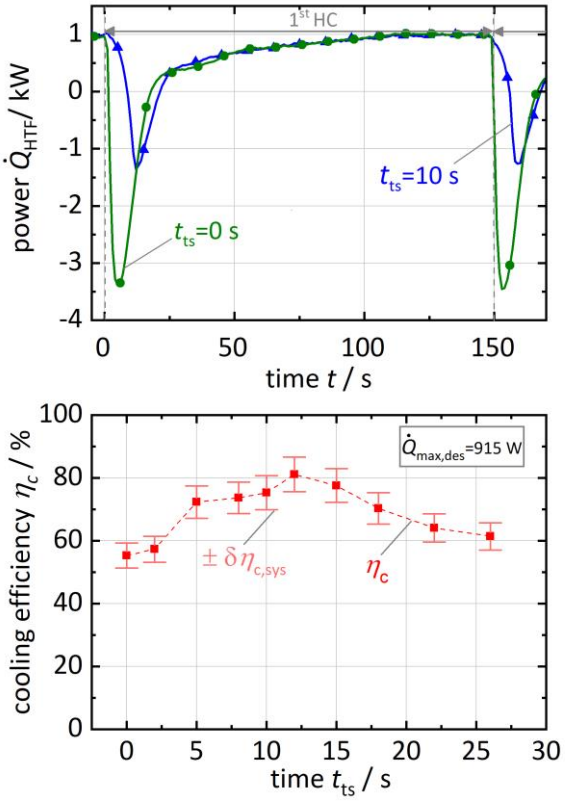

Figure 3-5: Top: Temporal course of the power of the cooling HTF loop for $t_{\mathrm{ts}} = 0$ s and $t_{\mathrm{ts}} = 10$ s. Bottom: Cooling efficiency η_{c} with error bars for different durations t_{ts} of the operation optimization. The maximum obtainable cooling power $\dot{Q}_{\mathrm{max,des}}$ corresponds to 915 W for an FC efficiency of 50%.

3.4 Error analysis of the cooling performance

To complete the functional demonstration and to prepare for a more detailed performance investigation in Chapter 4, in the following, an error analysis of the cooling power and the cooling efficiency is conducted. These values are the crucial characteristic of the present open MHCS. The corresponding fundamentals and equations for this error analysis are illustrated in [133].

Error analysis of the cooling power

According to equation (2-7), the transferred cooling power in the cooling HTF loop is measured by a caloric measurement, which is based on a measurement of the temperature difference $\Delta T = T_{\mathrm{in,c}} - T_{\mathrm{out,c}}$ and the HTF flow rate. Thus, the uncertainty of the cooling power depends on the uncertainty of the temperature sensors for the temperature difference, the uncertainty of the HTF flow meter as well as the uncertainty of the density and specific heat capacity of

the HTF. Since these uncertainties are independent and random, the resulting systematic uncertainty $\delta\dot{Q}_{\mathrm{HTF,sys}}$ can be calculated as follows:

$$\delta\dot{Q}_{\mathrm{HTF,sys}} = \sqrt{\left(\frac{\partial\dot{Q}_{\mathrm{HTF}}}{\partial\dot{V}_{\mathrm{c}}}\delta\dot{V}_{\mathrm{c}}\right)^2 + \left(\frac{\partial\dot{Q}_{\mathrm{HTF}}}{\partial\rho_{\mathrm{HTF}}}\delta\rho_{\mathrm{HTF}}\right)^2 + \left(\frac{\partial\dot{Q}_{\mathrm{HTF}}}{\partial c_{p,\mathrm{HTF}}}\delta c_{p,\mathrm{HTF}}\right)^2 + \left(\frac{\partial\dot{Q}_{\mathrm{HTF}}}{\partial\Delta T_{\mathrm{HTF}}}\delta\Delta T_{\mathrm{HTF}}\right)^2} \quad (3\text{-}1)$$

The uncertainties $\delta\dot{V}_{\mathrm{c}}$ and $\delta\Delta T_{\mathrm{HTF}}$ are derived from the accuracies of the measurement equipment according to Table 2-4. The PT100 resistance thermometers in the cooling HTF loop were temperature difference calibrated in increments of 20 K in the temperature range from 0–60 °C ($T_{\mathrm{in,c}}$ was used as a reference) and it was shown that the uncertainties are beyond <0.1 K in the entire temperature range. Therefore, for the temperature difference, an accuracy of $2 \cdot (\pm 0.002\mathrm{T})$ was applied in the error analysis. The specific heat capacity of the HTF was measured with the differential scanning calorimetry (accuracy of the measurement $\pm 3\%$) in the temperature range from 0–60 °C and the HTF density was determined using a hydrometer (accuracy of the measurement $\pm 0.4\%$).

Under reference experimental conditions with an average cooling power of $\dot{Q}_{\mathrm{HTF,avg}} = 662\ \mathrm{W}$, the resulting systematic uncertainty is equal to $\delta\dot{Q}_{\mathrm{HTF,sys}} = \pm 24\ \mathrm{W}$, which corresponds to a fractional uncertainty of $\delta\dot{Q}_{\mathrm{HTF,sys}}/\dot{Q}_{\mathrm{HTF,avg}} = 3.6\%$. The top of Figure 3-6 shows the error bars of the systematic uncertainty for the temporal course of the cooling power as well as for its average value.

To characterize the reliability of the measurements, the statistical error of random uncertainties was calculated by comparing the cooling power of six single HCs for the reference experiment, which is shown at the bottom of Figure 3-6. The standard deviation of the mean $\delta\dot{Q}_{\mathrm{HTF,stat}}$ was calculated as follows:

$$\delta\dot{Q}_{\mathrm{HTF,stat}} = \frac{\sigma_i}{\sqrt{N}} \quad (3\text{-}2)$$

Here, $N = 6$ corresponds to the total number of evaluated HCs and the standard deviation σ_i of an individual HC i was given by:

$$\sigma_i = \sqrt{\frac{1}{N-1}\sum_{i=1}^{N}(\dot{Q}_{\mathrm{HTF,avg,i}} - \dot{Q}_{\mathrm{HTF,avg}})^2} \quad (3\text{-}3)$$

Under reference conditions, the standard deviation of the mean corresponds to a value of $\delta\dot{Q}_{\mathrm{HTF,stat}} = \pm 5\ \mathrm{W}$. Thus, a fractional uncertainty of $\delta\dot{Q}_{\mathrm{HTF,stat}}/\dot{Q}_{\mathrm{HTF,avg}} = 0.7\%$ was

reached. This variation is also shown at the bottom of Figure 3-6 as red dashed line around the average cooling power. Overall, the total uncertainty of the cooling power

$$\delta\dot{Q}_{\mathrm{HTF}} = \sqrt{\delta\dot{Q}_{\mathrm{HTF,sys}}{}^{2} + \delta\dot{Q}_{\mathrm{HTF,stat}}{}^{2}} \tag{3-4}$$

corresponds to $\delta\dot{Q}_{\mathrm{HTF}} = \pm 29\mathrm{W}$ (fractional uncertainty: $\delta\dot{Q}_{\mathrm{HTF}}/\dot{Q}_{\mathrm{HTF,avg}} = 3.7\%$). Since the influence of the statistical error is comparable small, it will be neglected in the following error analysis of the cooling efficiency.

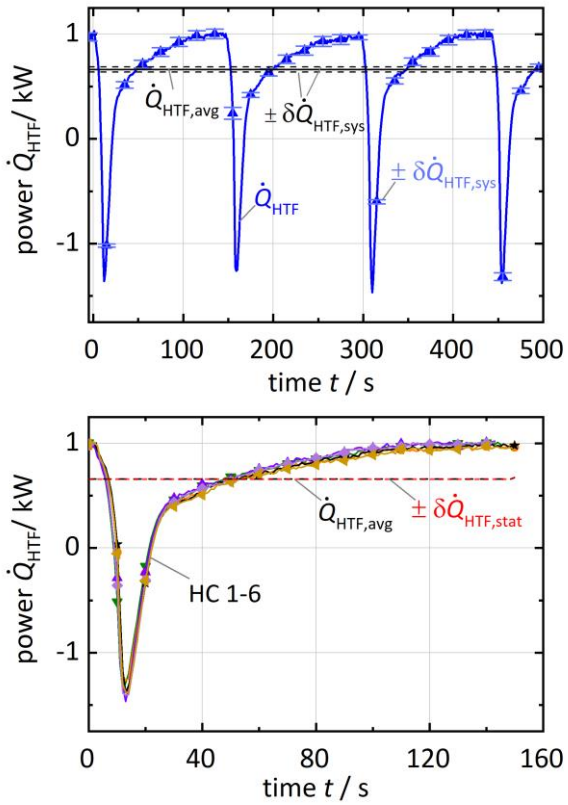

Figure 3-6: Top: Temporal course of the cooling power and the resulting average cooling power with error bars for the systematic uncertainty. Bottom: Temporal course of the cooling power for six single HCs and the resulting average cooling power with error bars for the statistical uncertainty.

Error analysis of the cooling efficiency

Corresponding to equation (2-8), the cooling efficiency is defined as ratio of the transferred average cooling power in the cooling HTF to the maximum obtainable cooling power of $\dot{Q}_{\mathrm{max,des}} = \dot{n}_{\mathrm{H2}}\,\Delta H_{\mathrm{des}}$. Thus, the uncertainty of the cooling efficiency $\delta\eta_{\mathrm{c}}$ depends on the uncertainty of the average power in the cooling HTF loop (determined before) and the

uncertainty of the maximum obtainable cooling power. The fractional uncertainty of the cooling efficiency is calculated according to:

$$\frac{\delta\eta_{\mathrm{c}}}{\eta_{\mathrm{c}}} = \sqrt{\left(\frac{\delta\dot{Q}_{\mathrm{HTF}}}{\dot{Q}_{\mathrm{HTF,avg}}}\right)^2 + \left(\frac{\delta\dot{Q}_{\mathrm{max,des}}}{\dot{Q}_{\mathrm{max,des}}}\right)^2} \tag{3-5}$$

Here, the uncertainty of the maximum obtainable cooling power $\delta\dot{Q}_{\mathrm{max,des}}$ depends on the uncertainty of the hydrogen mass flow rate and the uncertainty of the enthalpy for desorption. Similarly to equation (3-1), $\delta\dot{Q}_{\mathrm{max,des}}$ is given by:

$$\delta\dot{Q}_{\mathrm{max,des}} = \sqrt{\left(\frac{\partial\dot{Q}_{\mathrm{max,des}}}{\partial\dot{m}_{\mathrm{H2,out}}}\delta\dot{m}_{\mathrm{H2,out}}\right)^2 + \left(\frac{\partial\dot{Q}_{\mathrm{max,des}}}{\partial\Delta H_{\mathrm{des}}}\delta\Delta H_{\mathrm{des}}\right)^2} \tag{3-6}$$

The uncertainty $\delta\dot{m}_{\mathrm{H2,out}}$ is derived from the accuracy of the mass flow meter MFM2 according to Table 2-4. Corresponding to Chapter 2.1, the desorption enthalpy ΔH_{des} is calculated from the measured PCIs and the van´t Hoff equation. An accuracy of 6.1% was assumed for the enthalpy of desorption according to its dependency on the hydrogen capacity ω.

Under reference conditions, the resulting systematic uncertainty of the maximum obtainable cooling power is $\delta\dot{Q}_{\mathrm{max,des}} = \pm 53$ W (fractional uncertainty of $\frac{\delta\dot{Q}_{\mathrm{max,des}}}{\dot{Q}_{\mathrm{max,des}}} = 6.2\%$) and the fractional uncertainty of the cooling efficiency $\delta\eta_{\mathrm{c}}/\eta_{\mathrm{c}}$ finally corresponds to 7.1%. The bottom of Figure 3-5 shows the resulting error bars in the cooling efficiency for different durations of the time-shifted valve switching t_{ts}. The values of $\delta\eta_{\mathrm{c}}/\eta_{\mathrm{c}}$ are between 6.8% for $t_{\mathrm{ts}} = 12$ s and 7.2% for $t_{\mathrm{ts}} = 0$ s. The presented procedure for determining the uncertainty of the cooling efficiency is applied in the performance investigations and variation of the key influencing parameters in Chapter 4.

Conclusions of the functional demonstration

This section presented the first functional demonstration of the open MHCS. The evaluation of the hydrogen section at an electrical FC power of 5 kW showed that the alternately operating plate reactors continuously supplied hydrogen for the FC operation without disturbing its functionality. Thereby, hydrogen was absorbed at a pressure of 35 bar and the HCs with a duration of around 145 s were automatically switched when the minimum FC inlet pressure of 4.3 bar was reached. In the HTF infrastructure section, a quasi-continuous average cooling power of 662 W at an ambient temperature of 30 °C and a cooling temperature of 20 °C was detected. With regard to the maximum ratio of cooling power to electrical FC power of 18.3% for Hydralloy® C2, a cooling efficiency of 75% was reached and around 45% of the potential energy of hydrogen can be transformed into useful cold. Furthermore, in order to

reduce fluid exchange losses, the previously presented operation optimization was evaluated. The optimal duration of the time-shifted switching of the reactor outlet valves was determined as 12 s. Compared to the experiment without its implementation, the average cooling power could be increased by around 278 W, reaching a system efficiency of up to 81%. Since the resulting cooling power strongly depends on the operating conditions, in the following section a more detailed performance investigation considering the key influencing parameters is conducted.

4. Performance investigations

Similarly to vapour-compression cycles or other sorption systems, it is expected that the performance of the open MHCS strongly depends on the actual operating conditions (see the literature review in Chapter 1.4.4). Therefore, after successfully demonstrating the functionality of the system under reference conditions, in this section, a detailed performance investigation is conducted. As key influencing parameters, it is assumed that the performance depends on the two operating temperature levels – the temperature of the ambient environment and the cooling temperature level. However, since the open MHCS is directly connected to the FC, it can additionally be expected that the performance and the HC time will be highly dependent on the FC operation. This section will present the experimental results for a variation of these key influencing parameters. Using these results, it can be shown whether the system is able to work under varied operating conditions and what cooling power and cooling efficiency can be obtained. The results of this section have been published in [134].

Experimental procedure and definition of the varied operating conditions

The performance investigation is conducted based on the reference conditions of the functional demonstration as a reference experiment. Therefore, the same experimental procedure is applied and equal values of the pressure levels , HTF flow rates and the duration of the time-shifted valve switching ($t_{\mathrm{ts}} = 10\ \mathrm{s}$) were used. For varying the key influencing parameter, the desired inlet temperatures and electrical power are adjusted by means of the thermostatic baths and the electrical load, respectively. After an initial run-in period of four half-cycles and when constant operating conditions are reached, each experiment was run for around 15 minutes, of which 300 s are shown in the following. The experiments are evaluated according to the procedure described previously and Table 4-1 gives an overview of the range of varied operating and reference conditions. In the following, for each key influencing parameter, first the results for the system´s hydrogen section are presented, before the resulting thermal power in the HTF cooling loop is analysed.

Table 4-1: Overview of varied operating conditions.

Parameter	Symbol	Range	Reference
Electrical FC power	P_{el}	1.8 – 7.9 kW	~5 kW
Inlet temperature of the ambient HTF loop	$T_{\mathrm{in,amb}}$	24.3 – 42.3 °C	30.1 °C
Inlet temperature of the cooling HTF loop	$T_{\mathrm{in,c}}$	13 – 25.4 °C	20.2 °C

4.1 Variation of the electrical FC power

The cooling power of the present open system depends on the desorbed hydrogen mass flow rate of the reactors and, therefore, on the electrical FC power (see equations (1-10) and (1-11)). Since a constant operation at a specific electrical FC power cannot be expected at any case, it is important to investigate if the present system is able to operate at a reduced or increased electrical FC power and what cooling performance can be obtained for varied P_{el}.

Analysis of the hydrogen section

Figure 4-1 shows the temporal course of the hydrogen mass flow rate and the pressure profiles of the reactors R1 and R2 as well as the FC inlet pressure for three different electrical FC powers in the range of 3 –7 kW. Except for P_{el}, in all the experiments conducted reference conditions are applied.

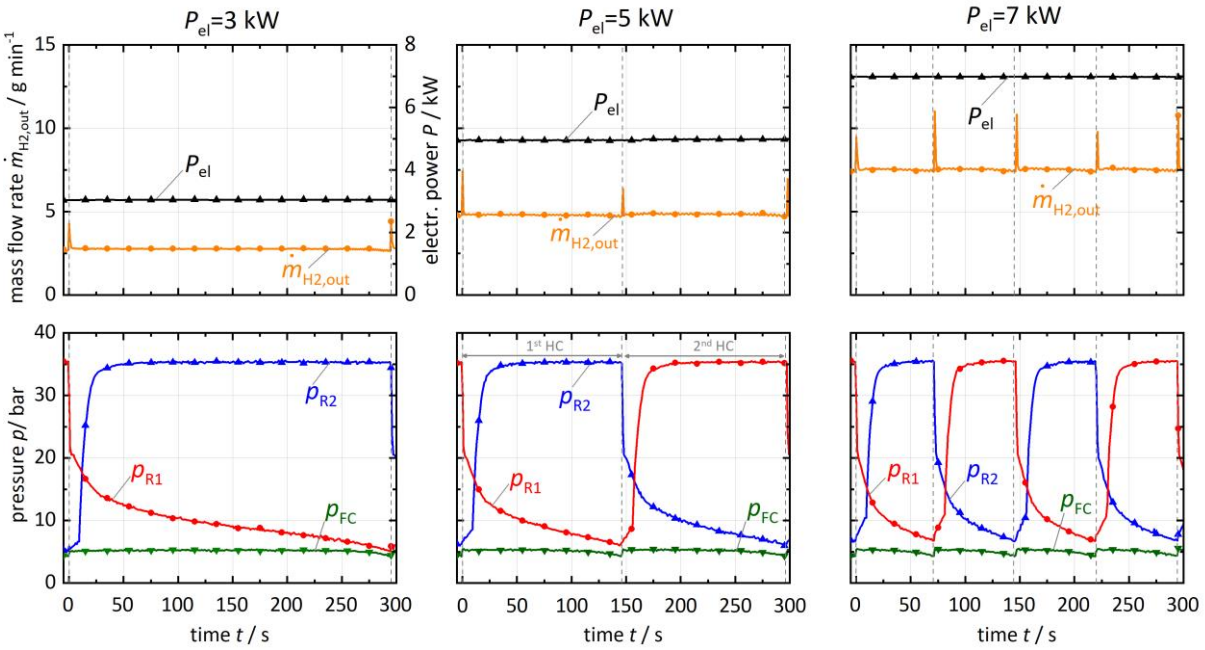

Figure 4-1: Top: Temporal course of the hydrogen mass flow rate for varied electrical FC powers. Bottom: Temporal course of the reactor pressures and the FC inlet pressure for varied electrical FC powers.

For each of the experiments with varied electrical FC powers, the characteristic alternating operation can be observed. In each 1st HC, reactor R1 desorbs hydrogen to the FC and a reduction of p_{R1} can be seen. Simultaneously, reactor R2 absorbs hydrogen from the pressure tank, which results in an increase of p_{R2}. When the FC inlet pressure reaches $p_{\mathrm{sw}} \leq 4.3$ bar, the HCs are switched and in the 2nd HC, the reactors are operated in reverse. Since the hydrogen mass flow rate of the absorption is not limited by the hydrogen consumption of the FC, the regeneration HC is faster compared to the cooling HC. Under reference conditions at $P_{\mathrm{el}} = 5\mathrm{kW}$ (middle of Figure 4-1) in the functional demonstration, the released hydrogen

mass during the HC time of 145 s was equal to 11.8 g. This experiment was conducted with an FC efficiency of $\eta_{\mathrm{FC,5\,kW}} = 51\%$ and a hydrogen utilization factor of $F_{5\,\mathrm{kW}} = 0.62$ with $w_{\max} = 1.32$ wt. % was reached.

Compared to the reference experiment, the impact of a reduced or increased electrical FC power on the profiles of the mass flow rate and the pressures can be explained as follows. Since in all experiments, the FC was kept at constant power, the profiles of $\dot{m}_{\mathrm{H2,out}}$ show a constant behaviour for the varied electrical FC powers. Corresponding to equation (1-11), for growing P_{el} an increased hydrogen mass flow rate has to be supplied by the desorbing reactors. While for $P_{\mathrm{el}} = 3\,\mathrm{kW}$ (Figure 4-1, left) the average mass flow rate corresponds to 2.73 g min^{-1}, for an enhanced electrical power of $P_{\mathrm{el}} = 7\,\mathrm{kW}$ (Figure 4-1, right), it is increased to 7.58 g min^{-1}. From the profiles of $\dot{m}_{\mathrm{H2,out}}$, it can be concluded that the reactors are able to continuously provide the required hydrogen mass flow rate in the entire range of varied P_{el}. The present MHCS is able to operate under varied electrical FC powers and the two alternately desorbing reactors do not influence the functionality of the FC. The peaks of $\dot{m}_{\mathrm{H2,out}}$ are due to the free volume expansion at the beginning of each HC. They have no influence on the corresponding FC operation, since in the profiles of the FC pressure and electrical FC power no peaks can be observed. The FC efficiency is equal to $\eta_{\mathrm{FC,3\,kW}} = 54\%$ and is reduced to $\eta_{\mathrm{FC,7\,kW}} = 46\%$ due to the increased FC heat production with growing electrical power.

Obviously, with increasing electrical FC power a reduction of the HC time can be observed, since with a growing hydrogen mass flow rate the available mass of hydrogen that can be desorbed by the reactors is consumed faster. While for an electrical power of 3 kW the HC time corresponds to 294 s, for $P_{\mathrm{el}} = 7\,\mathrm{kW}$ it is reduced to 70 s. Thus, for $P_{\mathrm{el}} = 7\,\mathrm{kW}$ the HCs have to be switched more than twice as often compared to the reference conditions and more than four times as often compared to $P_{\mathrm{el}} = 3\,\mathrm{kW}$. At an electrical FC power of 3 kW and 7 kW, the released hydrogen masses in one HC are 13.7 g and 9 g, respectively. These values show that a higher FC power results in a lower amount of hydrogen released by the reactors in one HC. Thus, along with the increased consumption of hydrogen, for growing electrical FC powers less hydrogen is available that can be supplied to the FC per HC. This is not automatically intuitive, as for a theoretical system the same amount of hydrogen should be released for increased electrical FC powers, but in a shorter time. However, this important fact for the real operation of the present system can be explained with a closer look at the reactor pressure profiles and the thermodynamic equilibrium characteristics of Hydralloy® C2. According to Figure 4-1, in the hydrogen outlet section a pressure difference between the reactor pressure and FC inlet pressure caused by PRV2 can be observed at the end of each HC (reference conditions: $\Delta p_{5\,\mathrm{kW}} = 1.8\,\mathrm{bar}$). This pressure difference increases with the growing hydrogen mass flow rates ($\Delta p_{3\,\mathrm{kW}} = 0.9\,\mathrm{bar}$ and $\Delta p_{7\,\mathrm{kW}} = 2.5\,\mathrm{bar}$). Since, at the point of switching, the reactor outlet pressures at the specific temperature are in the plateau region of Hydralloy® C2, for

growing P_{el} the theoretically usable hydrogen capacity $\Delta\omega_{\max}$ is reduced and less hydrogen is available to feed the FC. For an increase of the electrical FC power from 3 to 7 kW, the reduction of $\Delta w_{\max}$ is around 0.1 wt.%, which is equal to 1.4 g of hydrogen for the applied MH mass.

Furthermore, as it will be shown in the numerical analysis of the present plate reactor in Chapter 5, there is an additional pressure drop in the MH bed. Since the pressure at the reactor outlet determines the HC time, no more hydrogen can be released to the FC, although the average pressure in the MH bed is above the required FC backpressure. This pressure drop in the MH bed increases for growing electrical FC powers as well. Thus, the higher the FC power, the less the available MH capacity is exploited. This can be quantified by the hydrogen utilization factor, which is $F_{3\,\mathrm{kW}} = 0.69$ and $F_{7\,\mathrm{kW}} = 0.48$ for an electrical power of 3 kW and 7 kW, respectively. As an important result, the observed reduction in cycle time for higher electrical powers is not only due to the higher mass flow rate of hydrogen, but also due to the reduced amount of hydrogen available that can be released by the reactors at the corresponding pressure conditions.

Analysis of the cooling power

For the evaluation of the system´s actual cooling performance for varied electrical FC powers, the cooling power and temperature profiles in the cooling HTF loop are important. Figure 4-2 shows the temporal course of the inlet and outlet temperatures in the cooling HTF loop (top) and the corresponding power in the cooling HTF loop (bottom) for the respective electrical FC powers.

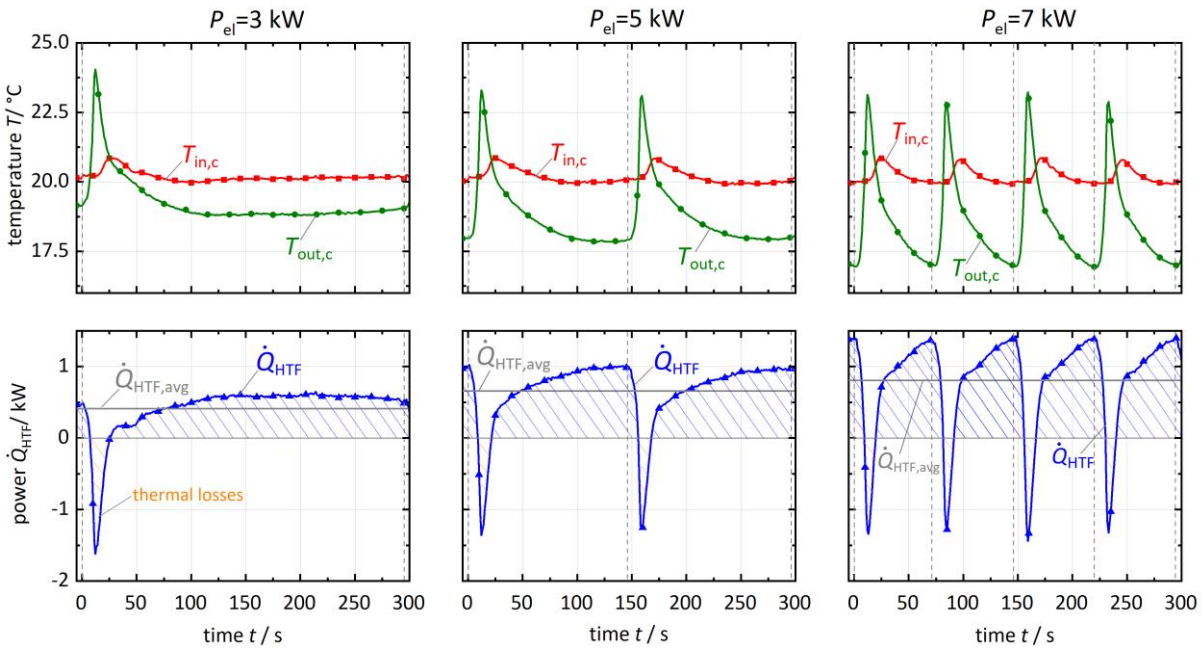

Figure 4-2: Temporal course of the inlet and outlet temperatures of the cooling HTF loop (top) and the cooling power (bottom) for varied electrical FC powers.

The temporal course of this profiles for varied P_{el} can be summarized as follows. The red lines show the inlet temperature of the HTF cooling loop $T_{\mathrm{in,c}}$, which is set to 20 °C in each conducted experiment. At $t = 0$ s and the beginning of each consecutive HC, an increase of the outlet temperature and negative peaks of the cooling power in the HIP can be observed. As previously described, this total heat input (e.g. -9.1 kJ for 13 s duration of the HIP at $P_{\mathrm{el}} = 5$ kW) is a result of thermal losses. By switching the HTF outlet valves slightly later than the inlet valves, the operation optimization with a duration of $t_{\mathrm{ts}} = 10$ s enables to reduce the fluid exchange losses. As a result of the endothermic desorption of hydrogen, with increasing duration in each HC (e.g. for $t \geq 20$ s at at $P_{\mathrm{el}} = 5$ kW) the outlet temperature $T_{\mathrm{out,c}}$ is below the inlet temperature $T_{\mathrm{in,c}}$ and a cooling effect is observed. When the pressure-controlled switching criterion is reached, the previously absorbing starts supplying hydrogen to the FC and a quasi-continuous cooling effect is obtained in the cooling HTF loop for each of the varied electrical FC powers. Under reference conditions at $P_{\mathrm{el}} = 5$ kW, an average cooling power of 662 W (SCP: 463 W kg_{MH}^{-1}) and a cooling efficiency of $\eta_{\mathrm{c}} = 75\%$ was reached.

When the profiles for an electrical FC power of 3 kW (Figure 4-2, left) and 7 kW (right) are compared to the reference conditions, it can be seen that for increasing P_{el} both the maximum obtainable temperature difference $\Delta T = T_{\mathrm{out,c}} - T_{\mathrm{in,c}}$ and the maximum cooling power $\dot{Q}_{\mathrm{HTF,max}}$ increases. This is due to the higher hydrogen mass flow rate that is directly correlated to the electrical FC power. However, at the same time an increased number of negative peaks of the cooling power can be observed, since with reduced HC time the reactors have to alternate at higher frequencies. The maximum negative peak value depends mainly on the operating temperature levels and, therefore, for varying P_{el} the same values of around -1.3 kW are obtained (the small variations are due to the regulation of the cooling inlet temperature). For higher hydrogen mass flow rates and electrical FC powers, a faster increase of $\dot{Q}_{\mathrm{HTF}}$ after each point of switching and a reduced duration of the negative peak can be observed (heat input of -14 kJ at $P_{\mathrm{el}} = 3$ kW and -8 kJ at $P_{\mathrm{el}} = 7$ kW). The resulting average cooling powers are 414 W (SCP: 290 W kg_{MH}^{-1}) and 807 W (SCP: 564 W kg_{MH}^{-1}) for an electrical FC power of 3 kW and 7 kW, respectively. Compared to the MHCSs that have been experimentally demonstrated (see Table 1-2), this value for the present first-of-its-kind system is in the range of the highest demonstrated SCP by Linder et al. [64], which is also referred to the MH mass of a single reactor. However, a major drawback of thermally driven closed MHCS is compensated with the present system: As no heat source is required for the operation, the open MHCS is superior with regard to the system efficiency. Furthermore, much larger values of the SCP for the total system are obtainable as only a reduced number of system components are required.

Analysis of the cooling efficiency

In order to compare the performance for different electrical FC powers, the cooling efficiency η_c according to equation (2-8) is applied. Figure 4-3 shows the resulting efficiencies for the experiments conducted in the range of $P_{el} = 1.8 - 7.9\,\mathrm{kW}$. Corresponding to equation (1-12), in this range the maximum obtainable cooling power $\dot{Q}_{max,des}$ for an FC efficiency of 50% is increased from 329 W at $P_{el} = 1.8\,\mathrm{kW}$ to 1446 W at $P_{el} = 7.8\,\mathrm{kW}$. However, as described above, the HC time is reduced due to higher mass flow rates of hydrogen and the reduced available amount of hydrogen at the required pressure level with increasing P_{el}. As a result, more pronounced impact of thermal losses and a reduction of the cooling efficiency for increasing values of P_{el} can be observed. At a maximum electrical FC power of 8 kW, a cooling efficiency of $\eta_c = 43\%$ is reached. This value is 16% less compared to the experiment at $P_{el} = 7\,\mathrm{kW}$. Due to this reduced efficiency, the average cooling power of 726 W at $P_{el} = 7.9\,\mathrm{kW}$ is below the system´s maximum value at $P_{el} = 7\,\mathrm{kW}$. Intuitively, a higher average cooling power with increasing desorbed hydrogen mass flow rate and electrical FC power would have been expected. A reduction of P_{el} improves the cooling efficiency up to a maximum value of $\eta_c = 84\%$ at an electrical power of 3 kW. For even a smaller electrical power a slight decrease of the efficiency can be observed, since the lower the hydrogen mass flow rates the slower the increase of $\dot{Q}_{HTF}$ at the beginning of each HC, which directly affects the resulting average cooling power.

In order to show the uncertainty of the experimental values of η_c, Figure 4-3 includes the corresponding error bars for the systematic uncertainty of the cooling efficiency $\delta\eta_c$. The corresponding values of the fractional systematic uncertainty $\delta\eta_c/\eta_c$ are between 7.1% at $P_{el} = 7.9\,\mathrm{kW}$ and 7.4% at $P_{el} = 1.8\,\mathrm{kW}$.

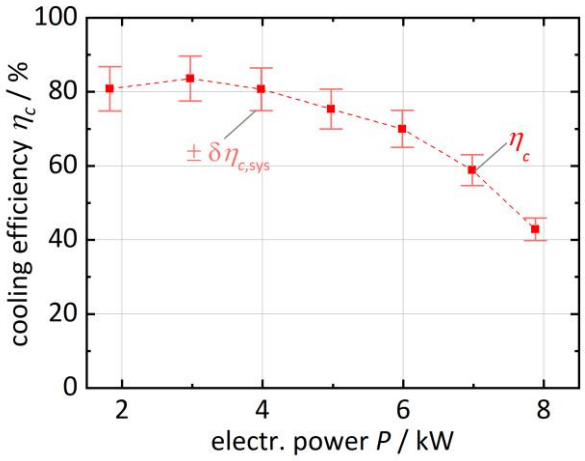

Figure 4-3: Cooling efficiency η_c with error bars for varied electrical FC powers.

4.2 Variation of the ambient temperature

The present system uses the ambient environment as a heat sink in order to release the heat of formation in the regeneration HC. Thus, the ambient temperature T_{amb} is one of the major factors that affect the performance of the open MHCS.

Analysis of the hydrogen section

Figure 4-4 shows the temporal course of the reactor pressures and the FC pressure in the hydrogen section for an inlet temperature of the ambient HTF loop of 24.3 °C (left), 30.1 °C (middle, reference experiment) and 38.7 °C (right). Except for $T_{\mathrm{in,amb}}$, reference conditions with an electrical FC power of 5 kW were applied. Therefore, the profiles of P_{el} and $\dot{m}_{\mathrm{H2,out}}$ show similar characteristics and the same values of the FC efficiency ($\eta_{\mathrm{FC}} = 49\%$) and the average mass flow rate ($\dot{m}_{\mathrm{H2,out}} = 4.86\ \mathrm{g\ min^{-1}}$) are obtained for 24.3 °C and 38.7 °C. From the temporal course of the reactor pressures, a slight reduction of the HC time can be observed with growing ambient temperature. The corresponding HC times are $t_{\mathrm{HC,24.3°C}} = 154\ \mathrm{s}$ and $t_{\mathrm{HC,38.7°C}} = 141\ \mathrm{s}$, which can be explained as follows. According to the thermodynamic characteristics of Hydralloy® C2, for a constant absorption pressure the initial hydrogen capacity of the cooling HC can be enhanced by reducing the ambient temperature. Thus, more hydrogen is available to supply hydrogen to the FC. However, for the present absorption pressure of 35 bar, the increase is comparatively small as the initial hydrogen capacity is increased by less than $\Delta\omega = 0.1\ \mathrm{wt.\%}$. Thus, similar values of the released hydrogen masses in one HC are obtained (12.5 g at $T_{\mathrm{in,amb}} = 24.3\ °\mathrm{C}$ and 11.5 g at $T_{\mathrm{in,amb}} = 38.7\ °\mathrm{C}$).

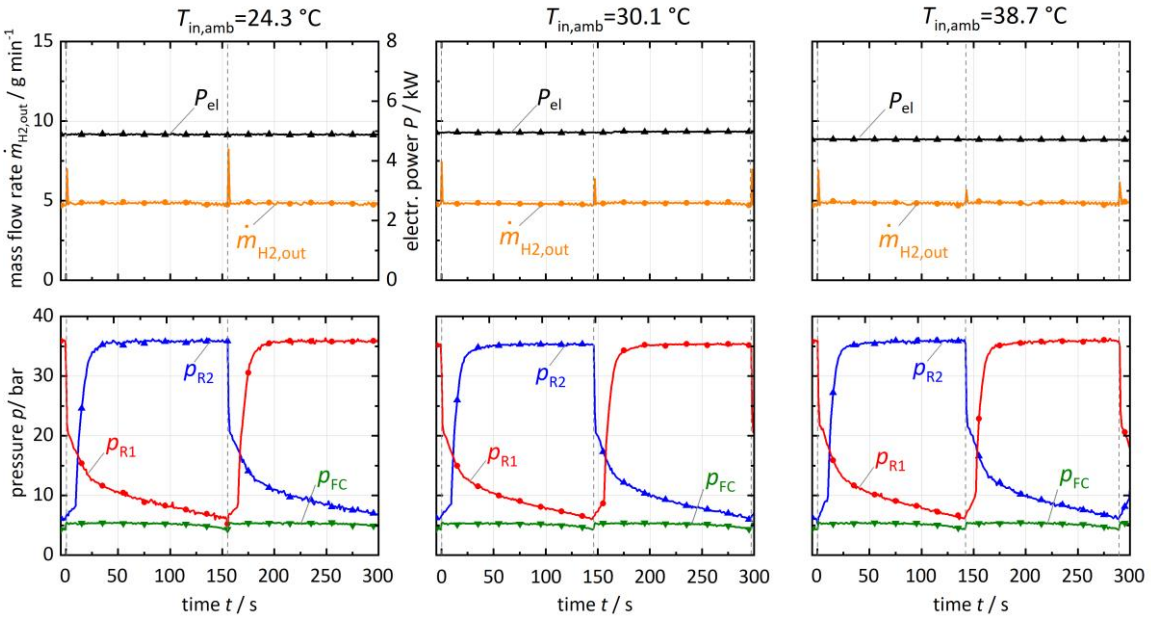

Figure 4-4: Top: Temporal course of the hydrogen mass flow rate and electrical FC power for varied inlet temperatures of the ambient HTF loop. Bottom: Temporal course of the reactor pressures and the FC inlet pressure for varied inlet temperatures of the ambient HTF loop.

Analysis of the cooling power

To evaluate the cooling performance, in Figure 4-5 the inlet and outlet temperature as well as the cooling power are presented for the three investigated inlet temperatures of the ambient HTF loop. It can be seen that the variation of $T_{\mathrm{in,amb}}$ strongly influences the resulting profiles. The maximum negative peak value as well as the duration of the negative cooling power increase with higher ambient temperature. This is obvious, as with increasing temperature difference between the ambient HTF loop and the cooling HTF loop, thermal losses increase as well. According to this explanation, for $T_{\mathrm{amb,in}} = 24.3\,°\mathrm{C}$, there is a comparably low maximum negative peak value of -0.2 kW and the total heat input after the switching corresponds to -0.7 kJ (5 s duration of the HIP). In contrast to this, for $T_{\mathrm{amb,in}} = 38.7\,°\mathrm{C}$, a maximum negative peak value of -3.4 kW is obtained, which results in a total heat input of -29kJ (19 s duration of the HIP). The detected maximum cooling powers are equal in all operation points, since the same hydrogen mass flow rates are supplied by the reactors and the FC operates at a constant power. The resulting average cooling powers are 821 W (SCP:574 W kg_{MH}^{-1}) and 412 W (SCP: 288 W kg_{MH}^{-1}) at an ambient temperature of 24.3 °C and 38.7 °C, respectively.

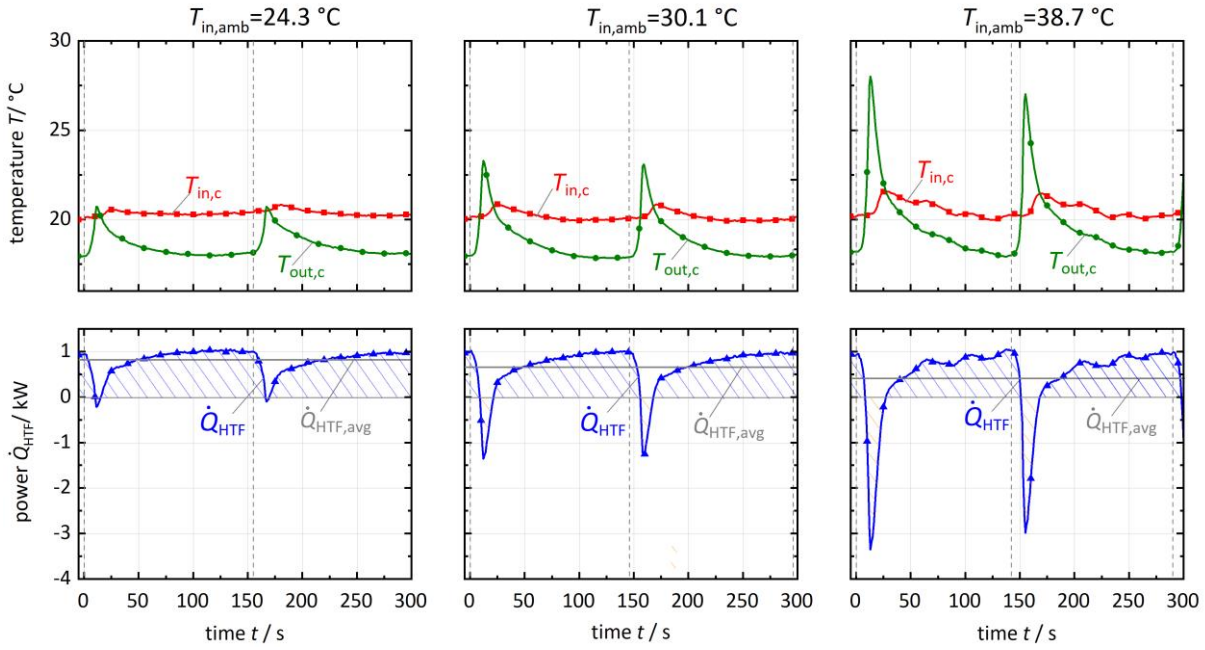

Figure 4-5: Temporal course of the inlet and outlet temperatures of the cooling HTF loop (top) and the cooling power (bottom) for varied inlet temperatures of the ambient HTF loop.

Analysis of the cooling efficiency

Figure 4-6 shows the corresponding cooling efficiencies for the variation of $T_{\mathrm{in,amb}}$ in the range of 24.3–42.3 °C. At an electrical power of 5 kW, a cooling efficiency of 100% corresponds to the maximum obtainable cooling power of $\dot{Q}_{\mathrm{max,des}} = 915\,\mathrm{W}$. It can be seen that η_{c} decreases with increasing ambient inlet temperature due impact of thermal losses (the effect

of the slightly reduced HC time is only marginal). At $T_{\mathrm{in,amb}} = 24.3$ °C, the cooling efficiency corresponds to $\eta_{\mathrm{c}} = 94\%$, while at $T_{\mathrm{in,amb}} = 42.3$ °C a value of $\eta_{\mathrm{c}} = 32\%$ is obtained. In other words, at these high temperatures around 2/3 of the available cooling effect is consumed by the prototype itself and only 1/3 can be seen as useful effect. It can be concluded that the present system is able to operate at various ambient temperatures, while its performance obviously decreases with increasing ambient temperature. However, the extent of this decrease is a matter of system and reactor design, and is addressed in the numerical analysis and optimization of the present reactor in Chapter 5.

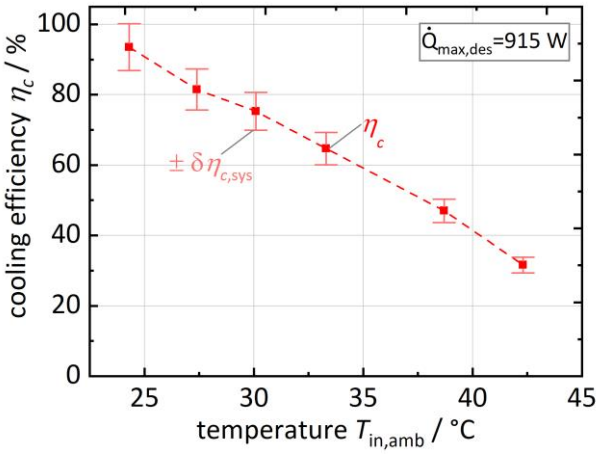

Figure 4-6: Cooling efficiency η_{c} with error bars for varied inlet temperatures of the ambient HTF loop.

4.3 Variation of the cooling temperature

Besides the ambient temperature, the temperature of the cooling HTF loop affects the operation and performance of the open MHCS. The required cooling temperature is generally determined by the final application of the system. For instance, since dehumidification of cabin air is necessary, the cooling temperature of this potential application has to be clearly lower in comparison to e.g. battery cooling. Thus, it is important to know at which cooling temperatures the present system is able to operate and which cooling power and efficiency can be obtained for a variation of $T_{\mathrm{in,c}}$.

Analysis of the hydrogen section

Figure 4-7 illustrates the results in the hydrogen section for inlet temperatures of the HTF cooling loop of 13 °C (left), 20.2 °C (middle, reference experiment) and 25.4 °C (right). Since the experiments are conducted with the same electrical FC power, the temporal courses of P_{el} and $\dot{m}_{\mathrm{H2,out}}$ show similar profiles, which is comparable to the variation of $T_{\mathrm{in,amb}}$ before. The average mass flow rates are 4.86 g min^{-1} and 4.84 g min^{-1} , and the FC efficiency corresponds to values of 48% and 49% for a cooling temperature of 13.1 °C and 25.3 °C, respectively.

In the pressure profiles, a rise in cooling temperature correlates with an increase of the HC time. This can be again explained by means of the thermodynamic equilibrium characteristics of Hydralloy® C2. According to this, a rise in cooling temperature increases the equilibrium pressure of the MH. Thus, an increased theoretically usable hydrogen capacity is obtained and more hydrogen is available to feed the FC. Based on the corresponding switching pressure, $\Delta\omega_{\max}$ is increased by around 15% when $T_{\mathrm{in,c}}$ rises from 13 to 25.4 °C. In the experiments conducted, the HC times are 90 s (released mass of hydrogen: 7.4 g) and 167 s (released mass of hydrogen: 13.5 g) for 13 °C and 25.3 °C, respectively, and the resulting hydrogen utilization factors correspond to $F_{13°\mathrm{C}} = 0.43$ and $F_{25.4°\mathrm{C}} = 0.7$. As the hydrogen has to be delivered at a constant pressure and mass flow rate, the lower utilization for a decreasing cooling temperature factor directly indicates still present heat and mass transfer limitations of the prototype reactor.

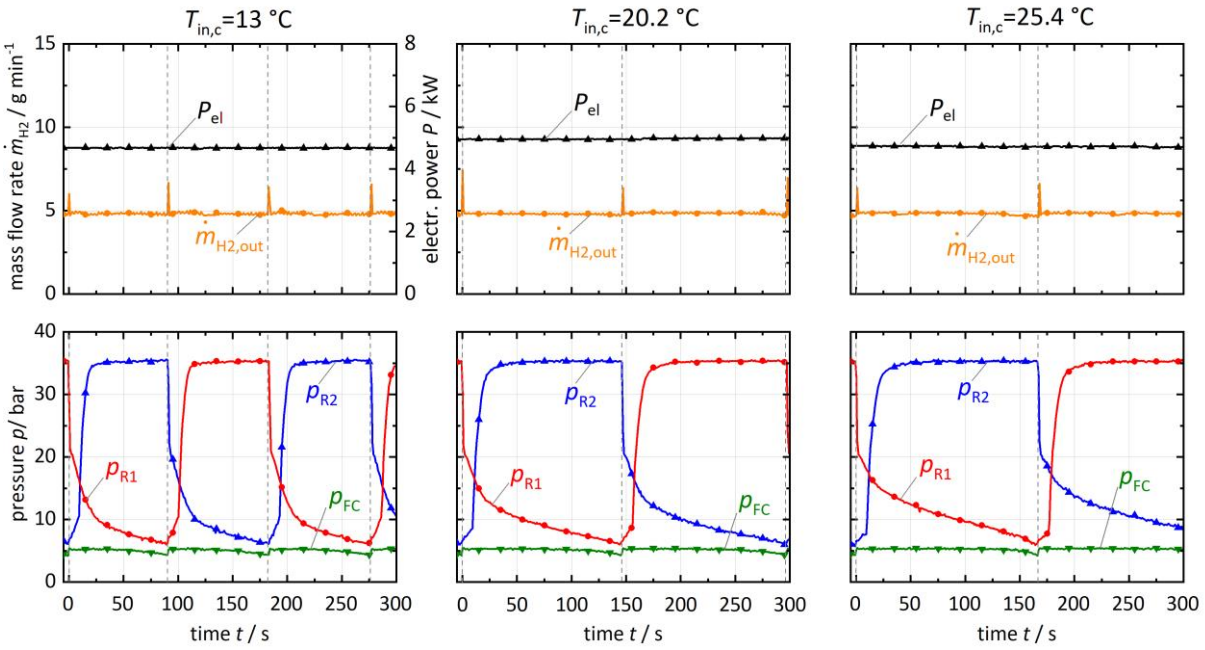

Figure 4-7: Top: Temporal course of the hydrogen mass flow rate and electrical FC power for varied inlet temperatures of the cooling HTF loop. Bottom: Temporal course of the reactor pressures and the FC inlet pressure for varied inlet temperatures of the cooling HTF loop.

Analysis of the cooling power

Figure 4-8 shows the profiles of the temperatures and the resulting power in the cooling HTF loop for these cooling inlet temperatures. With a decrease of the cooling inlet temperature, the temperature difference between the regeneration HC and the cooling HC increases. Therefore, the lower $T_{\mathrm{in,c}}$ the higher the thermal losses and the maximum negative peak value of $\dot{Q}_{\mathrm{HTF}}$. Additionally, as the HC time is reduced with decreasing cooling temperature, a higher number of negative peaks of the cooling power are obtained. For $T_{\mathrm{in,c}} = 13$ °C, the maximum negative peak value is –3.3 kW and the total heat input in one HC corresponds to -29.2 kJ (20 s duration of the HIP). Both the maximum negative peak value and the total heat input are

reduced to -0.1 kW and -0.2 kJ (2 s duration of the HIP) for $T_{\mathrm{in,c}} = 25.4$ °C. Since the same hydrogen mass flow rates are released to the FC, similar values of the maximum cooling power are obtained. The average cooling power is 838 W (SCP: 586 W kg_{MH}^{-1}) at $T_{\mathrm{in,c}} = 25.4$ °C, while $\dot{Q}_{\mathrm{HTF,avg}}$ is reduced to 178 W (SCP: 124 W kg_{MH}^{-1}) at $T_{\mathrm{in,c}} = 13$ °C.

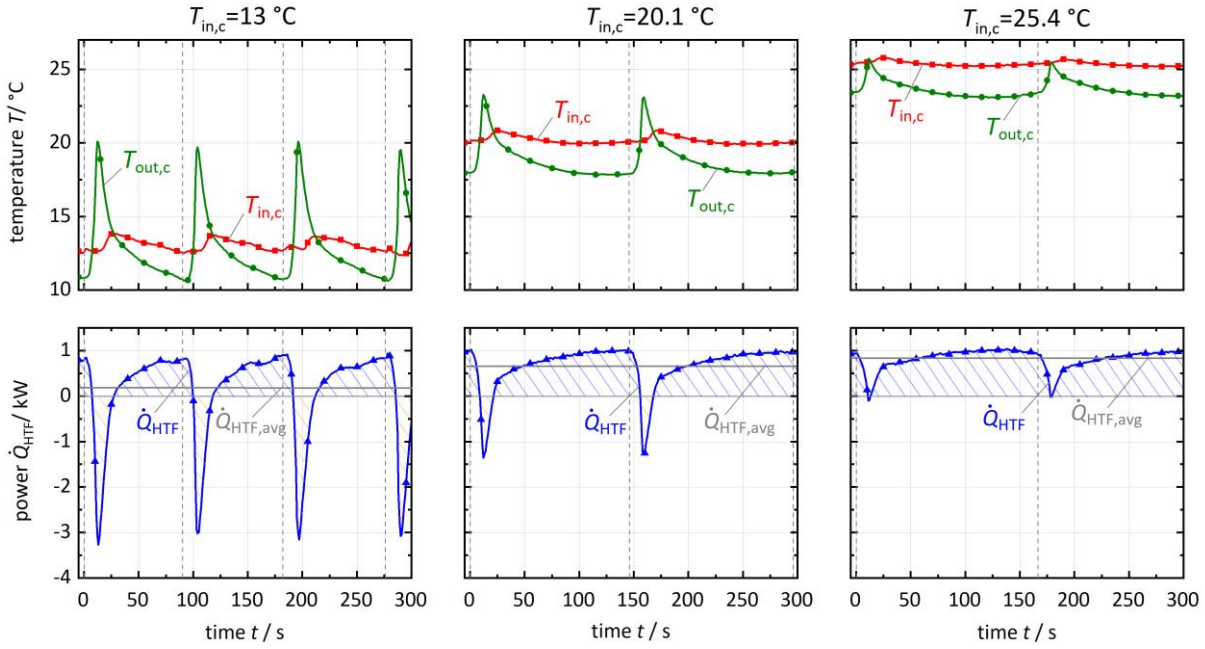

Figure 4-8: Temporal course of the inlet and outlet temperatures of the cooling HTF loop (top) and the cooling power (bottom) for varied inlet temperatures of the cooling HTF loop.

Analysis of the cooling efficiency

Figure 4-9 shows the resulting cooling efficiencies for a variation of the cooling inlet temperature in the range of 13–25.4 °C. Due to the reduced HC time, the lower utilization factor and the consequently increased thermal losses, there is a sharp decline of the cooling efficiency with decreasing $T_{\mathrm{in,c}}$. For the present system and a low cooling inlet temperature of 13 °C, the cooling efficiency corresponds to $\eta_{\mathrm{c}} = 20\%$. In contrast to this, for $T_{\mathrm{in,c}} = 25.4$ °C a cooling efficiency of $\eta_{\mathrm{c}} = 96\%$ is reached, due to the lower temperature difference between ambient and cooling temperature. It can be concluded that the system is able to work in the entire range of varied cooling temperature. However, it is not reasonable to operate the present system (present plate reactors with Hydralloy® C2) under cooling temperatures below 13 °C, due to the low resulting cooling efficiency and average cooling power. A decrease of the cooling temperature has a stronger impact on both the system´s resulting HC time and its cooling efficiency compared to a rise of ambient temperature for same ΔT. Based on these extensive experimental investigations, it can be concluded that the limited pressure ratio (absorption pressure to required FC backpressure) in combination with the given constant mass flow rate to the FC imposes challenging conditions for the dynamics of the reactor.

Especially in harsher temperature boundaries, the temperature differences between the MH and the HTF become small, which results in a low hydrogen utilization factor.

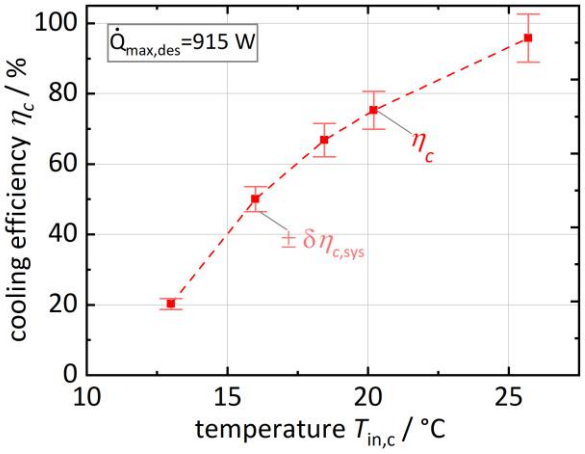

Figure 4-9: Cooling efficiency η_C with error bars for varied inlet temperatures of the cooling HTF loop.

Conclusions of the performance investigations

In this section, a detailed performance investigation for varying the key influencing parameters has been conducted. The experiments demonstrated that the present system is able to operate in the entire range of varied operating conditions. Nonetheless, the electrical FC power and operating temperature levels essentially influence the resulting cooling power output. The variation of electrical FC power in the range of 1.8–7.9 kW showed a maximum average cooling power of 807 W (SCP: 564 W kg_{MH}^{-1}) and a cooling efficiency of 59% at an electrical FC power of 7 kW. For same temperature differences, it was demonstrated that the present system is more sensitive towards a decrease of the cooling temperature compared to a rise of the ambient temperature. Due to the increased thermal losses and the reduced HC time, the operational limits of the first-of-its-kind system are at ambient temperatures above 43 °C and below cooling temperatures of 13 °C, each reaching cooling efficiencies below 32%. However, this decrease is considerably affected by the reactor design. Therefore, in the following section a numerical analysis of the applied plate reactor is conducted in order to investigate the potentials for improving the system performance.

5. Numerical analysis of the plate reactor

The MH reactor is the most important component of the open MHCS as it has a significant impact on the cooling power output as well as the cooling efficiency that can be reached in a real system. The present thesis applied the novel plate reactor concept, where the MH and HTF are arranged alternately with very small gaps. Single reactor measurements demonstrated that this concept is suitable for all high-performance systems [130] and a high cooling power could be obtained with the present open MHCS under moderate operating conditions. Nonetheless, the performance investigations showed that the cooling power output decreases in harsher operating conditions and with increased electrical FC power.

The numerical analysis of the reactor design is a promising method of identifying performance-limiting characteristics and to show possibilities for optimization as it has been done for different reactor concepts and various MH applications [123,135,136]. However, there are no available studies that carry out detailed numerical investigation of the promising plate reactor concept with regard to application in an open MHCS. Thereby, the focus is on avoiding heat and mass transfer limitations in the reaction bed, and at the same time the sensible reactor mass should be kept to the minimum required. When it comes to the layout of the system, it is very important to know the dynamic behaviour of the reactor, but this is difficult to predict as several physical phenomena have to be taken into account. Only if the hydrogen transport, chemical reaction and heat transport are accurately described, the cooling power of the open MHCS can be predicted well.

Therefore, in this section, the plate reactor concept is numerically investigated and optimizations for the open MHCS in view of increasing the performance are given. Initially, the model geometry and the equations of the numerical model are presented. Then, the model is validated with experimental data from the functional demonstration (see right of Figure 5-1) and the thermal losses that occur in a continuous system operation are discussed. Finally, recommendations for further optimization of the present reactor design are suggested and the expected performance of an improved system design under harsher operating conditions is derived. The contents of this section have already been published in [117,134].

Procedure of the numerical analysis

The applied procedure of the numerical analysis can be described as follows: Due to the equal profiles of the HCs in the two reactors, only a single cooling half-cycle (CHC) of one reactor is investigated for reasons of comparability and simplification. Therefore, according to the left part of Figure 5-1, the section of modelling is restricted to reactor R1 and the corresponding physical phenomena that occur during the endothermic desorption in the 1st HC for $t \leq 145$ s. The state of the previous regeneration half-cycle (RHC) is implemented as the initial condition

and, for the model validation, the characteristics of the HTF inlet as well as the hydrogen mass flow rate from the experiments are included. The numerical model predicts the temporal course of the reactor pressure, the HC time and the HTF outlet temperature, from which the reactor cooling power $\dot{Q}_{\mathrm{HTF,R1}}$ is derived. Since the operation optimization of the time-shifted valve switching and the interaction between the two HTF cycles is not included in the numerical model, the reactor cooling power has to be distinguished from the cooling power in the cooling HTF loop. In the Appendix F, a comparison of both profiles is given. Owing to this characteristic of the model, the values of the cooling power presented in this section each refer to $\dot{Q}_{\mathrm{HTF,R1}}$ (except in Chapter 5.4). However, this simplification has no effect on the validity of the given reactor optimization recommendations.

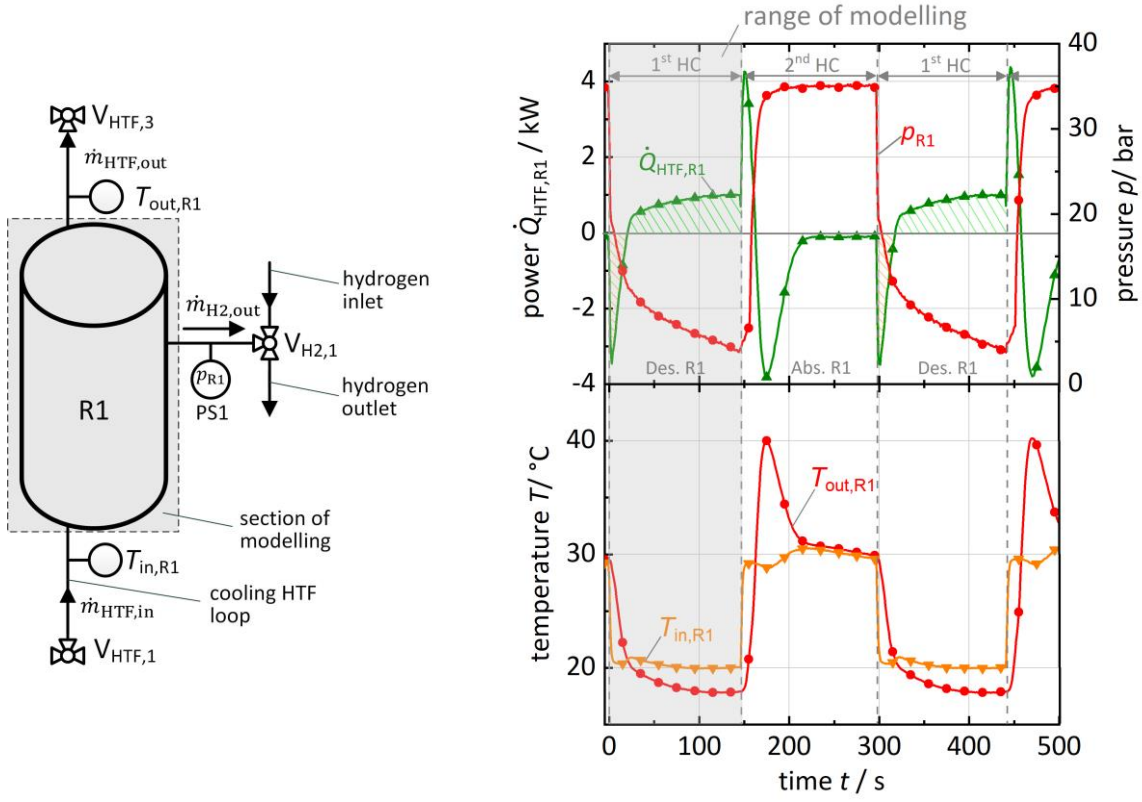

Figure 5-1: Illustration of the numerical procedure. Left: Section of modelling based on the experimental setup in Figure 2-6. Right: Range of modelling for a single desorption HC and results of the functional demonstration for the model validation.

5.1 Model formulation

Based on the description of the reactor design in Chapter 2.2, in this section, the resulting model geometry of the plate reactor concept is presented. For this geometry, a numerical model, including the equations for hydrogen transport, chemical reaction and heat transport is given.

5.1.1 Model geometry

Due to the alternating arrangement of MH/HTF and the uniform distribution of HTF and hydrogen, the applied plate reactor consists of a scalable and symmetrical structure. For this reason, the applied model geometry can be simplified and consists of three domains: (1) A half channel of MH, (2) a half channel of HTF and (3) the separating plate (thickness d_{SP}) in between. The corresponding shape of the rectangular model geometry is illustrated at the bottom of Figure 5-2.

In the half MH channel (thickness d_{MH}), hydrogen is released with a mass flow rate of $\dot{m}_{\mathrm{H2,out}}$ at the hydrogen outlet boundary $\overline{\mathrm{ab}}$ and the half HTF channel (thickness d_{HTF}) has an inlet and outlet for the HTF (mass flow rate $\dot{m}_{\mathrm{HTF}}$) on the right and left hand boundaries, respectively.

From the cross-sectional view of the reactor (Figure 5-2, top), it can be noted that the separating plates have a sinusoidal corrugation. Thus, in the MH channel the average distance for heat transfer varies along the length of the plate (which is l). In order to transfer this wavelike character to the simplified model geometry (geometry transformation), the average half channel height has to be included in the numerical model. For sinusoidal corrugation, d_{MH} is equivalent to the amplitude of the corrugation, which results in a very short average distance of heat transfer of $0.5 \cdot d_{\mathrm{MH}} = 0.44\ \mathrm{mm}$ for the present reactor design.

The performance of the complete reactor is obtained by scaling up the results from the simplified model geometry to the entire reactor with N_{MH} and $N_{\mathrm{HTF}} = N_{\mathrm{MH}} - 1$ channels, and $N_{\mathrm{SP}} = 2N_{\mathrm{MH}}$ steel plates. Thus, the transferred reactor cooling power $\dot{Q}_{\mathrm{HTF,R1}}$ is determined by the temperature difference between HTF channel inlet and outlet and the HTF flow rate of the entire reactor:

$$\dot{Q}_{\mathrm{HTF,R1}} = 2\,\dot{m}_{\mathrm{HTF}}\,c_{\mathrm{p,HTF}}(N_{\mathrm{MH}} - 1)(T_{\mathrm{in}} - T_{\mathrm{out}}) \tag{5-1}$$

Since the MH mass $m_{\mathrm{MH,R}}$ of the entire reactor is a function of the available half channel volume $V_{\mathrm{MH}} = bd_{\mathrm{MH}}l$, the porosity ε of the MH bed and the solid MH density ρ_{s} (calculated from the molar composition of Hydralloy® C2), the thermal performance of the reactor can be modified by varying the thickness d_{MH} of the MH bed (see Chapter 5.3):

$$m_{\mathrm{MH,R}} = 2N_{\mathrm{MH}}(1 - \varepsilon)\rho_{\mathrm{s}}V_{\mathrm{MH}} \tag{5-2}$$

where, for a given total reactor height h_{R}, the number of MH channels is

$$N_{\mathrm{MH}} = \frac{h_{\mathrm{R}} + d_{\mathrm{SP}}}{2(d_{\mathrm{MH}} + d_{\mathrm{SP}} + d_{\mathrm{HTF}})}. \tag{5-3}$$

The empty reactor weight m_{R} depends on the mass of the separating plates (volume $V_{\mathrm{SP}} = b d_{\mathrm{SP}} l$, density ρ_{SP}) and a mass m_{ep} that includes the weight of the end plates:

$$m_R = 2N_{MH}\, \rho_{SP} V_{SP} + m_{ep} \tag{5-4}$$

The total reactor mass $m_{\mathrm{t,}}$ is the sum of the total MH mass $m_{\mathrm{MH,R}}$ and the empty reactor mass m_{R}. Thus, from equations (5-2) and (5-4), the mass ratio k of passive reactor mass to active MH mass can be derived.

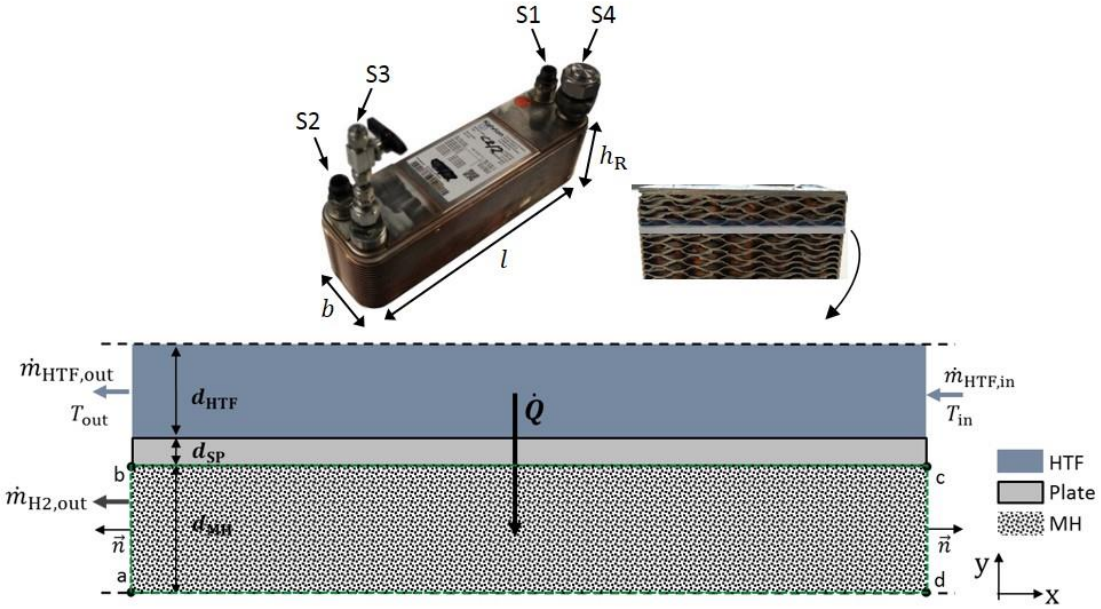

Figure 5-2: Top: Plate reactor (left) and cross-sectional view (right). Bottom: Model geometry consisting of a half MH/HTF channel and the separating plate.

5.1.2 Numerical model

Based on the previously described model geometry, in this section the required equations for the three domains MH bed, separating steel plate and HTF are presented. The following assumptions are made:

(1) Local thermal equilibrium between the hydrogen gas and the solid MH particles.
(2) The thermophysical properties of the MH bed do not vary with the hydrogen capacity and temperature; the impact of volume change during the phase change on the bulk properties is negligible.
(3) Hydrogen is assumed to be an ideal gas.
(4) The temperature variation in the steel plate and the HTF along the *y*-direction is negligible.
(5) Thermal radiation effects in the MH bed are negligible and no thermal losses occur to the surroundings.

Equations for the MH bed

Hydrogen mass balance

The density ρ_g of the hydrogen in the reactor changes due to the convective transport and the effective desorption rate of hydrogen in the MH bed (defined in [37,137] as $\frac{\partial \omega}{\partial t}$). Thus, the equation of continuity for the hydrogen gas is

$$\frac{\partial(\varepsilon \rho_g)}{\partial t} + \nabla(\rho_g \vec{u}) = -(1-\varepsilon)\rho_s \frac{\partial \omega}{\partial t} \tag{5-5}$$

where the gas density ρ_g is calculated from the ideal gas law:

$$\rho_g = \frac{p M_{H2}}{RT} \tag{5-6}$$

During the desorption a pressure drop occurs in the porous MH powder bed. This pressure gradient ∇p is related to u according to Darcy´s law:

$$\vec{u} = -\frac{\kappa}{\mu}\nabla p \tag{5-7}$$

The permeability $\kappa = 1 \cdot 10^{-12}\ \mathrm{m}^2$ [138] used for this numerical analysis is in good agreement with the Carman–Kozeny equation simplified for spherical particles [139].

Reaction kinetics of MH

The effective reaction rate is a function of the temperature T of the MH bed, the distance from thermodynamic equilibrium, and the transformed fraction. Based on equations (1-6) and (1-7), an expression for the effective desorption reaction rate is given by [37,137]:

$$\frac{\partial \omega}{\partial t} = -K_0 \exp\left(\frac{-E_A}{k_B T}\right)\left(\frac{p - p_{eq,des}}{p_{eq,des}}\right)(\omega_{max} - \omega) \tag{5-8}$$

The Arrhenius parameter K_0 and the activation energy E_A are calculated from the experimental desorption kinetics of Hydralloy® C2 and the Arrhenius plot presented in [37]. For this calculation, the values for the kinetic constant at 20 °C and 10 °C are 0.67 s^{-1} and 0.43 s^{-1}. The desorption equilibrium pressure $p_{eq,des}$ is determined by the polynomial fit of the PCIs of Hydralloy® C2, which was previously described in Chapter 2.1 (see equation (2-4)). The maximum hydrogen storage capacity ω_{max} for the desorption HC results from the hydrogen capacity w_{RHC} of the prior regeneration HC and k_B corresponds to the Boltzmann constant.

Energy equation of MH

The temperature change in the MH is caused by the heat transfer in/through the bed and the endothermic desorption (heat sink) due to the chemical reaction. Thus, the energy equation is:

$$\left[(1-\varepsilon)\rho_{\mathrm{s}}c_{\mathrm{p,s}}+\varepsilon\rho_{\mathrm{g}}c_{\mathrm{p,g}}\right]\frac{\partial T}{\partial t}+\nabla(-\lambda_{\mathrm{eff}}\nabla T)=\frac{(1-\varepsilon)\rho_{\mathrm{s}}\Delta H_{\mathrm{des}}}{M_{\mathrm{H2}}}\frac{\partial\omega}{\partial t} \qquad (5\text{-}9)$$

In the above expression $c_{\mathrm{p,s}}$, $c_{\mathrm{p,g}}$ are the specific heat capacity of the solid MH and of the hydrogen, and λ_{eff} is the effective heat conductivity of the MH bed.

Equations for the separating steel plate and the HTF

For the energy balances of the separating steel plate and the HTF, the convective heat transfer of the HTF (heat transfer coefficient α_{HTF}), the thermal conduction in the separating steel plate (thermal conductivity λ_{SP}) and the convective heat transfer to the MH bed (heat transfer coefficient α_{MH}) are taken into account. Since the thickness of the separating plate ($d_{\mathrm{SP}}=0.4\ \mathrm{mm}$) and the half HTF channel ($d_{\mathrm{HTF}}=0.88\ \mathrm{mm}$) is very small compared to the length, the variation along the *y*-axis of the temperature T_{SP} of the steel and the temperature T_{HTF} of the HTF is neglected. Based on [140], the energy equations of the separating steel plate along the *x*-direction is:

$$\rho_{\mathrm{SP,m}}c_{\mathrm{p,SP}}bd_{\mathrm{SP}}l\frac{\partial T_{\mathrm{SP}}}{\partial t}+\nabla(-\lambda_{\mathrm{SP}}bd_{\mathrm{SP}}l\nabla T)=bl\left(\alpha_{\mathrm{MH}}(T-T_{\mathrm{SP}})-\alpha_{\mathrm{HTF}}(T_{\mathrm{SP}}-T_{\mathrm{HTF}})\right) \qquad (5\text{-}10)$$

Since the mass of the end plates is not considered in the model geometry, a modified density of the plates $\rho_{\mathrm{SP,m}}$ is implemented:

$$\rho_{\mathrm{SP,m}}=\frac{m_{\mathrm{R}}}{2N_{\mathrm{MH}}bd_{\mathrm{SP}}l} \qquad (5\text{-}11)$$

Neglecting the variation of T_{HTF} along the *y*-axis leads to following energy equation of the HTF:

$$\rho_{\mathrm{HTF}}c_{\mathrm{p,HTF}}bd_{\mathrm{HTF}}l\frac{\partial T_{\mathrm{HTF}}}{\partial t}+\dot{m}_{\mathrm{HTF}}c_{\mathrm{p,HTF}}l\frac{\partial T_{\mathrm{HTF}}}{\partial x}=\alpha_{\mathrm{HTF}}bl(T_{\mathrm{SP}}-T_{\mathrm{HTF}}) \qquad (5\text{-}12)$$

As the HTF is equally distributed to all N_{HTF} HTF channels, the mass flow rate in the negative *x*-direction is

$$\dot{m}_{\mathrm{HTF}}=-\frac{\dot{V}_{\mathrm{HTF,R}}}{2(N_{\mathrm{MeH}}-1)}\rho_{\mathrm{HTF}} \qquad (5\text{-}13)$$

The convective heat transfer coefficient α_{HTF} used in equations (5-10) and (5-13) is given by:

$$\alpha_{\mathrm{HTF}}=\frac{Nu\lambda_{\mathrm{HTF}}}{d_{\mathrm{h}}} \qquad (5\text{-}14)$$

Various correlations are available for the calculation of the Nusselt number Nu [141–143] in corrugated plates. For the present reactor, the correlation of Martin [144] is in best accordance with the design values given by the manufacturer. The corresponding equations are shown in the Appendix G and the physical properties of the HTF are evaluated for an average temperature of $T_{\mathrm{HTF,avg}} = 0.5 \cdot (T_{\mathrm{SP}} + \mathrm{T_{HTF}})$. Due to the neglect of temperature variation along the y-axis, the model geometry is reduced to the MH domain with the corner points abcd (cf. Figure 5-2, dashed green line).

Initial and boundary conditions

For modelling the desorption HC, the corresponding state of regeneration during the previous HC is implemented as the initial condition. Thus, initially, the MH is in a hydrogenated state with a uniform hydrogen capacity ω_{RHC} that corresponds to an absorption pressure of p_{RHC}. A uniform initial regeneration temperature T_{RHC} is assumed for the MH bed, the separating plate and the HTF. Hence, at $t = 0$, the initial conditions are

$$T_{\mathrm{MH}}(x,y) = T_{\mathrm{SP}}(x,y) = T_{\mathrm{HTF}}(x,y) = T_{\mathrm{RHC}},$$
$$p(x,y) = p_{\mathrm{RHC}} \text{ and } \omega(x,y) = \omega_{\mathrm{RHC}}. \tag{5-15}$$

Then, the cooling HC is initiated by releasing hydrogen at a mass flow rate of $\dot{m}_{\mathrm{H2,out}}$ which is dependent on the electrical FC power P_{el}, the FC efficiency η_{FC} and the LHV of the hydrogen H_{H2}. The required heat of formation for the desorption is supplied from the HTF and consequently a cooling power is generated. As the MH pressure decreases during the desorption and the FC requires a minimum operating backpressure p_{FC}, a pressure-controlled switching criterion is defined. When, at the hydrogen outlet boundary $\overline{\mathrm{ab}}$, the pressure $p_{\overline{\mathrm{ab}}}$ reaches the reactor switching pressure $p_{\mathrm{R,sw}}$, the cooling HC is completed and the previously absorbing reactor starts feeding the FC. Since a pressure difference between the reactor pressure and the FC inlet pressure was observed during the experiments (e.g. $\Delta p = 1.8\ \mathrm{bar}$ under reference conditions), $p_{\mathrm{R,sw}}$ is adapted to the experimental value of the reactor pressure at the point of switching. For $t > 0$, the boundary conditions (cf. Figure 5-2) are summarized as follows:

Constant hydrogen mass flow rate $\dot{m}_{\mathrm{H2,out}}$ at the hydrogen outlet boundary $\overline{\mathrm{ab}}$ in the negative x-direction:

$$\dot{m}_{\mathrm{H2,out}} = -\frac{P_{\mathrm{el}}}{2\,\eta_{\mathrm{FC}} H_{\mathrm{H2}} N_{\mathrm{MH}}} \text{ (for } p_{\overline{\mathrm{ab}}} \geq p_{\mathrm{R,sw}}) \tag{5-16}$$

$$\dot{m}_{\mathrm{H2,out}} = 0 \text{ (for } p_{\overline{\mathrm{ab}}} < p_{\mathrm{R,sw}}) \tag{5-17}$$

The boundaries $\overline{\mathrm{ad}}, \overline{\mathrm{bc}}$ and $\overline{\mathrm{cd}}$ are assumed to be impermeable reactor walls ($\frac{\partial p}{\partial \vec{n}} = 0$). While the boundaries $\overline{\mathrm{ab}}, \overline{\mathrm{ad}}$ and $\overline{\mathrm{cd}}$ are thermally insulated ($\frac{\partial T}{\partial \vec{n}} = 0$), the heat flow at the interface between the separating plate and the MH bed (boundary $\overline{\mathrm{bc}}$) is given by:

$$\dot{Q} = \alpha_{\mathrm{MH}} bl(\mathrm{T_{SP}} - \mathrm{T}) \tag{5-18}$$

The mathematical model presented above was implemented in the commercial finite element software COMSOL Multiphysics® (version 5.3), which solves the presented conservation equations in differential form. Based on the initial conditions of the regeneration, the numerical model is applied to the presented model geometry. The cooling power of the entire reactor geometry is obtained by scaling up the results according to equation (5-1). The corresponding simulation parameters are summarized in Table 5-1.

Table 5-1: Simulation parameters and material properties of C2.

Parameter	Symbol	Value
Material properties of Hydralloy® C2		
Activation energy for desorption, J	E_a	$5.083 \cdot 10^{-20}$ [based on[37]]
Arrhenius coefficient for desorption, s^{-1}	K_0	$1.904 \cdot 10^5$ [based on [37]]
Boltzmann constant, $J\ K^{-1}$	k_B	$1.38065 \cdot 10^{-23}$
Density of MH, $kg\ m^{-3}$	ρ_s	6375.3
Enthalpy of absorption, $J\ mol^{-1}$	ΔH_{abs}	$17.8 \cdot 10^3$
Enthalpy of desorption, $J\ mol^{-1}$	ΔH_{des}	$21.9 \cdot 10^3$
Entropy of absorption, $J\ mol^{-1}\ K^{-1}$	ΔS_{abs}	83.9
Entropy of desorption, $J\ mol^{-1}\ K^{-1}$	ΔS_{des}	91.8
Heat conductivity of MH, $W\ m^{-1}\ K^{-1}$	λ	1.0 [145]
Heat transfer coefficient, $W\ m^{-2}\ K^{-1}$	α_{MH}	$1 \cdot 10^4$ [146]
Hydrogen capacity of the regeneration, wt.%	ω_{RHC}	1.75 (ref. conditions)
Permeability, m^2	κ	$1 \cdot 10^{-12}$ [138]
Porosity, -	ε	0.68 (ref. conditions)
Specific heat capacity of MH, $J\ kg^{-1}\ K^{-1}$	$c_{p,s}$	500
Hydrogen gas:		
Ambient pressure, Pa	p_0	$1.013 \cdot 10^5$
Dynamic viscosity of hydrogen, Pa s	μ	$10^{-5} \cdot 9.05 \cdot (T/293)^{0.68}$ [123]
Lower heating value of hydrogen, $J\ kg^{-1}$	ΔH_{H2}	$1.2 \cdot 10^8$
Molar weight of hydrogen, $kg\ mol^{-1}$	M_{H2}	$2.016 \cdot 10^{-3}$
Specific heat capacity of hydrogen, $J\ kg^{-1}\ K^{-1}$	$c_{p,g}$	$1.4304 \cdot 10^4$
Separating plate (SP)		
Density of plate, $kg\ m^{-3}$	ρ_{SP}	$8 \cdot 10^3$
Heat conductivity of plate, $W\ m^{-1}\ K^{-1}$	λ_{SP}	15
Initial pressure, Pa	p_{RHC}	$23.88 \cdot 10^5$ (ref. conditions)
Reactor switching pressure , Pa	$p_{R,sw}$	$6.1 \cdot 10^5$ (ref. conditions)
Specific heat capacity of plate, $J\ kg^{-1}\ K^{-1}$	$c_{p,SP}$	500
Heat transfer fluid (HTF)		
Density of HTF, $kg\ m^{-3}$	ρ_{HTF}	20 °C: 1072 (temp-dep.)
Heat conductivity of HTF, $W\ m^{-1}\ K^{-1}$	λ_{HTF}	20 °C: 0.392 (temp-dep.)
HTF inlet temperature, K	$T_{in,HTF}$	20 °C (ref. conditions)
Kinematic viscosity of HTF, $m^2 s^{-1}$	γ_{HTF}	20 °C: $4 \cdot 10^{-6}$ (temp-dep.)
Specific heat capacity of HTF, $J\ kg^{-1}\ K^{-1}$	$c_{p,HTF}$	20 °C: 3312 (temp-dep.)
Volume flow rate of HTF, $m^3\ s^{-1}$	$\dot{V}_{HTF,R}$	$1.33 \cdot 10^{-4}$
Reactor and model geometry (see Chapter 2.2)		
Channel length, m	l	0.279
Channel width , m	b	$8.059 \cdot 10^{-2}$
Corrugation inclination angle, rad	β	0.109
Corrugation wavelength, m	λ_a	$1.24 \cdot 10^{-2}$
Electrical FC power, W	P_{el}	$4.982 \cdot 10^3$ (ref. conditions)
FC Efficiency, -	η	0.51 (ref. conditions)
Mass of end plates and connections, kg	m_{ep}	2.108
Number of HTF channels, -	N_{HTF}	17 (ref. conditions)
Number of MH channels,-	N_{MH}	18 (ref. conditions)
Number of separating steel plates, -	N_{SP}	36 (ref. conditions)
Reactor (inner) height, m	h_R	$7.6 \cdot 10^{-2}$
Thickness of half HTF channel, m	d_{HTF}	$8.8 \cdot 10^{-4}$
Thickness of half MH channel, m	d_{MH}	$8.8 \cdot 10^{-4}$ (ref. conditions)
Thickness of steel plate, m	d_{SP}	$4 \cdot 10^{-4}$

5.2 Model validation and evaluation of thermal losses

In this section, the previously presented numerical model is compared with the reference experiment of the functional demonstration (1st HC of reactor R1 for $t \leq 145\,\mathrm{s}$, see Figure 5-1). In order to show that the model is valid for a wide range of boundary conditions, the validation is extended to different hydrogen mass flow rates (electrical FC powers) and cooling inlet temperatures, which were investigated in the system´s performance investigations. Since the thermal losses have a considerable influence on the usable cooling power of the system, these losses are also evaluated and discussed in detail in the following.

Model validation

In order to transfer the continuous system operation of the functional demonstration under reference conditions to the presented numerical reactor model, the regeneration HC is implemented with the following initial conditions: The absorption was conducted with an absorption pressure of $p_{\mathrm{RHC}} = 35\,\mathrm{bar}$ and an HTF inlet temperature of $T_{\mathrm{in,RHC}} = 30.1\,°\mathrm{C}$, consequently the initial hydrogen capacity is $\omega_{\mathrm{RHC}} = 1.75\,\mathrm{wt.\,\%}$ (cf. Figure 2-3). To consider the free volume expansion to the FC connecting pipe, the experimental pressure value after $t = 1\,\mathrm{s}$ is implemented as initial pressure in the reactor model. During the desorption, the reactor released an average hydrogen mass flow rate of $\dot{m}_{\mathrm{H2,out}} = 4.86\,\mathrm{g\,min^{-1}}$ to the continuously operating FC ($P_{\mathrm{el}} = 4.98\,\mathrm{kW}$, $\eta_{\mathrm{FC}} = 0.51$), while the HTF inlet temperature (flow rate $\dot{V}_{\mathrm{HTF,R}} = 7.98\,\mathrm{l\,min^{-1}}$) was adjusted to $T_{\mathrm{in}} = 20.2\,°\mathrm{C}$. For a precise model prediction, the profiles of HTF inlet temperature and flow rate are implemented from experimental data and the corresponding reactor switching pressure at the hydrogen outlet boundary is set to $p_{\mathrm{R,sw}} = 6.1\,\mathrm{bar}$.

Comparing the experimental results (dashed line with symbols) with the numerical model (solid line) in Figure 5-3, based on the temporal course of the HTF reactor outlet temperature T_{out}, it can be noted that there is a good agreement between experiment and simulation. The initial HIP as well as the subsequent CP in the profiles of T_{out} and $\dot{Q}_{\mathrm{HTF,R1}}$ are correctly predicted. The mean value deviation of the average reactor cooling power $\bar{\dot{Q}}_{\mathrm{HTF,R1}} = {t_{\mathrm{HC}}}^{-1} \int_0^{t_{\mathrm{HC}}} \dot{Q}_{\mathrm{HTF,R1}}(t)dt$ between the numerical model and the experiment is below 16%.

In the pressure course (top of Figure 5-3), there is at the beginning a clear deviation between experiment and simulation that becomes smaller during the course of the experiment. This discrepancy is probably caused by the deviation of the polynomial fitting method from the experimental PCIs for a high hydrogen capacity in the β-phase (cf. Figure 2-3). A further factor might be that the pressure sensor in the experiment is not directly integrated at the hydrogen outlet boundary $\overline{\mathrm{ab}}$, since there was a filter candle and a hydrogen two-way valve in between

as can be seen in Figure 2-7. These components as well as the detailed void volume in between are not implemented in the present model. As the PCIs model accurately predicts the plateau region (for instance, for a hydrogen capacity of $\omega = 0.75$ wt. % the deviation is 2.1%), with reduced hydrogen capacity the discrepancy in the temporal course of pressure decreases. Thus, the presented model predicts the duration of the cooling HC (HC time $t_{\mathrm{HC}} = 145$ s) very well, which is derived from the switching criterion of $p_{\overline{\mathrm{ab}}} < 6.1$ bar.

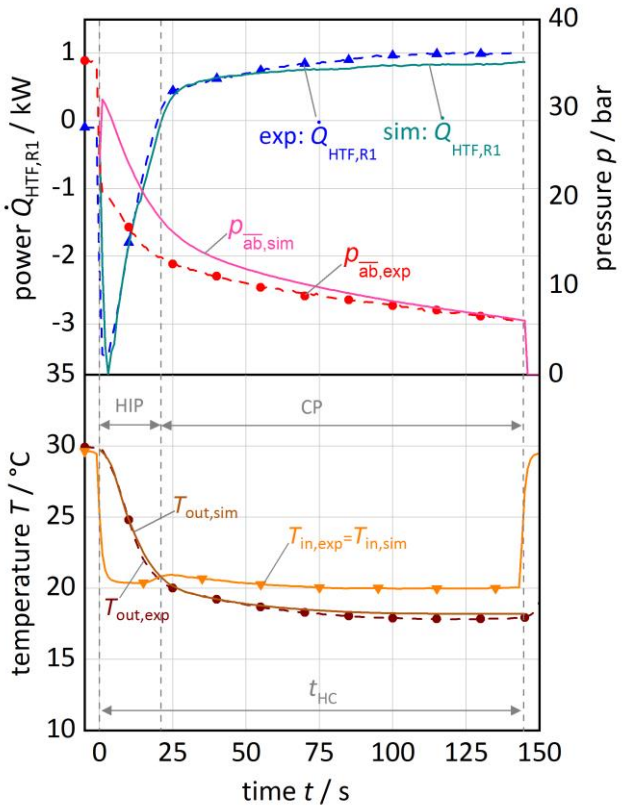

Figure 5-3: Comparison of the numerical and experimental results under reference conditions of the functional demonstration.

Due to the good agreement under reference conditions, the model is also validated for a variation of the inlet temperatures of the HTF cooling loop ($T_{\mathrm{in}} = 13 - 25$ °C) and electrical FC power ($P_{\mathrm{el}} = 4 - 6$ kW) which can be seen in Figure 5-4. Except from T_{in} and P_{el}, reference conditions are applied.

The experiments of the performance investigations demonstrated that for growing cooling inlet temperatures the average cooling power increases, since thermal losses in the HIP phase are reduced and the CP is extended as an increased $\Delta\omega_{\mathrm{max}}$ is available. The model (see Figure 5-4 left) correctly predicts the HC time as well as the experimental evolution of the HTF power, since for 13 °C and 25 °C the mean value deviation of $\bar{\dot{Q}}_{\mathrm{HTF,R1}}$ between the model and the experiment is below 10%. For 13 °C the HC time is slightly underestimated, and for 25 °C, it is overestimated, as in the plateau region a low pressure deviation results in a huge change in t_{HC}. The small deviation of the maximum cooling power at the end of the CP is probably caused

by the uncertainty of the experimental measurement equipment or the accuracy of the enthalpy of desorption, which is implemented in the numerical model.

From the experiments with varied electrical FC power, it was demonstrated that for increasing hydrogen mass flow rates the maximum cooling power increases, while the HC time t_{HC} is reduced and vice versa. The model (Figure 5-4 right) correctly predicts both effects, while the duration of the HC is overestimated for low FC powers and underrated for high FC powers. The mean value deviation of the average reactor cooling power is below 4% for an electrical FC power of 4 kW and below 25% for an electrical FC power of $6\ \mathrm{kW}$.

It can be concluded that the simulation results are in good agreement with the experiments for varied cooling inlet temperatures and electrical loads of the FC. As the temporal course of the reactor cooling power as well as the HC time is accurately described, the model can be used for the following discussion of thermal losses and the given reactor optimization recommendations in Chapter 5.3.

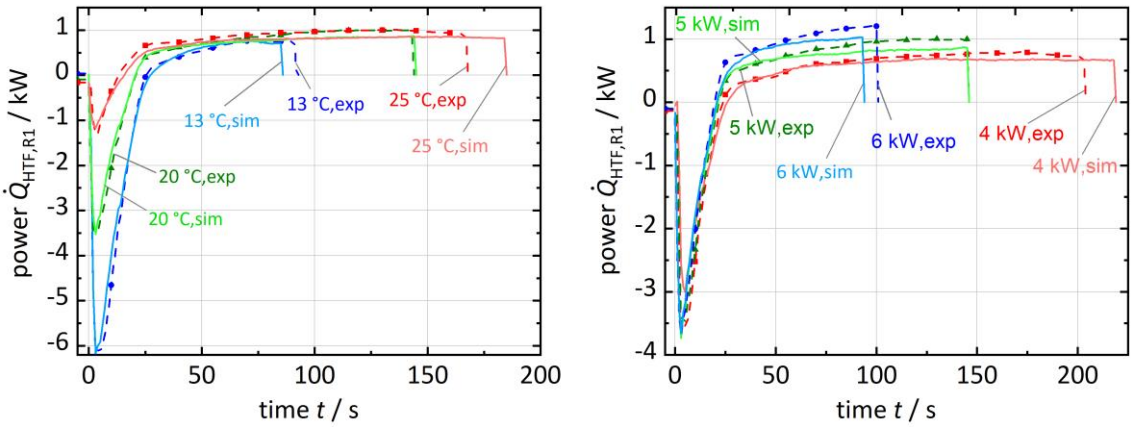

Figure 5-4: Comparison of the numerical and experimental results for a variation of cooling inlet temperature (left) and electrical FC power (right).

Discussion of thermal losses

As shown in the experimental characterization before, in the continuous operation of the system, there are fluid exchange losses and sensible heat losses that have a significant impact on the effective cooling power and, therefore, are crucial for the application of the open MHCS. Due to the change of operation temperature between every HC, the sensible mass of the reactor is very important. In order to simplify a comparison of different reactor designs, the mass ratio k according to equation (1-9) can be applied. In Figure 5-5 for two different mass ratios k, the thermal losses are evaluated under reference conditions, and compared to the maximum obtainable cooling power $\dot{Q}_{\mathrm{max,des}}$ corresponding to equation (1-10).

The orange line, which displays the maximum obtainable power, is obtained when the heat of formation for the desorption is completely supplied from the HTF and no fluid exchange losses or sensible heat losses occur (no switching between the HCs). For the average hydrogen mass

flow rate of 4.86 g min^{-1} at reference conditions and the desorption reaction enthalpy of Hydralloy® C2, the maximum obtainable power reaches a constant value of $\dot{Q}_{\mathrm{max,des}} = 889$ W for an FC efficiency of $\eta_{\mathrm{FC}} = 0.51$.

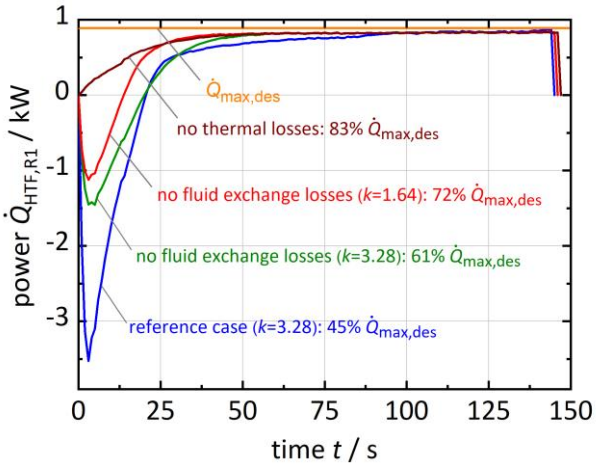

Figure 5-5: Evaluation of sensible heat losses and fluid exchange losses, and comparison to the maximum obtainable cooling power $\dot{Q}_{\mathrm{max,des}}$.

The brown line shows the HTF power for the present reactor design assuming that the regeneration temperature level is equivalent to the cooling temperature (initial condition: $T_{\mathrm{RHC}} = T_{\mathrm{CHC}}$) and therefore no thermal losses occur. Due to heat and mass transport and the real behaviour of the reactor, in the first seconds the cooling power increases slowly compared to the maximum obtainable power. Hence, the average maximum cooling power is reduced to $\bar{\dot{Q}}_{\mathrm{HTF,R1}} = 737$ W, which is $83\% \cdot \dot{Q}_{\mathrm{max,des}}$. Taking into account fluid exchange losses and sensible heat losses under reference conditions and the present reactor design (blue line, mass ratio $k = 3.28$), the average reactor cooling power decreases to $\bar{\dot{Q}}_{\mathrm{HTF,R1}} = 390$ W. This shows that the thermal losses that occur in the continuous operation of the system can reduce the attainable average cooling power by more than 50% compared to $\dot{Q}_{\mathrm{max,des}}$.

When fluid exchange losses are neglected and only sensible heat losses are considered (green line, initial condition: $T_{\mathrm{HTF,t=0}}(\mathrm{x,y}) = T_{\mathrm{HTF,in}}$), an average cooling power of 545 W can be realized. Thus, $\bar{\dot{Q}}_{\mathrm{HTF,R1}}$ can be increased by almost 40% compared to the reference conditions. The red line displays the HTF power when the reactor mass is reduced by 50% (reduced density of the plate) and a mass ratio $k = 1.64$ of passive reactor mass to active MH mass is realized (constant MH mass). In this case, the HIP is further decreased and the resulting average cooling power reaches $72\% \cdot \dot{Q}_{\mathrm{max,des}}$, while fluid exchange losses are also neglected.

From the temporal course of the reactor cooling power, it can be generally noted that varying the thermal losses and mass ratios has a significant impact on the heat input in the HIP, while the HC time and the maximum cooling power are unaffected by this variation. Therefore, the first recommendation for optimizing the reactor, it is crucial to decrease the mass ratio k, for

instance by reducing the reactor mass. Additionally, appropriate measures have to be adopted and implemented in the system in order to avoid fluid exchange losses. The operation optimization of time-shifted switching of the reactor outlet valves can be applied for this purpose.

5.3 Reactor optimization recommendations

In view of the high volumetric and gravimetric power density needed for an automotive application of the open MHCS, in this section recommendations for the design of an optimized reactor will be proposed based on the reference conditions. The parameters and effects under investigation are the following:

- Thickness of the MH bed.
- Reduced distance for the hydrogen gas transport.
- Reduced porosity and decreased switching pressure.

Effect of varying the thickness of the MH bed

In order to avoid heat transfer limitations in the MH channel, the present plate reactor has a very small average heat transport distance of $0.5 \cdot d_{\mathrm{MH}}$. However, it might be reasonable to increase the channel thickness since with growing d_{MH} a larger volume for packing the MH is available and the mass ratio k is improved. Thus, the duration of the HC time might be extended, which results in an increased average cooling power and a reduced impact of the thermal losses.

In Figure 5-6, the total MH mass, the empty reactor mass and the corresponding total reactor mass are given for varied half channel thicknesses (see equations (5-2) and (5-4)). In all cases, the inner height of the reactor is constant ($h_{\mathrm{R}} = 7.6\ \mathrm{cm}$) and the thickness of the HTF channel remains unchanged regarding the present reactor design. It can be seen that for growing d_{MH}, the MH mass $m_{\mathrm{MH,R}}$ is increased as the number of MH channels and separating steel plates with $N_{\mathrm{SP}} = 2N_{\mathrm{MH}}$ are reduced and therefore a larger volume for packing the MH is available. At the same time, for an increased channel thickness, the reactor mass is reduced and the mass ratio k can be improved. For instance, for $d_{\mathrm{MH}} = 5.2\ \mathrm{mm}$, $m_{\mathrm{MH,R}}$ is almost doubled and the mass ratio significantly reduced to $k = 1.01$, compared to the present reactor design.

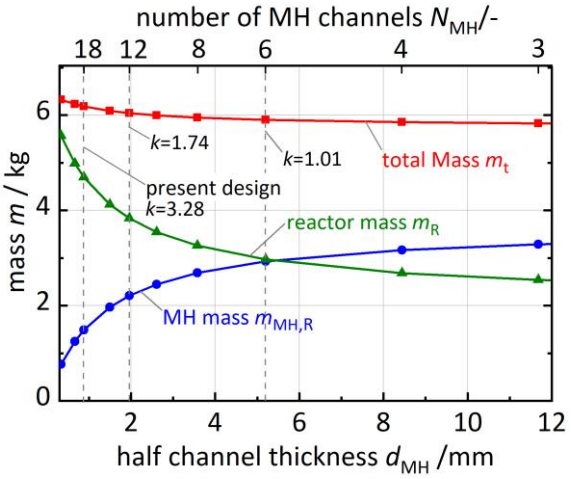

Figure 5-6: Total MH mass, empty reactor mass and total reactor mass for various half channel thicknesses and numbers of MH channels.

However, there is a trade-off as the heat transfer in the MH channel is affected by a variation of the channel thickness: When the increased thickness d_{MH} is too large, the supplied heat flow is lower than the required heat flux for the desorption of hydrogen, so the MH cools down to lower equilibrium temperatures. Thus, for the same switching pressure and a reduced MH equilibrium temperature, the utilization of the theoretically usable hydrogen capacity $\Delta\omega_{\max}$ is decreased. The hydrogen utilization factor F according to equation (2-1) is employed in the following to quantify this MH material utilization.

Figure 5-7 shows the reactor cooling power and average MH temperature as a function of the half channel thickness d_{MH}. For a very small thickness of 0.34 mm, heat transfer limitations in the MH bed are avoided, as in the CP the average MH temperature remains constant during the endothermic desorption. However, as the total MH mass is reduced to almost half of the reference conditions, the switching pressure is already reached after $t_{\mathrm{HC}} = 51$ s. In contrast, for $d_{\mathrm{MH}} = 8.44$ mm and a total MH mass of $m_{\mathrm{MH}} = 3.17$ kg, the average MH temperature continuously decreases (minimum average MH temperature $T_{\mathrm{MH,avg}} = 2.3$ °C) due to the endothermic reaction. Heat transfer limitations result in a slow increase of cooling power in the CP and in a low hydrogen utilization factor of $F = 0.26$ (reference conditions: $F = 0.63$).

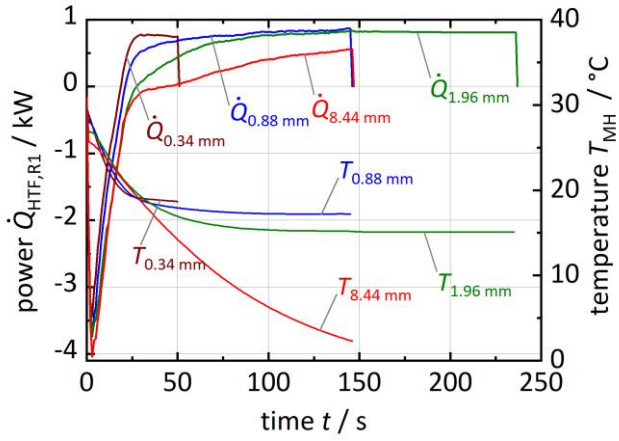

Figure 5-7: Temporal course of the reactor cooling power and average MH temperature as the half MH channel thickness varies.

Consequently, there is a conflict between avoiding heat transfer limitations (small bed thickness) and increasing the available MH/hydrogen capacity (large bed thickness) and, in terms of maximum average cooling power, there exists an optimum thickness for the MH bed.

The calculated average reactor cooling power $\bar{\dot{Q}}_{\mathrm{HTF,R1}}$ and the corresponding HC time t_{HC} as a function of d_{MH} are summarized in Figure 5-8. The behaviour of the average HTF power can be separated into two sections. If $d_{\mathrm{MH}} \leq 0.45\ \mathrm{mm}$ or $d_{\mathrm{MH}} \geq 7.3\ \mathrm{mm}$, the values for $\bar{\dot{Q}}_{\mathrm{HTF,R1}}$ are below zero. Thus, thermal losses due to switching from the regeneration to the cooling HC dominate and as a result, no actual cooling effect is obtained. For the range $0.45\ \mathrm{mm} < d_{\mathrm{MH}} < 7.3\ \mathrm{mm}$, a cooling effect is generated that has an optimum for $d_{\mathrm{MH}} = 1.96\ \mathrm{mm}$ ($N_{\mathrm{MH}} = 12$). The commercially available and currently used reactor design with symmetric channels (HTF and MH channels are identical) was close to this optimum of $\bar{\dot{Q}}_{\mathrm{HTF,R1}} = 432\ \mathrm{W}$.

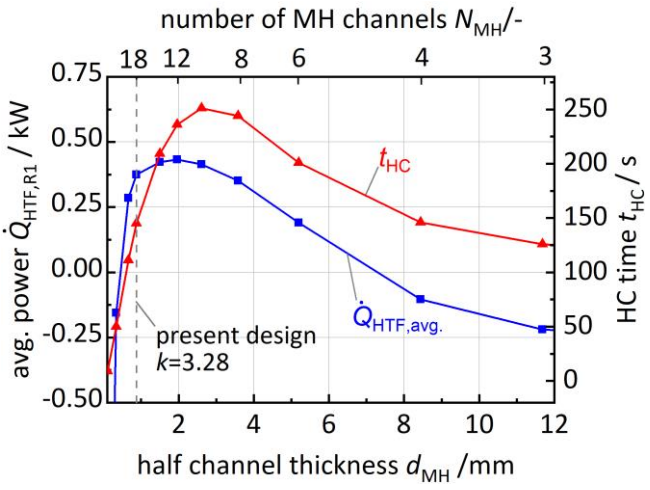

Figure 5-8: Average reactor cooling power and duration of the HC as functions of the half MH channel thickness.

However, an asymmetric reactor design with a slightly increased MH channel thickness and a reduced HTF channel thickness for low fluid exchange losses is generally recommended. Furthermore, an attractive option for improving the mass ratio k might be the employment of MH composites which have an increased thermal conductivity, in the range of 10–15 W m^{-1} K^{-1} [147]. In this way, the thickness of the MH channel and the available MH capacity can be enhanced without increasing the heat transfer limitations in the MH bed.

Effect of reduced distance for the hydrogen gas transport

Next to varying the MH bed thickness, another possibility to optimize the present reactor is to reduce the distance for the hydrogen gas transport. From the temporal course of the pressure at the hydrogen outlet boundary $p_{\overline{\mathrm{ab}},\mathrm{ref}}$ and the average MH bed pressure $p_{\mathrm{avg,ref}}$ in Figure 5-9, it can be seen that the present reactor shows a pressure drop in the MH bed. For instance, at the HC time $t_{\mathrm{HC}} = 145$ s when the switching pressure is reached, the pressure difference is $p_{\mathrm{avg,ref}} - p_{\overline{\mathrm{ab}},\mathrm{ref}} = 3.4$ bar. As the pressure at the hydrogen outlet boundary $\overline{\mathrm{ab}}$ defines the HC time, no more hydrogen can be supplied to the FC although the average bed pressure is above the switching criterion. The resulting hydrogen utilization factor of $F = 0.63$ shows that the available MH capacity is not fully exploited.

In order to reduce this pressure drop and to enhance the average cooling power, next to the existing supply, hydrogen can be additionally provided at the boundary $\overline{\mathrm{cd}}$. Hence, the average distance for the hydrogen gas transport in the MH bed is reduced and a reactor with a two-sided (tsd) hydrogen inlet/outlet is realized. According to Figure 5-9, for this reactor the pressure drop in the MH bed can be clearly decreased.

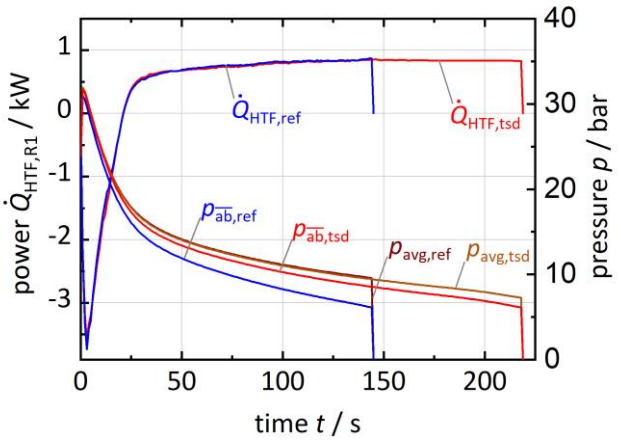

Figure 5-9: Temporal course of the reactor cooling power and hydrogen pressure for the present reactor (reference conditions) and with the implementation of a reduced distance for the hydrogen gas transport.

At the switching time on reference conditions, the difference between the average bed pressure $p_{\overline{\mathrm{ab}},\mathrm{tsd}}$ and the pressure at hydrogen outlet boundary $p_{\overline{\mathrm{ab}},\mathrm{tsd}}$ is reduced to

$\Delta p = 1.15\,\mathrm{bar}$ and, therefore, the CP is extended to $t_{\mathrm{HC,tsd}} = 219\,\mathrm{s}$. This results in an increased utilization of the available MH capacity (hydrogen utilization factor $F = 0.89$) and the average reactor cooling power is enhanced by 40% compared to the reference conditions.

Effects of reduced porosity and decreased switching pressure

As previously described, with the aim of obtaining a high cooling power of the reactor, a maximum duration of the CP is required. For a given reactor geometry, this can be reached by either reducing the porosity or decreasing the switching pressure. In the following, the effect of these two alternatives on the duration of the HC as well as the resulting average reactor cooling power will be presented.

The absorption of hydrogen is accompanied by a swelling effect that imposes pressures on the reactor wall of up to 85 bar [69]. Thus, for the first realization of the plate reactor a high porosity of $\varepsilon = 68\%$ was implemented assuring the mechanical stability. However, in the literature on Hydralloy® C5, an alloy with a similar composition to that of Hydralloy® C2, a porosity of $\varepsilon \leq 50\%$ was employed [148]. Hence, a reduction of porosity in the MH bed of the plate reactor could be feasible.

By decreasing the porosity from 68% to 50%, equation (5-2) implies that the total mass of the MH would be increased by 56%. As more MH capacity is available to supply hydrogen to the FC, the mass ratio can be improved and the CP is extended. For this first design recommendations, it is assumed that the permeability and effective heat conductivity of the MH bed are constant, and the heat and mass transport remain unaffected from the reduced porosity. According to the temporal course of the reactor cooling power and pressure (see Figure 5-10), for a porosity of 50% the duration of the HC is increased by $\Delta t_{\mathrm{HC}} = 75\,\mathrm{s}$ and, as a result, the average reactor cooling power is increased by 33% compared to the reference conditions. For a porosity of 60%, $\bar{\dot{Q}}_{\mathrm{HTF,R1}}$ is still enhanced by 15%, which shows the potential for improving the reactor performance by reducing the porosity of the bed.

Due to the required backpressure of the FC and the pressure difference at the hydrogen outlet section of the experimental setup, the switching pressure in the numerical model was set to $p_{\mathrm{R,sw}} = 6.1\,\mathrm{bar}$. However, for the present MH and the reference conditions, for this switching pressure the MH is not completely discharged, because the hydrogen content is still $\omega_{20°\mathrm{C}} = 0.45\,\mathrm{wt.\,\%}$ (cf. Figure 2-3). Thus, by decreasing the switching pressure, it is feasible to increase the theoretically usable hydrogen capacity $\Delta\omega_{\max}$. This can be facilitated, for example, by using an FC that requires a reduced backpressure and any pressure difference at the hydrogen outlet section has to be avoided. As can be seen in Figure 5-10, a decreased switching pressure leads to an extended CP and an increased average reactor cooling power is obtained. For instance, for a switching pressure of $p_{\overline{\mathrm{ab}}} = 2\,\mathrm{bar}$, the average reactor cooling power is enhanced by 28% compared to the reference conditions. Thus, for the present applied FC with a reactor switching pressure of $p_{\overline{\mathrm{ab}}} = 6.1\,\mathrm{bar}$, it might be reasonable to select an MH

with a higher equilibrium characteristic to avoid a switching pressure where a high hydrogen content is still available. However, with a higher equilibrium characteristic, an increased mechanical stability of the reactor is required to enable the regeneration at ambient temperature.

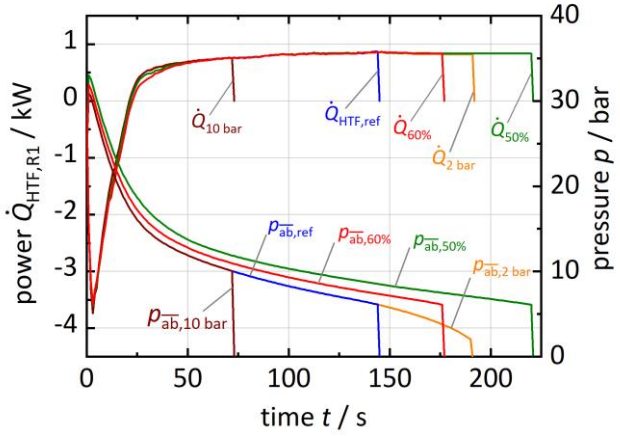

Figure 5-10: Temporal course of the reactor cooling power and pressure as a function of the MH bed porosity and switching pressure.

5.4 Performance of an improved design

Previously, reactor optimization recommendations were presented and their isolated effect on the cooling performance under reference conditions was discussed. Concluding this thesis, the combination of all optimization recommendations will be discussed in the following in order to demonstrate the obtainable power in harsher operating conditions and to show the remaining potential for increasing the system performance.

In this case, the time-shifted valve switching at the beginning of each HC is assumed to be implemented since the initial temperature of the remaining HTF is equal to the HTF inlet temperature at the beginning of the desorption. Thus, the reactor cooling power corresponds to cooling power in the cooling HTF loop. Reference conditions are applied in the numerical model and, compared to the present reactor design, the previously discussed optimization recommendations are included as follows:

- On the MH side, a half MH channel thickness of $d_{\mathrm{MH}} = 1.96\ \mathrm{mm}$ is used. This value is the optimum MH bed thickness between the objectives of avoiding heat transfer limitations and increasing the available MH capacity. Thus, an asymmetric reactor design with a slightly increased MH channel thickness and a reduced HTF channel thickness for low fluid exchange losses is obtained.

- To reduce the distance for the hydrogen gas transport in the MH bed, hydrogen is released at two sides of the reactor.
- The porosity in the MH bed is reduced from 68% to 60%.
- The switching pressure is decreased to 3 bar (reduced FC backpressure) and it is assumed that no pressure drop at the hydrogen outlet section occurs.

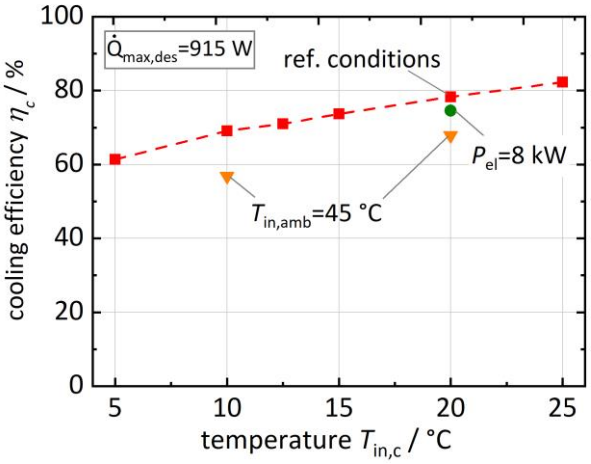

Figure 5-11: Cooling efficiency η_c of an improved reactor design for a variation of the cooling inlet temperature.

Figure 5-11 shows the simulated cooling efficiency of this improved plate reactor design for a variation of the cooling inlet temperature. The red line with square symbols corresponds to the optimized design under reference conditions, while the green circle and the orange triangles show the values for an electrical power of 8 kW and an inlet temperature of the ambient HTF cycle of 45 °C (except for P_{el} and $T_{\mathrm{in,amb}}$ reference conditions are applied). Due to the reduced bed porosity and the increased thickness of the MH channels, the available MH mass is increased by more than 55% compared to the present reactor, reaching a mass ratio of $k = 1.73$ for an empty reactor mass of 3.84 kg. Thus, the HC time is increased, while the MH channel thickness is still small enough that the reactor has a suitable heat transfer characteristic. Compared to the present design, therefore, even in harsher operating conditions high cooling efficiencies are feasible. For instance at $T_{\mathrm{c,in}} = 13$ °C and reference conditions, η_{c} corresponds to around 70%, while in the experimental results of the performance investigations only an efficiency of 20% was obtained for these conditions. Thus, the resulting average cooling power can be increased by more than 470 W compared to the experiments with the present plate reactor. At a very low cooling temperature of 10 °C and a high ambient temperature of 45 °C, still a cooling efficiency of $\eta_{\mathrm{c}} = 57\%$ and an average cooling power of 520 W is feasible with the optimized design. For an increased electrical FC power of 8 kW with $\dot{Q}_{\mathrm{max,des}} = 1440$ W, the improved reactor design enables an average cooling of 1092 W, reaching a cooling efficiency of $\eta_{\mathrm{c}} = 75\%$. These values show the potential

for improving the realized first-of-its-kind system and indicate that the open MHCS is able to operate in even harsher operating conditions.

As a final comment, since some of these measures to improve the performance are related to the overall system design, next to a direct integration between the pressure tank and the FC in the existing hydrogen infrastructure of an FC vehicle, the solution of an auxiliary power unit (APU) for battery electrical vehicles can be advantageous. In this solution, all single components of the APU (the separate hydrogen pressure tank, the FC and the open MHCS) can be tuned together to reach the best overall performance in providing electrical energy for increasing the vehicle driving range as well as heat and cold for the thermal management of the vehicle.

In general for all types of applications, it is recommended to use the open MHCS in many scenarios as possible throughout the year. So, next to the cooling mode, the system could also be applied for a continuous heating at low ambient temperatures or the purpose of precooling/-heating. Thereby, for a high cooling efficiency, small temperature differences between the regeneration HC and the cooling HC are generally preferable. According to this, a promising application might be the temperature control of vehicle components, such as the battery that do not require very low operating temperatures. As an innovative “hydrogen pressure transducer”, the system can be applied in any mobile and stationary application, where the hydrogen pressure is reduced and thermal energy is locally required.

Conclusions of the numerical analysis

With regard to its use in the open MHCS, in this section the promising plate reactor concept used in the previous chapters was numerically analyzed and design recommendations were given. The comparison with experimental data showed that the reactor model is suitable for an accurate performance prediction. With a view to increasing the power density, the minimization of thermal losses is crucial. For this purpose, the mass ratio k has to be reduced (e.g. by reducing the reactor mass) and appropriate measures have to be taken to avoid fluid exchange losses (e.g. the presented operation optimization). The variation of the thickness of the MH bed showed that there is a conflict between the objectives of avoiding heat transfer limitations and the available MH capacity. The half-channel thickness of the applied reactor is in the optimal range of 0.8–3 mm, leaving small space for geometric optimization. However, in order to reduce the existing pressure drop in the MH bed, it is suggested to reduce the distance for the hydrogen gas transport and to realize a reactor with a two-sided hydrogen inlet/outlet. Furthermore, a decrease of the porosity of the MH bed porosity as well as the FC backpressure is recommended. Summarizing all discussed optimization possibilities, even in harsher operating conditions cooling efficiencies above 60% are obtainable, which shows the automotive applicability of the open MHCS.

6. Summary

Compressed storage of hydrogen in high-pressure tanks is the established technology for automotive systems. However, an intrinsic problem of the state-of-the-art 700 bar tanks is that around 15% of the lower heating value of hydrogen is consumed by the compression to reach the required energy densities. By throttling the hydrogen to the fuel cell (FC) backpressure, the onboard available potential energy of compressed hydrogen has been wasted until now. Simultaneously, currently used cooling systems substantially decrease the driving range of FC vehicles as the electrical power is provided by the chemical energy of hydrogen. A promising option for the thermal management without the consumption of electrical energy is an open metal hydride (MH) cooling system. The system enables the utilization of the potential energy in the storage tank of an FC vehicle by providing heat or cold.

In the frame of this work, a systematic investigation and experimental demonstration of a first-of-its-kind system were presented. Thereby, the focus was on the cooling operation. According to the structure of the thesis, the results and main contributions can be summarized as follows:

The first part addressed the experimental details of this investigation. Based on the hydrogen pressure conditions, Hydralloy® C2 ($Ti_{0.98}Zr_{0.02}Mn_{1.46}V_{0.41}Cr_{0.05}Fe_{0.08}$) was chosen as the MH material and thermodynamically characterized in the relevant temperature range from 0–50 °C. The applied polynomial fitting method is suitable to describe the pressure–concentration isotherms, as the mean value deviation in the plateau region was below 7%. The realized MH cooling system (MHCS) consisted of two alternately working plate reactors, which are each filled with around 1.5 kg of MH, supplied with pressurized hydrogen and coupled to a polymer electrolyte membrane FC.

In the second part, the functional demonstration at an electrical FC power of 5 kW showed that the alternately desorbing reactors are able to continuously supply the hydrogen mass flow rate required for the FC operation. The absorption was conducted at a pressure of 35 bar and the half-cycles were automatically switched when the FC inlet pressure reached 4.3 bar. During the half-cycle duration of 145 s, the reactors released around 12 g of hydrogen, which corresponds to a used hydrogen capacity of 0.82 wt.%. Under reference conditions, a quasi-continuous average cooling power of 662 W at an ambient temperature of 30 °C and a cooling temperature of 20 °C was detected. Thus, referred to the compression work of 18 MJ kg_{H2}^{-1} required to increase the pressure to 700 bar, around 45% of the as-yet-unexploited potential energy can be transformed into useful cold. In order to reduce thermal losses that occur in the operation at two temperature levels, a novel operation optimization was presented. Through the time-shifted valve switching of the reactor outlet valves, fluid exchange losses are reduced and an increase of the cooling power by more than 50% compared to the case without its implementation was proven.

In the third part, performance investigations of the key influencing parameters were conducted. Overall, the system was able to operate in the entire range of varied operating conditions. However, the key influencing parameters, which are the electrical FC power and the operating temperature levels, had a significant impact on the resulting cooling performance. The variation of electrical FC power in the range of 1.8–7.9 kW showed a maximum average cooling power of 807 W at an electrical power of 7 kW. This corresponds to a specific cooling power of 564 W kg_{MH}^{-1} referred to the MH mass of a single reactor. Due to the increased thermal losses and the reduced HC time, the performance decreased with increased ambient temperatures (varied in the range of 24.3–43.3 °C) and reduced cooling temperatures (varied in the range of 13–25.4 °C).

In the fourth part, the novel plate reactor concept was numerically investigated and design recommendations for an improved power density of the open MHCS were given. Based on a simplified model geometry and a specific numerical model, a comparison with the experimental data showed that the reactor model is suitable for an accurate performance prediction of the reactor cooling power and the duration of the desorption half-cycle. With a view to increasing the power density, firstly, it is crucial to decrease thermal losses by improving the mass ratio k, which, for instance, can be obtained by reducing the reactor mass. Secondly, to fully exploit the available MH capacity, the pressure drop in the system´s hydrogen outlet and the MH bed has to be reduced. This can be realized by a reactor with a two-sided hydrogen inlet/outlet. Summarizing all discussed optimization possibilities, with regard to the maximum ratio of cooling power to electrical FC power of 18.3% for Hydralloy® C2, cooling efficiencies above 60% are feasible with an improved system design even in harsher operating conditions. The presented model can be applied to develop further reactor designs and for the implementation of the open MHCS in the overall vehicle simulation.

In summary, it can be stated that the utilization of the potential energy of hydrogen by the investigated open MHCS provides the possibility to increase the efficiency of FC vehicles and the green mobile hydrogen cycle. Thereby, a major drawback of the compressed storage in high-pressure tanks is partly compensated. In a next step, this increase of efficiency and the hydrogen saving potential has to be quantified when the open MHCS is implemented in a real vehicle. For this purpose, a suitable integration concept has to be developed and a further increase of the power density can be enabled with regard to the presented optimization recommendations. As an innovative “hydrogen pressure transducer”, the system can be transferred to all applications where the hydrogen pressure has to be throttled and thermal energy (heating or cooling) is locally required.

References

[1] Gulia S, Shiva Nagendra SM, Khare M, Khanna I. Urban air quality management-A review. Atmos Pollut Res 2015;6:286–304. doi:https://doi.org/10.5094/APR.2015.033.

[2] Wilberforce T, Alaswad A, Palumbo A, Dassisti M, Olabi AG. Advances in stationary and portable fuel cell applications. Int J Hydrogen Energy 2016;41:16509–22. doi:https://doi.org/10.1016/j.ijhydene.2016.02.057.

[3] Cano ZP, Banham D, Ye S, Hintennach A, Lu J, Fowler M, et al. Batteries and fuel cells for emerging electric vehicle markets. Nat Energy 2018;3:279–89. doi:http://dx.doi.org/10.1038/s41560-018-0108-1.

[4] A European Strategy for low-emission mobility. Webpage 2019. https://ec.europa.eu/clima/policies/transport_en (accessed October 26, 2019).

[5] Eberle U, Müller B, Von Helmolt R. Fuel cell electric vehicles and hydrogen infrastructure: Status 2012. Energy Environ Sci 2012;5:8780–98. doi:https://doi.org/10.1039/c2ee22596d.

[6] Ball M, Weeda M. The hydrogen economy - Vision or reality? Int J Hydrogen Energy 2015;40:7903–19. doi:http://dx.doi.org/10.1016/j.ijhydene.2015.04.032.

[7] Schlapbach L, Züttel A. Hydrogen storage materials for Mobile Applications. Nature 2001;414:353–8. doi:http://dx.doi.org/10.1038/35104634.

[8] Luo Y, Jiao K. Cold start of proton exchange membrane fuel cell. Prog Energy Combust Sci 2018;64:29–61. doi:https://doi.org/10.1016/j.pecs.2017.10.003.

[9] Züttel A, Remhof A, Borgschulte A, Friedrichs O. Hydrogen: The future energy carrier. Philos Trans R Soc A Math Phys Eng Sci 2010;368:3329–42. doi:https://doi.org/10.1098/rsta.2010.0113.

[10] Klell M. Storage of Hydrogen in the Pure Form. Handbook o. Wiley-VCH Verlag GmbH & Co. KGaA; 2010. doi:https://doi.org/10.1002/9783527629800.ch1.

[11] Jensen JO, Vestbø AP, Li Q, Bjerrum NJ. The energy efficiency of onboard hydrogen storage. J Alloys Compd 2007;446–447:723–8. doi:https://doi.org/10.1016/j.jallcom.2007.04.051.

[12] Qi Z. Advances on air conditioning and heat pump system in electric vehicles - A review. Renew Sustain Energy Rev 2014;38:754–64. doi:http://dx.doi.org/10.1016/j.rser.2014.07.038.

[13] Kambly K, Bradley TH. Geographical and temporal differences in electric vehicle range due to cabin conditioning energy consumption. J Power Sources 2015;275:468–75. doi:https://doi.org/10.1016/j.jpowsour.2014.10.142.

[14] Kambly KR, Bradley TH. Estimating the HVAC energy consumption of plug-in electric vehicles. J Power Sources 2014;259:117–24. doi:https://dx.doi.org/10.1016/j.jpowsour.2014.02.033.

[15] Pino FJ, Marcos D, Bordons C, Rosa F. Car air-conditioning considerations on hydrogen consumption in fuel cell and driving limitations. Int J Hydrogen Energy 2015;40:11696–703. doi:https://dx.doi.org/10.1016/j.ijhydene.2015.04.079.

[16] Peng Q, Du Q. Progress in heat pump air conditioning systems for electric vehicles-A review. Energies 2016;9. doi:https://doi.org/10.3390/en9040240.

[17] Regulation (EU) No 517/2014 of the European Parliament and of the Council of 16 April 2014 on fluorinated greenhouse gases and repealing Regulation (EC) No 842/2006, 2014.

[18] Skripnyuk VM, Ron M. Evaluation of kinetics by utilizing the normalized pressure dependence method for the alloy Ti0.95Zr0.05Mn1.48V0.43Fe0.08Al0.01. J Alloys Compd 1999;293–295:385–90. doi:https://doi.org/10.1016/S0925-8388(99)00375-8.

[19] Meunier F. Solid sorption heat powered cycles for cooling and heat pumping applications. Appl Therm Eng 1998;18:715–29. doi:https://doi.org/10.1016/S1359-4311(97)00122-1.

[20] Muthukumar P, Groll M. Metal hydride based heating and cooling systems: A review. Int J Hydrogen Energy 2010;35:3817–31. doi:https://doi.org/10.1016/j.ijhydene.2010.01.115.

[21] Wanner M. Untersuchung des Langzeitverhaltens der thermodynamischen Stabilität von Metallhydriden. Dissertation at the University of Stuttgart, 2001.

[22] Sakintuna B, Lamaridarkrim F, Hirscher M. Metal hydride materials for solid hydrogen storage: A review☆. Int J Hydrogen Energy 2007;32:1121–40. doi:https://doi.org/10.1016/j.ijhydene.2006.11.022.

[23] Sandrock G. Panoramic overview of hydrogen storage alloys from a gas reaction point of view. J Alloys Compd 1999;293–295:877–88. doi:https://doi.org/10.1016/S0925-8388(99)00384-9.

[24] Huot J. Metal Hydrides. In: Hirscher M, editor. Handb. Hydrog. Storage, Weinheim: Wiley-VCH Verlag GmbH & Co. KGaA; 2010.

[25] Weidenthaler C, Felderhoff M. Solid-state hydrogen storage for mobile applications: Quo Vadis? Energy Environ Sci 2011;4:2495–502. doi:https://doi.org/10.1039/c0ee00771d.

[26] Cao DL, Cheng HH, Ma L, Chen DM, Lue MQ, Yang K. Effects of Al partial substitution for Ni on properties of LaNi5-xAlx. Trans Nonferrous Met Soc China 2007;17:s967–71.

[27] Kandavel M, Ramaprabhu S. Hydriding properties of Ti-substituted non-stoichiometric AB2 alloys. J Alloys Compd 2004;381:140–50. doi:https://10.1016/j.jallcom.2004.03.081.

[28] Sharma VK, Anil Kumar E. Measurement and analysis of reaction kinetics of La – based hydride pairs suitable for metal hydride – based cooling systems. Int J Hydrogen Energy 2014;39:19156–68. doi:https://doi.org/10.1016/j.ijhydene.2014.09.083.

[29] Kandavel M, Bhat V V., Rougier A, Aymard L, Nazri G a., Tarascon JM. Improvement of hydrogen storage properties of the AB2 Laves phase alloys for automotive application. Int J Hydrogen Energy 2008;33:3754–61. doi:https://doi.org/10.1016/j.ijhydene.2008.04.042.

[30] Sastri MVC, Viswanathan B, Murthy SS. Metal Hydrides - Fundamentals and Applications. Springer; 1998.

[31] Linder M. Automotive Cooling Systems based on Metal Hydrides. Dissertation at the University of Stuttgart, 2010. doi:http://dx.doi.org/10.18419/opus-1882.

[32] Schlapbach L. Hydrogen in Intermetallic Compounds II- Surface and Dynamic Properties, Applications. vol. 67. Springer-Verlag Berlin Heidelberg; 1992. doi:https://doi.org/10.1007/3-540-54668-5.

[33] Buchner H. Energiespeicherung in Metallhydriden. Springer-Verlag Wien; 1982. doi:https://doi.org/10.1007/978-3-7091-8671-8.

[34] Doraiswamy LK, Sharma MM. Heterogeneous reactions: Analysis, examples, and reactor design. Volume 1: Gas -solid and solid -solid reactions. New York: 1984.

[35] Martin M, Gommel C, Borkhart C, Fromm E. Absorption and desorption kinetics of hydrogen storage alloys. J Alloys Compd 1996;238:193–201. doi:https://doi.org/10.1016/0925-8388(96)02217-7.

[36] Førde T. Theoretical and Experimental Studies of Metal Hydride Storage Units. Dissertation at the Norwegian University of Science and Technology, 2007.

[37] Skripnyuk M, Ron M. Hydrogen desorption kinetics in intermetallic compounds C2, C51 and C52 with Laves phase structure. Int J Hydrogen Energy 2003;28:303–9. doi:https://doi.org/10.1016/S0360-3199(02)00081-2.

[38] Corgnale C, Hardy BJ, Tamburello DA, Garrison SL, Anton DL. Acceptability envelope for metal hydride-based hydrogen storage systems. Int J Hydrogen Energy 2012;37:2812–24. doi:https://doi.org/10.1016/j.ijhydene.2011.07.037.

[39] Askri F, Ben Salah M, Jemni A, Ben Nasrallah S. Optimization of hydrogen storage in metal-hydride tanks. Int J Hydrogen Energy 2009;34:897–905. doi:https://doi.org/10.1016/j.ijhydene.2008.11.021.

[40] Yang FS, Wang GX, Zhang ZX, Meng XY, Rudolph V. Design of the metal hydride reactors - A review on the key technical issues. Int J Hydrogen Energy 2010;35:3832–40. doi:http://dx.doi.org/10.1016/j.ijhydene.2010.01.053.

[41] Vyazovkin S, Burnham AK, Criado JM, Pérez-Maqueda LA, Popescu C, Sbirrazzuoli N. ICTAC Kinetics Committee recommendations for performing kinetic computations on thermal analysis data. Thermochim Acta 2011;520:1–19. doi:https://doi.org/10.1016/j.tca.2011.03.034.

[42] Bürger I. Investigation of a New Reactor Concept for Hydrogen Storage in Complex Hydrides. Dissertation at the University of Stuttgart, 2014.

[43] MacDonald BD, Rowe AM. Impacts of external heat transfer enhancements on metal hydride storage tanks. Int J Hydrogen Energy 2006;31:1721–31. doi:https://doi.org/10.1016/j.ijhydene.2006.01.007.

[44] Murray J, Miller H, Bird P, Goudy AJ. The effect of particle size and surface composition on the reaction rates of some hydrogen storage alloys. J Alloys Compd 1995;231:841–5. doi:https://doi.org/10.1016/0925-8388(95)01769-0.

[45] Suzuki Y, Haraki T, Uchida H. Effect of LaNi5H6 hydride particles size on desorption kinetics. J Alloys Compd 2002;330–332:488–91. doi:https://doi.org/10.1016/S0925-8388(01)01645-0.

[46] Raed K. Investigation of Knudsen and Gas-Atmosphere Effects on effective thermal conductivity of porous media. Dissertation at the TU Bergakademie Freiberg, 2013.

[47] Hahne E, Kallweit J. Thermal conductivity of metal hydride materials for storage of hydrogen: Experimental investigation. Int J Hydrogen Energy 1998;23:107–14. doi:https://doi.org/10.1016/S0360-3199(97)00020-7.

[48] Matsushita M, Monde M, Mitsutake Y. Predictive calculation of the effective thermal conductivity in a metal hydride packed bed. Int J Hydrogen Energy 2014;39:9718–25. doi:https://doi.org/10.1016/j.ijhydene.2014.04.072.

[49] Lee M, Kim KJ, Hopkins RR, Gawlik K. Thermal conductivity measurements of copper-coated metal hydrides (LaNi5, Ca0.6Mm0.4Ni5, and LaNi4.75Al0.25) for use in metal hydride hydrogen compression systems. Int J Hydrogen Energy 2009;34:3185–90. doi:https://doi.org/10.1016/j.ijhydene.2009.01.078.

[50] Lototskyy M, Satya Sekhar B, Muthukumar P, Linkov V, Pollet BG. Niche applications of metal hydrides and related thermal management issues. J Alloys Compd 2015;645:117–22. doi:https://doi.org/10.1016/j.jallcom.2014.12.271.

[51] Payá J, Linder M, Mertz R, Corberán JM. Analysis and optimization of a metal hydride cooling system. Int J Hydrogen Energy 2011;36:920–30. doi:https://doi.org/10.1016/j.ijhydene.2010.08.112.

[52] Mosher DA, Arsenault S, Tang X, Anton DLL. Design, fabrication and testing of NaAlH4 based hydrogen storage systems. J Alloys Compd 2007;446–447:707–12. doi:https://doi.org/10.1016/j.jallcom.2007.01.042.

[53] Urbanczyk R, Peil S, Bathen D, Heßke C, Burfeind J, Hauschild K, et al. HT-PEM fuel cell system with integrated complex metal hydride storage tank. Fuel Cells 2011;11:911–20. doi:https://doi.org/10.1002/fuce.201100012.

[54] Bhouri M, Goyette J, Hardy BJ, Anton DL. Honeycomb metallic structure for improving heat exchange in hydrogen storage system. Int J Hydrogen Energy 2011;36:6723–38. doi:https://doi.org/10.1016/j.ijhydene.2011.02.092.

[55] Garrier S, Chaise A, de Rango P, Marty P, Delhomme B, Fruchart D, et al. MgH2 intermediate scale tank tests under various experimental conditions. Int J Hydrogen Energy 2011;36:9719–26. doi:https://doi.org/10.1016/j.ijhydene.2011.05.017.

[56] Pohlmann C, Röntzsch L, Hu J, Weißgärber T, Kieback B, Fichtner M, et al. Tailored heat transfer characteristics of pelletized LiNH2–MgH2 and NaAlH4 hydrogen storage materials. J Power Sources 2012;205:173–9. doi:https://doi.org/10.1016/j.jpowsour.2012.01.064.

[57] Chaise A, de Rango P, Marty P, Fruchart D, Miraglia S, Olivès R, et al. Enhancement of hydrogen sorption in magnesium hydride using expanded natural graphite. Int J Hydrogen Energy 2009;34:8589–96. doi:https://doi.org/10.1016/j.ijhydene.2009.07.112.

[58] Johnson TA, Kanouff MP, Dedrick DE, Evans GH, Jorgensen SW. Model-based design of an automotive-scale, metal hydride hydrogen storage system. Int J Hydrogen Energy 2012;37:2835–49. doi:https://doi.org/10.1016/j.ijhydene.2011.05.030.

[59] Van Hassel BA, Mosher D, Pasini JMM, Gorbounov M, Holowczak J, Tang X, et al. Engineering improvement of NaAlH4 system. Int J Hydrogen Energy 2012;37:2756–66. doi:https://doi.org/10.1016/j.ijhydene.2011.02.005.

[60] Kim KJ, Lloyd GM, Razani A. Thermal analysis of the Ca0.4Mm0.6Ni5 metal–hydride reactor. Appl Therm Eng 1998;18:1325–36. doi:https://doi.org/10.1016/S1359-4311(98)00007-6.

[61] Yang F, Meng X, Deng J, Wang Y, Zhang Z. Identifying heat and mass transfer characteristics of metal hydride reactor during adsorption: Improved formulation about parameter analysis. Int J Hydrogen Energy 2009;34:1852–61. doi:https://doi.org/10.1016/j.ijhydene.2008.11.119.

[62] Mat MD, Kaplan Y, Aldas K. Investigation of three-dimensional heat and mass transfer in a metal hydride reactor. Int J Energy Res 2002;26:973–86. doi:https://doi.org/10.1002/er.831.

[63] Payá J, Linder M, Laurien E, Corberán JM. Dynamic model and experimental results of a thermally driven metal hydride cooling system. Int J Hydrogen Energy 2009;34:3173–84. doi:https://doi.org/10.1016/j.ijhydene.2009.01.085.

[64] Linder M, Mertz R, Laurien E. Experimental results of a compact thermally driven cooling system based on metal hydrides. Int J Hydrogen Energy 2010;35:7623–32. doi:https://doi.org/10.1016/j.ijhydene.2010.04.184.

[65] Kim KJ, Feldman KT, Lloyd G, Razani A. Compressor-driven metal-hydride heat pumps. Appl Therm Eng 1997;17:551–60. doi:https://doi.org/10.1016/S1359-4311(96)00067-1.

[66] Ron M. A HYDROGEN HEAT PUMP AS A BUS AIR CONDITIONER. J Less-Common Met 1984;104:259–78. doi:https://doi.org/10.1016/0022-5088(84)90411-9.

[67] Muthukumar P, Patil MS, Raju NN, Imran M. Parametric investigations on compressor-driven metal hydride based cooling system. Appl Therm Eng 2016;97:87–99. doi:https://doi.org/10.1016/j.applthermaleng.2015.10.155.

[68] Bedbak SS, Gopal MR. Performance analysis of a compressor driven metal hydride cooling system. Int J Hydrogen Energy 2005;30:1127–37. doi:https://doi.org/10.1016/j.ijhydene.2004.10.014.

[69] Heubner F, Pohlmann C, Mauermann S, Kieback B, Röntzsch L. Mechanical stresses originating from metal hydride composites during cyclic hydrogenation. Int J Hydrogen Energy 2015;40:10123–30. doi:https://doi.org/10.1016/j.ijhydene.2015.06.053.

[70] Saito T, Suwa K, Kawamura T. Influence of expansion of metal hydride during hydriding–dehydriding cycles. J Alloys Compd 1997;253–254:682–5. doi:https://doi.org/10.1016/S0925-8388(96)02893-9.

[71] Nasako K, Ito Y, Hiro N, Osumi M. Stress on a reaction vessel by the swelling of a hydrogen absorbing alloy. J Alloys Compd 1998;264:271–6. doi:https://doi.org/10.1016/S0925-8388(97)00246-6.

[72] Charlas B, Kneib F, Gillia O, Imbault D, Doremus P. A tool for modelling the breathing of hydride powder in its container while cyclically absorbing and desorbing hydrogen. Int J Hydrogen Energy 2015;40:2283–94. doi:https://doi.org/10.1016/j.ijhydene.2014.11.077.

[73] Nakamura Y, Sato K, Fujitani S, Nishio K, Oguro K, Uehara I. Lattice expanding behaviour and degradation of LaNi5-based alloys. J Alloys Compd 1998;267:205–10. doi:https://doi.org/10.1016/S0925-8388(97)00503-3.

[74] Salque B, Chaise A, Iosub V, Gillia O, Charlas B, Dupuis C, et al. Measure of the hydride breathing while cyclically absorbing and desorbing hydrogen. J Alloys Compd 2015;645:S353–6. doi:https://doi.org/10.1016/j.jallcom.2014.12.112.

[75] Qin F, Guo LH, Chen JP, Chen ZJ. Pulverization, expansion of La0.6Y0.4Ni4.8Mn0.2 during hydrogen absorption-desorption cycles and their influences in thin-wall reactors. Int J Hydrogen Energy 2008;33:709–17. doi:https://doi.org/10.1016/j.ijhydene.2007.10.029.

[76] Charlas B, Gillia O, Doremus P, Imbault D. Experimental investigation of the swelling/shrinkage of a hydride bed in a cell during hydrogen absorption/desorption cycles. Int J Hydrogen Energy 2012;37:16031–41. doi:https://doi.org/10.1016/j.ijhydene.2012.07.091.

[77] Arvind Varma HTH. Hydrogen storage for fuel cell vehicles. Curr Opin Chem Eng 2014;5:42–8. doi:https://doi.org/10.1016/j.coche.2014.04.004.

[78] U.S. Department of Energy. 3.3 Hydrogen Storage. Fuel Cell Technol Off Multi-Year Res Dev Demonstr Plan 2015:23. https://www.energy.gov/sites/prod/files/2015/05/f22/fcto_myrdd_storage.pdf (accessed September 26, 2019).

[79] Office of Energy Efficiency and Renewable Energy. https://www.energy.gov/eere/fuelcells/hydrogen-storage (accessed September 26, 2019).

[80] Rivard E, Trudeau M, Zaghib K. Hydrogen storage for mobility: A review. Materials (Basel) 2019;12. doi:https://doi.org/10.3390/ma12121973.

[81] Yoshida T, Kojima K. Toyota MIRAI Fuel Cell Vehicle and Progress Toward a Future Hydrogen Society. Interface Mag 2015;24:45–9. doi:https://doi.org/10.1149/2.f03152if.

[82] H2 MOBILITY Deutschland GmbH & Co. KG. https://h2.live/h2mobility (accessed September 26, 2019).

[83] Barthelemy H, Weber M, Barbier F. Hydrogen storage: Recent improvements and industrial perspectives. Int J Hydrogen Energy 2017;42:7254–62. doi:https://doi.org/10.1016/j.ijhydene.2016.03.178.

[84] Monterey G. Energy requirements for hydrogen gas compression and liquefaction as related to vehicle storage needs. DOE Hydrog Fuel Cells Progr Rec 2009.

[85] Stephan K, Mayinger F. Thermodynamik - Band 1: Einstoffsysteme. Grundlagen und technische Anwendungen. vol. 18. Auflag. Springer-Verlag Berlin Heidelberg; 1998. doi:https://doi.org/10.1007/978-3-540-92895-9.

[86] Bossel U, Eliasson B, Taylor G. The Future of the Hydrogen Economy: Bright or Bleak? 2003. https://planetforlife.com/pdffiles/h2report.pdf.

[87] Weindorf W, Bünger U, Schindler J. Comments on the paper by baldur Eliasson and Ulf Bossel "The future of the hydrogen Economy: bright or bleak." 2003.

[88] Bellosta von Colbe J, Ares JR, Barale J, Baricco M, Buckley C, Capurso G, et al. Application of hydrides in hydrogen storage and compression: Achievements, outlook and perspectives. Int J Hydrogen Energy 2019;44:7780–808. doi:https://doi.org/10.1016/j.ijhydene.2019.01.104.

[89] Durbin DJ, Malardier-Jugroot C. Review of hydrogen storage techniques for on board vehicle applications. Int J Hydrogen Energy 2013;38:14595–617. doi:https://doi.org/10.1016/j.ijhydene.2013.07.058.

[90] Ward P a., Corgnale C, Teprovich J a., Motyka T, Hardy B, Peters B, et al. High performance metal hydride based thermal energy storage systems for concentrating solar power applications. J Alloys Compd 2015;645:S374–8. doi:https://doi.org/10.1016/j.jallcom.2014.12.106.

[91] Aswin N, Dutta P, Murthy SS. Screening of metal hydride pairs for closed thermal energy storage systems. Appl Therm Eng 2016. doi:https://doi.org/10.1016/j.applthermaleng.2016.04.129.

[92] Muthukumar P, Kumar A, Raju NN, Malleswararao K, Rahman MM. A critical review on design aspects and developmental status of metal hydride based thermal machines. Int J Hydrogen Energy 2018;43:17753–79. doi:https://doi.org/10.1016/j.ijhydene.2018.07.157.

[93] N'Tsoukpoe KE, Liu H, Le Pierrès N, Luo L. A review on long-term sorption solar energy storage. Renew Sustain Energy Rev 2009;13:2385–96. doi:https://doi.org/10.1016/j.rser.2009.05.008.

[94] Lototskyy M V., Yartys VA, Pollet BG, Bowman RC. Metal hydride hydrogen compressors: A review. Int J Hydrogen Energy 2014;39:5818–51. doi:https://doi.org/10.1016/j.ijhydene.2014.01.158.

[95] Dieterich M, Bürger I, Linder M. Open and closed metal hydride system for high thermal power applications: preheating vehicle components. Int J Hydrogen Energy 2017;42:11469–81. doi:https://doi.org/10.1016/j.ijhydene.2017.03.024.

[96] Klein H. Betriebsverhalten einer zweistufigen Metallhydrid-Sorptionsanlage zur Kälteerzeugung. Dissertation at the Universoty of Stuttgart, 2007. doi:http://dx.doi.org/10.18419/opus-1744.

[97] Kölbig M. Coupled metal hydride reactions for preheating vehicle components at low temperatures. Dissertation at the University of Stuttgart, 2018. doi:http://dx.doi.org/10.18419/opus-10158.

[98] Linder M, Kulenovic R. An energy-efficient air-conditioning system for hydrogen driven cars. Int J Hydrogen Energy 2011;36:3215–21. doi:https://doi.org/10.1016/j.ijhydene.2010.11.101.

[99] Park JG, Han SC, Jang HY, Lee SM, Lee PS, Lee JY. The development of compressor-driven metal hydride heat pump (CDMHHP) system as an air conditioner. Int J Hydrogen Energy 2002;27:941–4. doi:https://doi.org/10.1016/S0360-3199(01)00187-2.

[100] Willers E. Multi-Hydrid-Sorptionsanlage zur kombinierten Heizung und Kühlung. Dissertation at the University of Stuttgart, 2002. doi:http://dx.doi.org/10.18419/opus-1556.

[101] Zhai Q, Wang RZ, Wu JY, Dai YJ, Ma Q. Design and performance of a solar-powerered air-conditioning system in a green building. Appl Energy 2008;85:297–311. doi:https://doi.org/10.1016/j.apenergy.2007.07.016.

[102] Tso CY, Chan KC, Chao CYH, Wu CL. Experimental performance analysis on an adsorption cooling system using zeolite 13X/CaCl2 adsorbent with various operation sequences. Int J Heat Mass Transf 2015;85:343–55. doi:https://doi.org/10.1016/j.ijheatmasstransfer.2015.02.005.

[103] Willers E, Groll M. The two-stage metal hydride heat transformer. Int J Hydrogen Energy 1999;24:269–76. doi:https://doi.org/10.1016/S0360-3199(98)00058-5.

[104] Satheesh A, Muthukumar P. Performance investigation of double-stage metal hydride based heat pump. Appl Therm Eng 2010;30:2698–707. doi:https://doi.org/10.1016/j.applthermaleng.2010.07.021.

[105] Gruen DM, Mendelsohn MH, Sheft I. Metal hydrides as chemical heat pumps. Sol Energy 1978;21:153–6. doi:https://doi.org/10.1016/0038-092X(78)90043-9.

[106] Magnetto D, Mola S, DaCosta DH, Golben M, Rosso M. A Metal Hydride Mobile Air Conditioning System. J Passeng CAR Mech Syst 2006;115:1150–9. doi:https://doi.org/10.4271/2006-01-1235.

[107] Hosoz M, Direk M. Performance evaluation of an integrated automotive air conditioning and heat pump system. Energy Convers Manag 2006;47:545–59. doi:https://doi.org/10.1016/j.enconman.2005.05.004.

[108] Baheta AT, Hassan S, Reduan ARB, Woldeyohannes AD. Performance investigation of transcritical carbon dioxide refrigeration cycle. Procedia CIRP 2015;26:482–5. doi:https://doi.org/10.1016/j.procir.2015.02.084.

[109] Ahn J, Kang H, Lee H, Kim Y. Performance characteristics of a dual-evaporator heat pump system for effective dehumidifying and heating of a cabin in electric vehicles. Appl Energy 2015;179:29–37. doi:https://doi.org/10.1016/j.apenergy.2015.01.124.

[110] Sharafian A, Mehr SN, Thimmaiah P, Huttema W, Bahrami M. Effects of adsorbent mass and number of adsorber beds on the performance of a waste- heat driven adsorption cooling system for vehicle air conditioning applications. Energy 2015;112:481–93. doi:https://doi.org/10.1016/j.energy.2016.06.099.

[111] Bhuiya MMH, Kumar A, Kim KJ. Metal hydrides in engineering systems, processes, and devices: A review of non-storage applications. Int J Hydrogen Energy 2015;40:2231–47. doi:https://doi.org/10.1016/j.ijhydene.2014.12.009.

[112] Chernikov AS, Izhvanov L., Solovey A., Frolov V., Shanin Y. An installation for water cooling based on a metal hydride heat pump. J Alloys Compd 2002;330–332:907–10. doi:https://doi.org/10.1016/S0925-8388(01)01479-7.

[113] Ni J, Liu H. Experimental research on refrigeration characteristics of a metal hydride heat pump in auto air-conditioning. Int J Hydrogen Energy 2007;32:2567–72. doi:https://doi.org/10.1016/j.ijhydene.2006.09.038.

[114] Qin F, Chen J, Lu M, Zhijiu C, Zhou Y, Yang K. Development of a metal hydride refrigeration system as an exhaust gas-driven automobile air conditioner. Renew Energy 2007;32:2034–52. doi:https://doi.org/10.1016/j.renene.2006.10.014.

[115] Yasuda N, Tsuchiya T, Okinaka N, Akiyama T. Application of metal hydride sheet to thermally driven cooling system. Int J Hydrogen Energy 2013;38:7469–76. doi:https://doi.org/10.1016/j.ijhydene.2013.04.011.

[116] Fang ZZ, Zhou C, Fan P, Udell KS, Bowman R, Vajo J, et al. Metal hydrides based high energy density thermal battery. Jouranl Alloy Compunds 2015;645:S184–9.

[117] Weckerle C, Bürger I, Linder M. Numerical optimization of a plate reactor for a metal hydride open cooling system. Int J Hydrogen Energy 2019;44:16862–76. doi:https://doi.org/10.1016/j.ijhydene.2019.04.260.

[118] Weckerle C, Bürger I, Linder M. Experimental demonstration of a metal hydride air-conditioning system for fuel cell vehicles - Functional demonstration. Appl Energy In Press, Corrected Proof :114187. doi:https://doi.org/10.1016/j.apenergy.2019.114187.

[119] Wanner M, Friedlmeier G, Hoffmann G, Groll M. Thermodynamic and structural changes of various intermetallic compounds during extended cycling in closed systems. J Alloys Compd 1997;253–254:692–7. doi:https://doi.org/10.1016/S0925-8388(96)03041-1.

[120] Musat R, Helerea E. Parameters and Models of the Vehicle Thermal Comfort. 2009.

[121] Willers E. Multi-Hydrid-Sorptionsanlage zur kombinierten Heizung und Kühlung. Dissertation at the University of Stuttgart, 2002. doi:http://dx.doi.org/10.18419/opus-1556.

[122] Koller D. Thermodynamische Charakterisierung und Modellierung von Metallhydriden für die Fahrzeugklimatisierung. Master thesis at the University of Stuttgart, 2018.

[123] Bhouri M, Linder M, Bürger I. Metal hydride reactor for dual use: hydrogen storage and cold production. Int J Hydrogen Energy 2018;43:23357–71. doi:https://doi.org/10.1016/j.ijhydene.2018.10.194.

[124] Bürger I, Dieterich M, Pohlmann C, Röntzsch L, Linder M. Standardized hydrogen storage module with high utilization factor based on metal hydride-graphite composites. J Power Sources 2017;342:970–9. doi:https://doi.org/10.1016/j.jpowsour.2016.12.108.

[125] Lototsky M V., Yartys VA, Marinin VS, Lototsky NM. Modelling of phase equilibria in metal-hydrogen systems. J Alloys Compd 2003;356–357:27–31. doi:https://doi.org/10.1016/S0925-8388(03)00095-1.

[126] Zhou Z, Zhang J, Ge J, Feng F, Dai Z. Mathematical modeling of the PCT curve of hydrogen storage alloys. Int J Hydrogen Energy 1994;19:269–73. doi:https://doi.org/10.1016/0360-3199(94)90097-3.

[127] Paya J, Linder M, Laurien E, Corberan JM. Mathematical models for the P-C-T characterization of hydrogen absorbing alloys. J Alloys Compd 2009;484:190–5. doi:https://doi.org/10.1016/j.jallcom.2009.05.069.

[128] Jemni A, Nassrallah S ben, Lamloumi J. Experimental and theoretical study of a metal-hydrogen reactor. Int j Ournal Hydrog Energy 1999;24:631–44. doi:https://doi.org/10.1016/S0360-3199(98)00117-7.

[129] Gambini M, Manno M, Vellini M. Numerical analysis and performance assessment of metal hydride-based hydrogen storage systems. Int J Hydrogen Energy 2008;33:6178–87. doi:https://doi.org/10.1016/j.ijhydene.2008.08.006.

[130] Weckerle C, Bürger I, Linder M. Novel reactor design for metal hydride cooling systems. Int J Hydrogen Energy 2017;42:8063–74. doi:https://doi.org/10.1016/j.ijhydene.2017.01.066.

[131] M. Wanner, G. Hoffmann MG. Thermodynamic and Structural Changes of an Ab2-Laves-Phase Alloy (Ti0.98 Zr0.02 V0.43 Fe0.06 Cr0.05 Mn1.52) During Extended Thermal Cycling. Hydrog Power Theor Eng Solut 1998;9:257–62. doi:http://dx.doi.org/10.1007/978-94-015-9054-9_33.

[132] Ron M. The normalized pressure dependence method for the evaluation of kinetic rates of metal hydride formation/decomposition. J Alloys Compd 1999;283:178–91. doi:https://doi.org/10.1016/S0925-8388(98)00859-7.

[133] Taylor JR. An Introduction to Error Analysis: The Study of Uncertainties in Physical Measurements. Sausalito, California: 1997.

[134] Weckerle C, Nasri M, Hegner R, Linder M, Bürger I. A metal hydride air-conditioning system for fuel cell vehicles – Performance investigations. Appl Energy 2019;256:113957. doi:https://doi.org/10.1016/j.apenergy.2019.113957.

[135] Meng X, Wu Z, Bao Z, Yang F, Zhang Z. Performance simulation and experimental confirmation of a mini-channel metal hydrides reactor. Int J Hydrogen Energy 2013;38:15242–53. doi:https://doi.org/10.1016/j.ijhydene.2013.09.056.

[136] Bao Z. Performance investigation and optimization of metal hydride reactors for high temperature thermochemical heat storage. Int J Hydrogen Energy 2015;40:5664–76. doi:https://doi.org/10.1016/j.ijhydene.2015.02.123.

[137] Herbrig K, Röntzsch L, Pohlmann C, Weißgärber T, Kieback B. Hydrogen storage systems based on hydride–graphite composites: computer simulation and experimental validation. Int J Hydrogen Energy 2013:1–11. doi:https://doi.org/10.1016/j.ijhydene.2013.03.104.

[138] Nassrallah S ben, Jemni A. Heat and mass transfer models in metal-hydrogen reactor. Int J Hydrog Energy 1997;22:67–76. doi:https://doi.org/10.1016/S0360-3199(96)00039-0.

[139] Blinov D V., Dunikov DO, Kazakov AN. Measuring the gas permeability of a metal hydride bed of the LaNi5 type alloy. High Temp 2016;54:153–6. doi:https://doi.org/10.1134/S0018151X1506005X.

[140] Massoud Kaviany. Essentials of Heat Transfer: Principles, Materials, and Appplications. 2011. doi:https://doi.org/10.1017/CBO9780511998195.

[141] Pradhan RL, Ravikumar D, Pradhan DL. Review of Nusselt Number Correlation for Single Phase Fluid Flow through a Plate Heat Exchanger to Develop C # Code Application Software. IOSR J Mech Civ Eng 2008.

[142] Hashmi A, Tahir F, Hameed U. Empirical Nusselt Number Correlation for Single Phase Flow through a Plate Heat Exchanger. Recent Adv Fluid Mech Heat Mass Transf Biol - Proc 9th WSEAS Int Conf HEAT MASS Transf (HMT '12) 2012:41–6.

[143] Cieśliński JT, Fiuk A, Typiński K, Siemieńczuk B. Heat transfer in plate heat exchanger channels: Experimental validation of selected correlation equations. Arch Thermodyn 2016;37:19–29. doi:https://doi.org/10.1515/aoter-2016-0017.

[144] Martin H. A theoretical approach to predict the performance of chevron-type plate heat exchangers. Chem Eng Process Process Intensif 1996;35:301–10. doi:https://doi.org/10.1016/0255-2701(95)04129-X.

[145] Suda S, Komazaki Y, Kobayashi N. Effective thermal conductivity of metal hydride beds. J Less Common Met 1983;89:1983. doi:https://doi.org/10.1016/0022-5088(83)90340-5.

[146] Garrison SL, Hardy BJ, Gorbounov MB, Tamburello DA, Corgnale C, Vanhassel BA, et al. Optimization of internal heat exchangers for hydrogen storage tanks utilizing metal hydrides. Int J Hydrogen Energy 2012;37:2850–61. doi:https://doi.org/10.1016/j.ijhydene.2011.07.044.

[147] Dieterich M, Pohlmann C, Bürger I, Linder M, Röntzsch L. Long-term cycle stability of metal hydride-graphite composites. Int J Hydrogen Energy 2015;40:16375–82. doi:https://doi.org/10.1016/j.ijhydene.2015.09.013.

[148] Capurso G, Schiavo B, Jepsen J, Lozano G, Klassen T, Dornheim M. Development of a modular room-temperature hydride storage system for vehicular applications. Appl Phys A 2016;236:1–11. doi:https://doi.org/10.1007/s00339-016-9771-x.

[149] Gstrein G, Klell M. Stoffwerte von Wasserstoff. Technische Universität Graz: Institut für Verbrennungskraftmaschinen und Thermodynamik; 2004.

[150] Herbrig K, Röntzsch L, Pohlmann C, Weißgärber T, Kieback B. Hydrogen storage systems based on hydride-graphite composites: Computer simulation and experimental validation. Int J Hydrogen Energy 2013;38:7026–36. doi:https://doi.org/10.1016/j.ijhydene.2013.03.104.

[151] Broom DP. The accuracy of hydrogen sorption measurements on potential storage materials. Int J Hydrogen Energy 2007;32:4871–88. doi:https://doi.org/10.1016/j.ijhydene.2007.07.056.

[152] Tao Y, Lee H, Hwang Y, Radermacher R, Wang C. Electrochemical compressor driven metal hydride heat pump. Int J Refrig 2015;60:278–88. doi:https://doi.org/10.1016/j.ijrefrig.2015.08.018.

Appendix

A. Work of isothermal compression for real gas behaviour

In Chapter 1.4.2, the energy required to compress hydrogen from standard pressure to the final pressure $p_1$is discussed. The work of isothermal compression for real gas behaviour in Figure 1-9 is determined as follows. A convenient approach to consider real gas behaviour at pressures above 100 bar is to use the dimensionless compressibility factor Z. For hydrogen pressures up to 1000 bar and a gas temperature of 300 K, the compressibility factor Z is given by [11]:

$$Z = 1 + k_z \ln(\frac{p}{p_{amb}}) \tag{A-1}$$

Using the real gas equation and with $k_z = 6.31 \cdot 10^{-4}$, the work of isothermal compression for real gas behaviour can be expressed as follows:

$$w_{ic,RG} = p_1 v_1 \left[k_z \frac{p_2 - p_1}{p_{amb}} + \ln(\frac{p_2}{p_1}) \right] \tag{A-2}$$

B. *T–s* diagram of hydrogen

To determine the maximum useful work w_{ex} that can be extracted from the hydrogen pressure tank in Chapter 1.4.2, the following *T–s* diagram of hydrogen in the temperature range from 85–330 K is applied. With $h = u + pv$ and equation (1-18), the maximum useful work w_{ex} is given by:

$$-w_{\mathrm{ex}} = h_{\mathrm{cd}} - h_{\mathrm{amb}} - T_{\mathrm{amb}}(s_{\mathrm{cd}} - s_{\mathrm{amb}}) + v_{\mathrm{cd}}(p_{\mathrm{amb}} - p_{\mathrm{cd}}) \qquad \text{(B-1)}$$

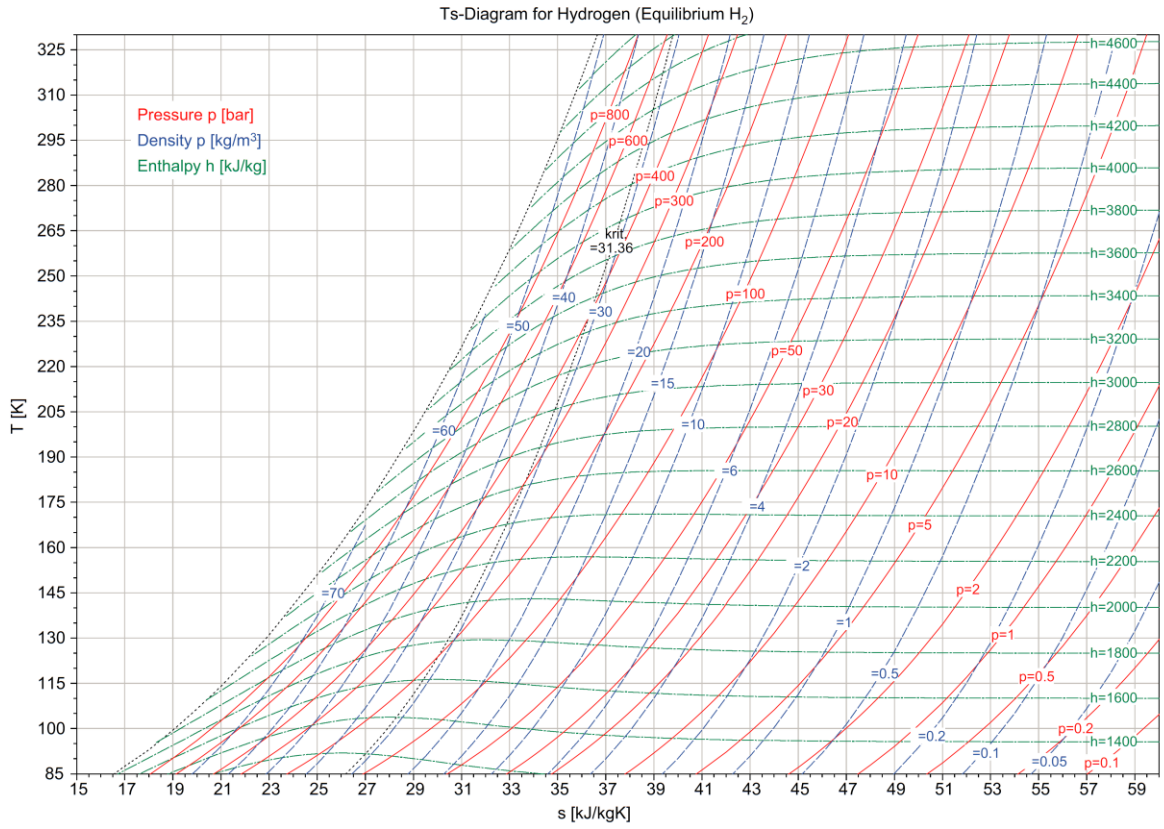

Figure B-1: *T-s* diagram of equilibrium hydrogen for temperatures from 85 to 330 K. Reprinted with permission from [149].

C. Single reactor characterization

The plate reactor concept was applied in the present thesis for the first systematic investigation of the open MHCS. The proof of concept of this novel design was conducted in single reactor measurements without coupling to an FC and the performance was compared to intrinsic material kinetic data (results have been published in [118]). To demonstrate the feasibility of the plate reactor concept, in the following an extract of these results (representative absorption experiment) including the experimental details is given.

Reactor design for the single reactor characterization

The proof of concept was conducted with a soldered plate heat reactor from VAU Thermotech GmbH & Co. KG with a one-way flow pattern. The design of the reactor is shown in Figure C-1 and Table C-1 summarizes all relevant design parameters (in the present thesis an up-scaled version of this concept is used). The connections for the HTF are C3 (inlet) and C4 (outlet), respectively. While connection C1 is applied for the hydrogen supply and removal, connection C2, which is closed during operation, is used for the filling of the reactor with MH.

Table C-1: Plate reactor characteristics for the single reactor characterization.

Description	Value
Average channel thickness	~1.5 mm
Empty reactor mass	1.6 kg (without connections)
Mass ratio of reactor R1 and R2	$k = 4.53$
Max. permitted pressure	30 bar
Max. permitted temperature	195 °C
MH mass of reactor R1 and R2	0.353 kg
Number of HTF channels	$N_{\mathrm{HTF}} = 10$
Number of MH channels	$N_{\mathrm{MH}} = 9$
Number of separating steel plates	$N_{\mathrm{SP}} = 20$
Reactor dimensions	203 mm × 73 mm × 66 mm ($l \times b \times h_{\mathrm{R}}$)

Due to its appropriate thermodynamic behaviour and excellent intrinsic kinetics [18], for the proof of concept of the plate reactor, Hydralloy® C5 ($Ti_{0.95}Zr_{0.05}Mn_{1.46}V_{0.41}Fe_{0.09}Cr_{0.05}$) was chosen as the MH material[2]. The equilibrium pressures at 35 °C and 15 °C are $p_{\mathrm{abs}} = 16.1$ bar and $p_{\mathrm{des}} = 4.5$ bar, respectively [150]. To exclude reactor failure, the small scale plate reactor was filled with a bulk density of 2300 kg m^{-3} and a safety factor of 30% was additionally included. Thus, the reactor was filled with a total MH mass of 0.353 kg.

[2] Hydralloy® C5 and Hydralloy® C2 have a similar composition and both show excellent intrinsic kinetics. Due to the higher thermodynamic equilibrium characteristics, Hydralloy® C2 was selected for the experimental demonstration of the MHCS with a minimum operating FC backpressure of 4.1 bar.

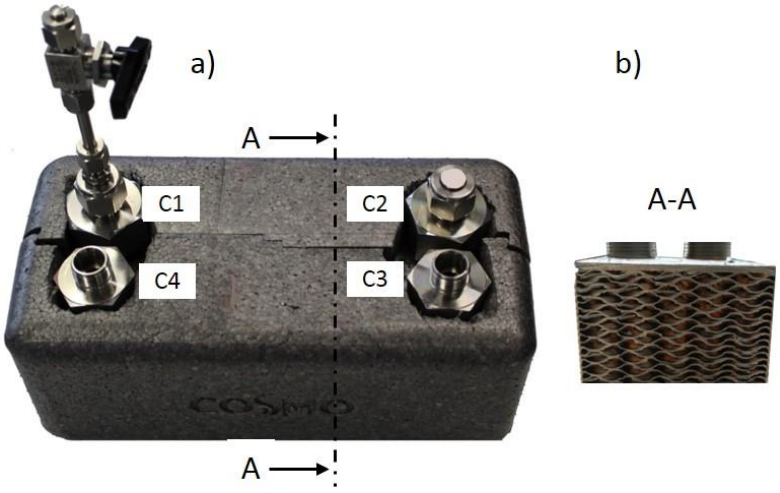

Figure C-1: Design of the plate reactor for the single reactor characterization. a) Converted state with connections and insulation b) unfilled cross-sectional view.

Experimental setup and measurement procedure

For the experimental validation, the plate reactor was integrated into the experimental setup shown in Figure C-1. In principle, the setup was divided into a hydrogen part and an HTF cycle (shown in blue) on the right hand side of the test bench scheme. The hydrogen part consisted of a reference volume RV (hydrogen gas bottle with a volume of 50 dm^3), a pressure reducing valve PRV, a thermocouple T_1, three pneumatic valves $V_{1\text{-}3}$, two hand valves $HV_{1\text{-}2}$ and three pressure sensors PS 1-2/VPS.

In the HTF cycle, the reactor inlet temperature was controlled via the thermostatic bath TB, which supplied the required heat and cold, respectively, to keep the HTF inlet temperature constant during the experiments. To determine the thermal power transferred to/from the HTF, the volume flow rate $\dot{V}_{\mathrm{HTF}}(t)$ and the HTF inlet and outlet temperatures (T_{in} and T_{out}) of the reactor were measured with a turbine flow meter FM (type: KEM HMP 06-SC, ±2.5%) and two thermocouples of Type K (±1.5 K, temperature difference calibrated). The instantaneously transferred specific power was referred to the MH mass m_{MH} and calculated according to equation (2-7).

Before the absorption experiment was initiated, the reactor was completely discharged by a vacuum pump (valves $HV_{1\text{-}2}$ and V_2 open) down to a system pressure of 50 mbar at room temperature. The desired HTF inlet temperature was set via the thermostatic bath until steady-state conditions between the HTF inlet and outlet temperature were obtained. After closing V_2, the absorption pressure p_{abs} was adjusted with hydrogen from the reference volume and the pressure reducing valve PRV. By opening V_2, hydrogen flowed from the reference volume into the hydrogen part of the plate reactor, the exothermic reaction was initiated and heat was transferred to the HTF depending on the boundary conditions of the reaction. The amount of

hydrogen absorbed in the MH is directly correlated with a pressure drop in the reference volume that is detected for each instant of time with the pressure sensor PS1 (type: Keller LEO3, ±0.2%). Using this Sieverts system [151] and considering the gas expansion in the free volume, the transformed fraction $x(t)$ according to equation (1-7) was calculated using real gas behaviour with, for instance, a real gas factor of 1.092 at a reference volume pressure of 150 bar. Thereby, the free volume including the tubes and free reactor volume was previously determined using inert gas. Due to the pressure reducing valve PRV, the Sieverts type measurement can be combined with a constant supply pressure to the reactor. Therefore, the fraction was completely transformed at constant pressure. With the resulting transformed fraction profile, the time constant τ (time required to reach 63.2% of the total absorbed hydrogen mass) and the HC time for a complete transformed fraction were determined (see Chapter 3.1).

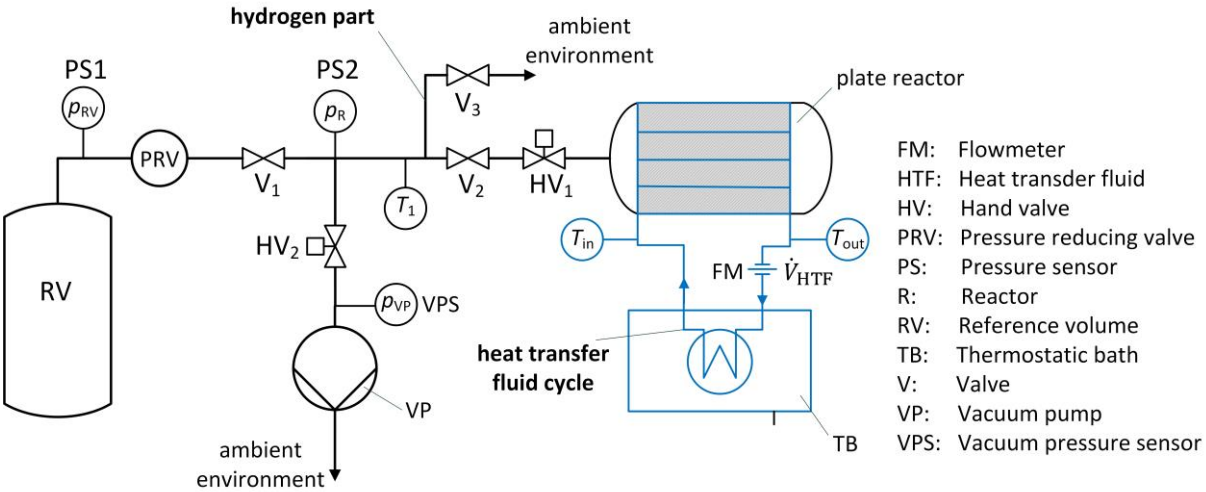

Figure C-2: Schematic flow diagram of the experimental setup for the single reactor characterization.

Results of the representative absorption experiment

In Figure C-3, the results of the representative absorption experiment for an absorption pressure of 30 bar are shown. In the HTF cycle, the inlet temperature was adjusted to $T_{\mathrm{in}} = 20\ °\mathrm{C}$ and the flow rate was $\dot{V}_{\mathrm{HTF}} = 4.5\ \mathrm{l\ min^{-1}}$. The temporal course of the specific HTF power and the HTF temperatures are illustrated in the upper diagram, while the profile of the transformed fraction is presented in the lower graph.

At $t = 0$, the reaction is initiated and due to the exothermic reaction, the HTF outlet temperature T_{out} increases. Furthermore, the transformed fraction of hydrogen (6 g of total absorbed hydrogen) also increases and shows a behaviour that corresponds to a first-order system response. Then, after approximately 100 s, all measured values area again in steady-state conditions. The oscillation in the inlet temperature by $\pm 2\ \mathrm{K}$ around the set value results from the regulation of the HTF cycle. Additionally, the slight overshoot in the transformed fraction is due to the temperature change of the gas in the reference volume. The initial

temperature is reached again after around 120 s. Using the values for the transformed fraction, for this experiment, a time constant of $\tau = 8$ s and a HC time of $\tau_{\mathrm{HC}} = 40$ s for a complete transformed fraction can be determined.

Next to the cycle time, it is also important to determine the experimentally transferred thermal power using this reactor. The observed maximum temperature difference in the HTF of -15 K, results in a specific peak heat power of $\dot{q}_{\mathrm{HTF}} = -4.9\ \mathrm{kW\ kg_{MH}}^{-1}$. Furthermore, assuming a nominal HC time of 60 s, the average specific power is calculated as $\bar{\dot{q}}_{60\mathrm{s}} = 2.42\ \mathrm{kW\ kg_{MH}}^{-1}$ (no thermal losses are included). When the curves for the transformed fraction and specific power are compared, it is obvious that heat is still transferred to the HTF although the reaction is completed after about 40 s. The reason for this observation is the sensible heating of the reactor and the MH caused by the reaction. This heat is transferred to the HTF until steady-state conditions are reached after approximately 100 s and the reactor as well as all hydride material is again at reference temperature.

From this proof of concept, it can be concluded that the plate reactor concept shows very good heat transfer characteristics as the reactor is able to transfer the heat from the material to the HTF in a time of $t \sim 60$ s. Therefore, this concept is suitable for the present open MHCS. By up-scaling the small-scale reactor, the mass ratio of passive reactor mass to active MH mass declines further.

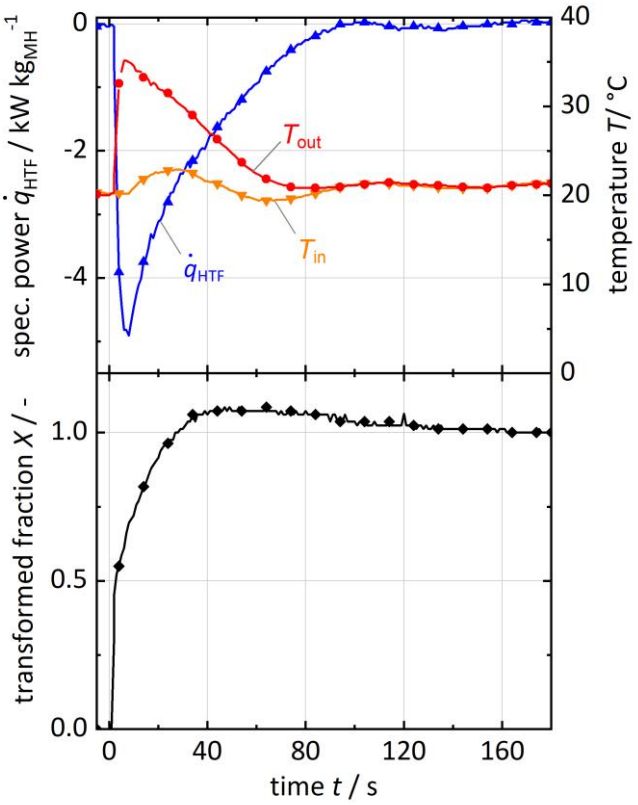

Figure C-3: Results of the reference absorption experiments for $p_{\mathrm{abs}} = 30$ bar and an HTF inlet temperature of $T_{\mathrm{in}} = 20$ °C.

D. Details for the thermodynamic characterization

D.1 Calculation of the hydrogen mass

For the PCI measurements of Hydralloy® C2 in Chapter 2.1, the hydrogen capacity ω at isothermal conditions as a function of the equilibrium pressure p_{eq} results from the ratio of absorbed/desorbed hydrogen mass to the MH mass (see equation (1-2)). In order to determine the hydrogen mass $m_{\mathrm{H2}}(t)$, the Sieverts principle is applied [151], according to which $m_{\mathrm{H2}}(t)$ can be determined by means of a pressure change in a reference volume measured by a very accurate differential pressure sensor. In the following, the procedure for this calculation is presented. The schematic flow diagram of the experimental setup that was used for the thermodynamic characterization is shown in Figure 2-1.

Hydrogen mass of absorption

During the absorption, the pressure in the reference volume decreases as a constant hydrogen mass flow rate is supplied to the MH sample. Since this pressure change is measured by means of the differential pressure sensor DSD, the reference volume RV+ is closed during the absorption. The absorbed hydrogen mass $m_{\mathrm{abs}}(t)$ follows from the difference of the hydrogen mass, which has left the Sieverts area $m_{\mathrm{SA,abs}}(t)$ reduced by the change of hydrogen mass $\Delta m_{\mathrm{free,des}}(t)$ in the free volume of the reactor section:

$$m_{\mathrm{abs}}(t) = m_{\mathrm{SA,abs}}(t) - \Delta m_{\mathrm{free,abs}}(t) \tag{D-1}$$

Based on the ideal gas law, $m_{\mathrm{SA,abs}}(t)$ is derived from the pressure drop in the Sieverts area as follows:

$$m_{\mathrm{SA,abs}}(t) = \frac{M_{\mathrm{H2}}\, p_{\mathrm{DSD,cor}}(t)}{R}\left(\frac{V_{\mathrm{tb,abs}}}{T_{\mathrm{SA}}(t)} + \frac{V_{\mathrm{SV,abs}}}{T_{\mathrm{R-}}(t)}\right) \tag{D-2}$$

For this calculation, the Sieverts area (SA) is separated in two different volumes: The tube volume $V_{\mathrm{tb,abs}} = V_{\mathrm{tb1}} + V_{\mathrm{tb2}}$ and the Sieverts volume $V_{\mathrm{SV,abs}} = V_{\mathrm{RV-}} + V_{\mathrm{SV1}} + V_{\mathrm{SV2}} + V_{\mathrm{SV3}}$, which is placed in the water reservoir and selected depending on the mass of the MH sample. During the measurements, all thermocouples in the water reservoir showed the same temperature. Therefore, hydrogen inside each Sieverts volume is at $T_{\mathrm{SA}}(t)$, while hydrogen in tube volume is at the temperature $T_{\mathrm{SA}}(t)$. In equation (D-2), M_{H2} is the molar mass of hydrogen, R is the universal gas constant and $p_{\mathrm{DSD,cor}}(t)$ is the corrected pressure difference. This correction was required, since during the automatic operation valve V_8 was opened before V_9.

Therefore, there was an initial increase of the Sieverts area volume, which has to be taken into account by using the minimal value at the beginning of the absorption according to:

$$p_{\mathrm{DSD,cor}}(t) = p_{\mathrm{DSD}}(t) - p_{\mathrm{DSD}}(t=0) \tag{D-3}$$

In equation (D-1), the change of hydrogen mass $\Delta m_{\mathrm{free,abs}}(t)$ in the free volume of the reactor section (RS) is derived from the pressure difference between the initial reactor pressure and the current reactor pressure as given by:

$$\Delta m_{\mathrm{free,abs}}(t) = \frac{M_{\mathrm{H2}}}{R}\left[p_{\mathrm{PS2/3}}(t) - p_{\mathrm{PS2/3}}(t=0)\right]\left(\frac{V_{\mathrm{free,R}}}{T_{\mathrm{R}}(t)} + \frac{V_{\mathrm{tb,RS,abs}}}{T_{\mathrm{MFC}}(t)}\right) \tag{D-4}$$

Thereby, the reactor section is separated in the free volume of the reactor $V_{\mathrm{free,R}}$ with the temperature $T_{\mathrm{R}}(t)$ and the tube volume $V_{\mathrm{tb,RS,abs}} = V_{\mathrm{tb3}} + V_{\mathrm{tb4}} + V_{\mathrm{tb5}}$ with the temperature $T_{\mathrm{MFC}}(t)$. Depending on the pressure value, $p_{\mathrm{PS2/3}}(t)$ is detected by the pressure sensors PS2 and PS3, respectively.

Combining the equations (D-1)–(D-4), the absorbed hydrogen mass was calculated and the hydrogen capacity at isothermal conditions as a function of p_{eq} was derived. Using ideal gas behaviour for this calculation is reasonable, as the influence of the compressibility at the comparable low pressures during the measurements is small (in Ref. [42] ideal gas versus real gas behaviour for the thermodynamic characterization is compared). Table D-1 summarizes all volumes, which are required for this calculation. The corresponding values are calculated from the pressure change in the experimental setup using a well-known volume.

Table D-1: Free volumes of the experimental setup.

Tube volumes [ml]					
V_{tb1}	V_{tb2}	V_{tb3}	V_{tb4}	V_{tb5}	$V_{\mathrm{free,R}}$
28.07	6.3	4.73	6.44	7.94	32.5
Sieverts and Reference volumes [ml]					
SV1	SV2	SV3	RV+	RV-	
292.3	492.8	1006.2	292.9	307.5	

Hydrogen mass of desorption

The remaining mass of hydrogen in the MH sample $m_{\mathrm{des,re}}(t)$ during the desorption is given by the initial hydrogen mass at the end of the absorption $m_{\mathrm{abs,end}}$ reduced by the desorbed hydrogen from the MH sample $m_{\mathrm{des}}(t)$ according to.

$$m_{\mathrm{des,re}}(t) = m_{\mathrm{abs,end}} - m_{\mathrm{des}}(t) \tag{D-5}$$

In this equation, the value of $m_{\mathrm{des}}(t)$ is obtained from the difference of the hydrogen mass $m_{\mathrm{SA,des}}(t)$ released to the Sieverts area and the change of hydrogen mass $\Delta m_{\mathrm{free,des}}(t)$ in the free volume of the reactor section:

$$m_{\mathrm{des}}(t) = m_{\mathrm{SA,des}}(t) - \Delta m_{\mathrm{free,des}}(t) \tag{D-6}$$

Since the flow direction of the MFM is only one way, the flow direction of the desorption differs from the absorption. Therefore, the experimental setup has different tube and Sieverts volumes (reference volume RV- is closed during the desorption) depending on the type of measurement. With the tube volume $V_{\mathrm{tb,des}} = V_{\mathrm{tb1}} + V_{\mathrm{tb4}} + V_{\mathrm{tb5}}$ and the Sieverts volume $V_{\mathrm{SV,des}} = V_{\mathrm{RV+}} + V_{\mathrm{SV1}} + V_{\mathrm{SV2}} + V_{\mathrm{SV3}}$ for the desorption, the value of $m_{\mathrm{SA,des}}(t)$ results from:

$$m_{\mathrm{SA,des}}(t) = \frac{M_{\mathrm{H2}}\, p_{\mathrm{DSD,cor}}(t)}{R}\left(\frac{V_{\mathrm{tb,des}}}{T_{\mathrm{SA}}(t)} + \frac{V_{\mathrm{SV,des}}}{T_{\mathrm{R+}}(t)}\right) \tag{D-7}$$

As the volume between the hydrogen valves V_9 and V_{13} was not evacuated at the beginning of the measurement, a correction of the differential pressure sensor DSD according to equation (D-3) was also required for the desorption.

In equation (D-6), the value of $\Delta m_{\mathrm{free,des}}(t)$ is derived from the difference between initial hydrogen mass at the beginning of the desorption $m_{\mathrm{free,des}}(t = 0)$, which is equal to the final value of the absorption and the remaining hydrogen mass in the free volume $m_{\mathrm{free,des}}(t)$ according to:

$$\Delta m_{\mathrm{free}}(t) = m_{\mathrm{free,des}}(t = 0) - m_{\mathrm{free,des}}(t) \tag{D-8}$$

With the volume $V_{\mathrm{tb,RS,des}} = V_{\mathrm{TV2}} + V_{\mathrm{TV3}}$ for the desorption, $m_{\mathrm{free,des}}(t)$ is given by:

$$m_{\mathrm{free,des}}(t) = \frac{M_{\mathrm{H2}}\, p_{\mathrm{PS2/3}}(t)}{R}\left(\frac{V_{\mathrm{free,R}}}{T_{\mathrm{R}}(t)} + \frac{V_{\mathrm{tb,RS,des}}}{T_{\mathrm{MFC}}(t)}\right) \tag{D-9}$$

Thus, the remaining mass of hydrogen in the MH sample during the desorption follows by combining the equations (D-5)–(D-9). It has to be noted that the calculated hydrogen mass of the desorption showed lower values compared to the absorption. However, as the same final hydrogen capacity was obtained during the following absorption, the MH sample had to desorb the same amount of hydrogen as was absorbed before. For this reason, the hydrogen capacity of the desorption was normalized by using a correction factor of 1.03. Further details of this measurement procedure including the measurement accuracy can be found in [97,122].

D.2 Measurement sensors for the thermodynamic characterization

Table D-2 summarizes the measurement sensors for the thermodynamic characterization of Hydralloy® C2, which are implemented in the experimental setup shown in Chapter 2.1.1.

Table D-2: Measurement sensors for the thermodynamic characterization.

Sensor	Type	Measurement range	Accuracy	Max. deviation
Mass flow controller MFC	Bronkhorst F-221M-PBD-33-V	0.5–25 smL min^{-1}	±0.5% Rd plus ±0.1% FS	0.15 smL min^{-1}
Pressure sensors PS1/PS3	Keller PA-21Y	1–120 bar	±1.5% FS	1.8 bar
Pressure sensors PS2	Keller PA-21Y	0–40 bar	±0.25% FS	0.1 bar
Pressure sensor DSD	Keller PD-33X	0–10 bar	±0.1% FS	0.015 bar
Thermocouple *T*	type K	-40 °C to +1100 °C	±1.5 K	±1.5 K

E. Experimental equipment for the demonstration of the open MHCS

In Table E- 1, the equipment of the experimental setup for the demonstration of the open MHCS is summarized (see Chapter 2.3). Thereby, this equipment is separated according to the the system´s hydrogen section and HTF infrastructure section.

Table E- 1: Equipment of the experimental setup.

Description	Type
Hydrogen section	
Electromagnetic three-way valves $V_{H2,1-2}$	Bürkert 0355-C
Electromagnetic valves $V_{H2,3-5}$	Bürkert 0255
Hand valves HV1 and HV2	Swagelok SS-42GS6MM
Hydrogen piping	Swagelok SS-T6M and SS-T10M
Mass flow meter MFM1	Micro Motion Elite CMF010M
Mass flow meter MFM2	Bronkhorst EL-Flow Select F-202AC
Overpressure valves OPV1-2	SV 805A
Pressure reducing valve PRV1	Messer Spectron EM61
Pressure reducing valve PRV2	Swagelok KPR1GRF417A2000
Pressure sensors PS1-2	Afriso DMU 05 P
Pressure sensor PS3	Keller PAA-33EI
Fuel cell	
Ammeter AM	LEM IT 600
Differential pressure sensors	Rosemount 3051/3001
DC electronic load	Höcherl & Hackl DS8412SC400
Fluid-to-air heat exchanger	BEHR CL048001
Liquid-to-liquid heat exchanger	VAU VM15/20
PEM FC	Hydrogenics Corporation HyPM™ HD8
Resistance thermometers	PT100 class A
Voltmeter VM	VariTrans P 27000
HTF infrastructure section	
6/2-way HTF valves	Landefeld PN250
HTF pump P_{amb}	Regloplas 90S, TP20
HTF pump P_c	VTM50-10-X
Impeller HTF flow meter MFM_{amb-c}	Meister DHGA-10
Resistance thermometers	Pt 100 class A
Thermostatic bath TB_{amb}	Reglopas 90S
Thermostatic bath TB_c	Lauda Proline RP845

F. Reactor cooling power

Under the reference conditions of the functional demonstration, Figure F-1 shows the temporal course of the reactor cooling power $\dot{Q}_{\mathrm{HTF,R1}}$ and a comparison to the cooling power in the cooling HTF loop $\dot{Q}_{\mathrm{HTF}}$ according to Figure 3-4. The temporal course of $\dot{Q}_{\mathrm{HTF,R1}}$ is determined by means of the temperature difference at the inlet and outlet of reactor R1 (see top of Figure 3-3) and the corresponding HTF flow rate. According to the states of operation, in the 1st HC, the cooling effect in the cooling HTF cycle is generated via reactor R1. Therefore, identical values of $\dot{Q}_{\mathrm{HTF,R1}}$ and $\dot{Q}_{\mathrm{HTF}}$ can be observed in the CP (point 2). The deviation in the HIP (point 1) results from the applied operation optimization and the time-shifted switching of the HTF outlet valves relative to the inlet valves. At the beginning of the 2nd HC, a positive peak of $\dot{Q}_{\mathrm{HTF,R1}}$ (point 3) can be observed as initially the total reactor mass is on cooling temperature level while ambient HTF enters at the inlet. This peak leads to additional thermal losses in the ambient HTF cycle during the regeneration of reactor R1. At $t = 156\,\mathrm{s}$, the absorption of hydrogen is initiated and the heat of formation of the exothermic reaction is transferred to the HTF (Point 4), which has to be released to the ambient environment or can be used for heating purposes (peak value of -3.8 kW). At the same time, the cooling effect of $\dot{Q}_{\mathrm{HTF}}$ in the 2nd HC is generated by reactor R2 and subsequently the characteristic recurrent profiles can be seen.

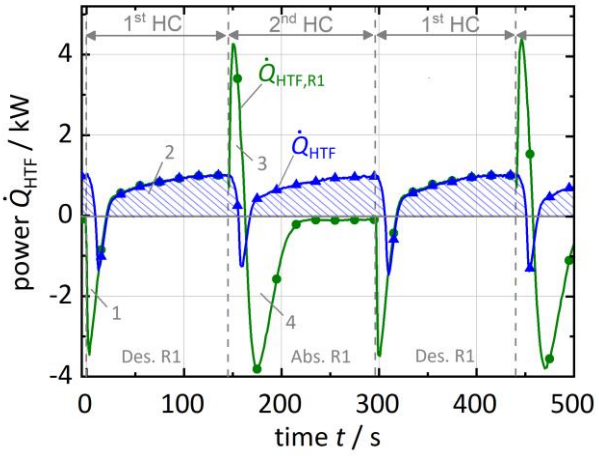

Figure F-1: Temporal course of the reactor cooling power $\dot{Q}_{\mathrm{HTF,R1}}$ and comparison to the cooling power in the cooling HTF loop $\dot{Q}_{\mathrm{HTF}}$ (under reference conditions of the functional demonstration)

.

G. Heat transfer coefficient for corrugated plates

The heat transfer coefficient α_{HTF} for corrugated plates of the present plate reactor in Chapter 5 (see equations (5-10) and (5-12)) can be calculated according to the correlation of Martin [144], which depends on the amplitude of the corrugation and the surface enlargement factor. The corrugation amplitude a is derived from the reactor height h_{R}, the total number of separating plates $N_{\mathrm{SP}} = 2N_{\mathrm{MH}}$ and the thickness d_{SP}:

$$a = \frac{1}{2}\left(\frac{h_{\mathrm{R}}}{2N_{\mathrm{MH}}+1} - d_{\mathrm{SP}}\right) \tag{G- 1}$$

The surface waviness of the plates (wavelength λ_{a}) is taken into account by the surface enlargement factor φ. For a sinusoidal corrugation, φ is approximated by

$$\varphi \approx \frac{1}{6}\left[1+\left(1+\left(\frac{2\pi a}{\lambda_{\mathrm{a}}}\right)^2\right)^{0.5} + 4\left(1+\frac{\left(\frac{2\pi a}{\lambda_{\mathrm{a}}}\right)^2}{2}\right)^{0.5}\right] \tag{G- 2}$$

From the corrugation amplitude and the surface enlargement factor, the hydraulic diameter d_{hd} is as follows:

$$d_{\mathrm{hd}} = \frac{4a}{\varphi} \tag{G- 3}$$

The Prandtl number Pr and the Reynolds Re number are given by

$$Pr = \frac{\gamma_{\mathrm{HTF}}\,\rho_{\mathrm{HTF}} c_{\mathrm{p,HTF}}}{\lambda_{\mathrm{HTF}}} \tag{G- 4}$$

and

$$Re = \frac{v_{\mathrm{HTF}}\,d_{\mathrm{hd}}}{\gamma_{\mathrm{HTF}}} \tag{G- 5}$$

where γ_{HTF} is the dynamic viscosity of the HTF and the HTF flow velocity v_{HTF} is calculated according to:

$$v_{\mathrm{HTF}} = \frac{\dot{V}_{\mathrm{HTF,R}}}{2ab\,(N_{MH}-1)} \tag{G- 6}$$

The Nusselt number Nu in equation (5-14) for the plate heat exchanger with a chevron pattern is finally given by:

$$Nu = 0.205 Pr^{\frac{1}{3}} (f_g Re^2 \sin(2\beta))^{0.374} \frac{\gamma_{\mathrm{HTF}}}{\gamma_{\mathrm{SP}}} \tag{G- 7}$$

Here, β is the inclination angle of the corrugation (chevron angle) and γ_{SP} is the dynamic viscosity of the HTF at the wall temperature. For $Re < 2000$, which is true in all conducted calculations, the fanning friction factor f_g is defined by:

$$f_g = \left[\frac{\cos(\beta)}{\left(0.045\tan(\beta) + 0.09\sin(\beta) + \frac{16}{Re}\cos(\beta)^{-1}\right)^{0.5}} + \frac{1-\cos(\beta)}{\left(\frac{37.05}{Re^{0.289}}\right)^{0.5}} \right]^{-0.5} \quad \text{(G- 8)}$$